Intraoperative Multimodal Imaging System for Surgical Guidance

Kosta Popović
Belgrade, Republic of Serbia

Bachelor of Arts, Hamilton College, 2006
Master of Arts, University of Virginia, 2009

A Dissertation presented to the Graduate Faculty
of the University of Virginia in Candidacy for the Degree of
Doctor of Philosophy

Department of Physics

University of Virginia
May 2013

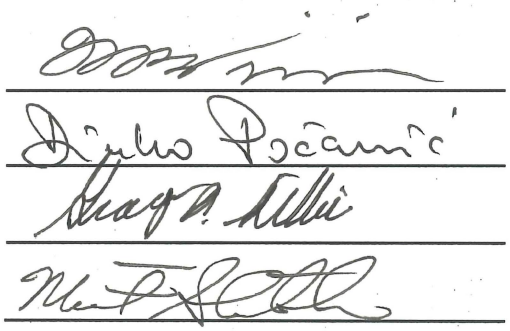

ABSTRACT

This dissertation describes the development of an Integrated Multimodal Imaging System (IMIS) for intraoperative guided surgery. The IMIS consists of an unique small field of view (FOV) gamma camera based on the silicon photomultiplier (SiPM) technology and a video camera for simultaneous visible and near infrared fluorescence (NIRF) imaging. The targeted tracers that are labeled with a radioisotope and a near infrared (NIR) fluorophore are initially injected into the patient and accumulate in the tumors or lymph nodes (surgical targets). The gamma imaging is used for initial target localization through thick overlying tissue and the optical imaging is used to help surgeons differentiate the targets from surrounding tissue once the targets are near the surface. The IMIS components are integrated on a mobile cart that allows the system to be transported to the operating room (OR). Our hope is that intraoperative imaging with IMIS can help surgeons in the OR in a wide scope of procedures, including determining the location and extent of primary carcinomas, detecting secondary lesions and identifying lymph nodes during sentinel lymph node biopsy (SLNB).

The feasibility of the concept was demonstrated by successfully imaging surgical patients in a clinical study during SLNB using the gamma imaging component of IMIS, imaging tumor bearing mice pre-clinically and characterizing the performance of IMIS in multimodal imaging in bench-top and simulated surgery experiments in the laboratory.

TABLE OF CONTENTS

LIST OF FIGURES

LIST OF TABLES

LIST OF ABBREVIATIONS AND SYMBOLS

ADC – Analog to digital converter

APD – Avalanche photodiode

CCD – Charge coupled device

CCT – Correlated color temperature

COG – Center of gravity

CRI – Color rendering index

CTF – Contrast transfer function

DAQ – Data acquisition system

ESR – Extrinsic spatial resolution

FOV – Field of view

fps – Frames per second

FWHM - Full Width at Half Maximum

GUI – Graphical user interface

HSA – Human serum albumin

ICG – Indocyanine green

ISR – Intrinsic spatial resolution

IEC - International Electrotechnical Commission

$LaBr_3$ – Lanthanum (III) Bromide

LED – Light emitting diode

MGC – Mobile gamma camera

MPPC – Multi-pixel photon counter

MTF – Modulation transfer function

NIR – Near infrared

NIRF – Near infrared fluorescence

OR – Operating room

PCB – Printed circuit board

PDE – Photon detection efficiency

PMT – Photomultiplier tube

SBR – Signal-to-background ratio

SNR – Signal-to-noise ratio

SiPM – Silicon photomultiplier

SLN – Sentinel lymph node

SLNB – Sentinel lymph node biopsy

^{99m} Tc – Technetium-99m, a metastable nuclear isomer of Technetium-99, used as a medical radioisotope

^{99m} Tc-SC – ^{99m}Tc sulfur colloid

WD – Working distance

CHAPTER 1: INTRODUCTION

At present, there exists a great need for improved means of intraoperative imaging in multiple clinical settings in oncology. Better intraoperative imaging options in theory correlate well with better information a surgeon has available intraoperatively, which leads to better surgical decision making, improved patient outcomes and lower morbidity rates. For example, the cancer recurrence rates for non-palpable breast lesions are reported to be between 20 % and 50 % (1; 2; 3) and similarly between 15 % and 30 % for colorectal cancer (4; 5). The false negative rates in melanoma have been reported as high as 24 % (6; 7). Minimizing the cancer recurrence rates would result in decreased cost and lower morbidity and trauma to the patient, which is the motivation behind this project.

1.1 Current practice of SLNB and carcinoma excision

A standard method of staging certain types of cancer is the sentinel lymph node biopsy (SLNB) (8; 9; 10). This concept relies on the fact that in the spread of many types of cancer, the metastasis will pass down the lymph system, and some cancer cells with be deposited in the first (sentinel) lymph node. The ability to biopsy this node and assess the presence or absence of cancer metastasis in the node is one of the most important prognostics tests today and can help guide decisions about patient treatment. The majority of the SLNB procedures today utilize injecting the patient with blue dye and

^{99m}Tc sulfur colloid (^{99m}Tc-SC), and employing preoperative imaging and intraoperative nuclear counting with a hand-held probe as a standard of care. However, multiple publications have recently reported that the success rates in identifying SLNs with the nuclear medicine methods are as good as with the visual blue dye detection method, even favoring the nuclear medicine methods alone (11; 12). Furthermore, in some cases staining from the blue indigo dye can cause unnecessary aesthetic issues in post-surgical tattooing of the skin of the patient; this can cause inconvenience particularly when the lymph nodes are near the patient's face (13). The nuclear medicine methods alone will be discussed in more detail in this section.

The SLNB procedure most commonly involves preoperative planar lymphoscintigraphy and intraoperative gamma probe detection. Preoperative planar lymphoscintigraphy is sometimes used concurrently with single photon emission computed tomography (SPECT) and x-ray computed tomography (CT) that require the patient to be imaged with a fixed gamma camera (FGC) or a dedicated SPECT-CT imaging system. The three dimensional imaging of SLNs by SPECT-CT can significantly improve the correlation between the locations of high radioactivity concentration and the anatomical map of the patient and show more accurate information about the exact location of the nodes and lymphatic drainage patterns (14; 15; 16) compared to two dimensional lymphoscintigraphy alone. The reason that the SPECT-CT method is not used regularly is because of the greater radiation dose from the x-ray CT to the patient compared to lymphoscintigraphy alone as well as a considerable increase in equipment cost, while the method still fails to address the need for intraoperative imaging of the patient. On occasion, postoperative ex-vivo planar gamma imaging of excised nodes is

used, but as most OR suites do not have the gamma cameras available on-site, most frequently the nodes are sent straight to pathology for staining and microscopic inspection.

The intraoperative gamma probe method has been gaining popularity in the last two decades as an intraoperative complement to the visual blue dye inspection method, and coupled with planar preoperative lymphoscintigraphy has become a standard of care in cancer staging. In this procedure, the preoperative imaging is performed first by using the FGC, which gives information about the lymphatic drainage patterns of the injected ^{99m}Tc-SC, and aids surgeon in developing a plan of surgery before the incision is made. In more detail, the patient is injected with a standard dose of ^{99m}Tc-SC in the nuclear medicine imaging suite the day of, or the day before the surgery. The patient is then imaged with a conventional fixed gamma camera and the pathways of lymphatic flow and lymph nodes are recorded on the images and marked on the patient. In the operating room (OR), the surgeon uses a hand-held gamma probe, which is a radiation-detecting device that uses auditory signals and meter read-outs of counts detected to provide the feedback to the location of ^{99m}Tc-SC within the patient. The surgeon then removes all lymph nodes whose gamma probe count rate in-vivo exceeds one tenth of the count rate of the hottest lymph node ex-vivo (17; 18). However, practical and technical drawbacks exist with this method. Some of the drawbacks are related to the equipment – for example the non-imaging characteristics of the gamma probe (presents only auditory signal and count rate information) or imperfect hardware intrinsic properties of the probe like the wide activity acceptance angle. The wide acceptance angle and the wide radial sensitivity distribution without the ability to precisely single out the source within the patient can

even further confound a complicated distribution process of radioactivity in the lymphatic system, whereas the spatial position and the uptake level vary depending on cancer type and location. For example, the injection spot and the SLNs can be very close in breast and head and neck tumors, while they are usually far apart in melanoma; on the other hand, the uptake of radio-nuclide in the SLNs is usually higher in melanoma, lower in breast cancer and can vary strongly in prostate cancer, typically varying between 0.01 % and 1 % (median 0.1 %) of the injected dose (19). Other drawbacks of this method are related to logistics – for example the inability of the surgeon to acquire additional lymphoscintigraphy images once the patient is in the OR, in case the gamma probe or FGC findings are inconclusive or the intraoperative findings call into question the preoperative findings. Postoperative imaging is not routinely performed in the OR as discussed in the paragraph above due to lack of imaging equipment on-site. Finally, there are significant non-technical concerns with this method, like the additional patient scheduling issues connected to imaging with the FGC, which can add significant wait time between the FGC imaging and actual surgery. The scheduling issues can even extend to patients needing separate injections for cases scheduled for morning SLNB with the FGC imaging performed the day before the surgery in that case.

With this in mind, it is clear that the intraoperative imaging during the present standard of care surgical procedure can be improved upon; possible ways of addressing some of these issues will be discussed in the next paragraph in more detail.

1.2 Considerations of different imaging modalities as related to SLNB and carcinoma excision

To address how the guidance procedure and other issues can be improved for the SLNB practice described in the previous paragraphs, important properties of imaging modalities relevant to this imaging task need to be considered first. The overall performance and task-specific effectiveness of all imaging modalities in general are determined by the fact that there is typically an inverse relationship between spatial resolution and sensitivity, as well as among a multitude of other parameters that affect the use of a modality; parameters like the imaging time, field of view imaged or ease of handling and logistics can vary significantly depending on the imaging task and the modality. It is important to evaluate which procedure task-specific parameters are important in various imaging modalities to be able to judge which ones are useful for each surgical procedure. For example, an ideal intraoperative surgical guidance system would help guide the surgeon to the location of the tumor or SLN (i.e. the location of the target or targets) and then provide information about the extent of the tissue that needs to be removed. In the case of tumor mapping, the image guidance system ideally would detect the borders of the tumor with high resolution and with high sensitivity for the signal emitted by the tracer. The surgeon can use this information to excise the tumor fully, as tumor cells remaining in the patient could lead to cancer recurrence. Note that this means that the system needs to have high sensitivity and spatial resolution both through several centimeters of tissue (prior to the incision) and when the target is near the surface. Furthermore, two additional task-specific requirements are that this system

should be compact so it can be maneuvered within the OR easily by the surgical staff, and that the system can be operated close to real-time as not to prolong the surgery significantly compared to the present standard of care procedure.

Unfortunately, no single imaging modality possesses all of these characteristics. For example, the x-ray based imaging modalities provide excellent resolution images with high penetration power; however the radiation dose concerns, high tracer concentration necessary for tracer distribution visualization, and the size of the x-ray/CT equipment prevent this modality for being useful intraoperatively for the SLNB procedures. Ultrasound on the other hand is compact and utilizes hand-held transducers, but has low sensitivity and spatial resolution in detection of deep breast lesions and lymph nodes (20) and has a lack of tumor-specific targeting agents. MRI has very good spatial resolution and good tumor sensitivity but limited specificity (can lead to high number of false positives). Most importantly, MRI is expensive and hard to translate to the OR logistically, requiring dedicated operating suites and specialized instrumentation while obstructing surgeon's access to the patient during imaging. The nuclear medicine techniques (PET and SPECT) offer good sensitivity through substantial tissue thickness. They can additionally be translated to hand-held use with the recent advent in the field of photomultiplier tubes (PMTs) (21; 22; 23), but their spatial resolution is lower compared to the modalities mentioned above. Finally, optical imaging techniques using fluorescent agents can provide excellent spatial resolution and can be translated to the OR fairly easily. The advantage of optical imaging compared to nuclear medicine imaging for real-time surgical guidance is that the imaging can be done from distances (several decimeters away from the patient), allowing the surgeon ready access to the surgical site. However,

the sensitivity through thick tissue is poor and the tissue attenuation limits depth of penetration of photons to about 1 – 2 cm in the near-infrared range (700 - 900 nm). This fact prevents the NIR imaging alone from being adequate for localization of tumors and secondary lesions, and renders this modality impractical for the task of initial localization of surgical targets.

From the standpoint of targeted tracers for use in intraoperative imaging, recent advances and discoveries in the field of biochemistry and targeted imaging agents have allowed for unmitigated growth and interest in the molecular imaging. The majority of these agents are designed for nuclear medicine modalities (PET and SPECT) because of the high sensitivities of these modalities compared to other modalities discussed above, which can allow for detection of low concentrations of the agent. However, significant progress (24; 25; 26) has been reached in developing tracers for optical and NIRF imaging, even with concerns of low tissue penetration ability of this modality and the limited number of NIR fluorophores approved for clinical use in humans.

1.3 Discussion on improving the intraoperative guidance procedure during SLNB and carcinoma excision

Following the discussion in the previous sections, it is apparent that no single modality can satisfy all of the important requirements for the SLNB and tumor surgery. However, a combination of modalities could provide more complete information about the location and extent of the tumors and lymph nodes or other targets of interest within the patient. This concept has been evolving over the last decades and is still reaching its

peak, as a PubMed search for phrase “multimodal imaging” shows an exponential growth in the number of published publications over the last ten years. Consequently, modalities that could be combined from technical and practical standpoint to provide the surgeons with a more complete set of information about the location and extent of tumors and lymph nodes within the patient were considered for the system described in this dissertation.

A combination of planar gamma scintigraphy and near infrared fluorescence (NIRF) imaging can overcome the limitations of separate imaging modalities and satisfy the imaging requirements necessary for surgical procedures that utilize injected tracers. These two imaging modalities are complementary in that the gamma scintigraphy provides good spatial resolution and high sensitivity tracer imaging through thick biological tissue to assist the pre-incision tumor or lymph node localization, while the NIRF modality provides excellent spatial resolution for precise visualization of SLNs or tumor margins near the surface once the surgeon is near the target.

These two modalities have been extensively evaluated separately in recent years for intraoperative image-guided SLNB for various types of cancers. Prototype small FOV gamma cameras have been successfully tested for intraoperative gamma scintigraphy in breast cancer SLNB (Aarsvold/GammaCAM, Mathelin/CarollReS, Scopinaro/IP-824), melanoma SLNB (Stoffels/Sentinella, Dengel/13 x 13 cm camera), oral cancer SLNB (Tsuchimochi/SSGC) and prostate and testicular cancer SLNB (Vermeeren/ Sentinella) among others. On the other hand, the NIRF imaging has been tested for intraoperative guidance for breast cancer SLNB (Hirche/IC-View, Troyan/FLARE, Hutteman/van der Vorst/mini-FLARE, Sevick-Muraca/FDPM, Kitai/Tagaya/PDE, Olcott/NodeView,

Garbay/Minicam II, Goto/Motomura/2020tc, Kerrou/Pitre/POCI), melanoma SLNB (Tanaka/Namikawa/PDE, Olcott/NodeView), cervical SLNB (Crane/Munich prototype, Schaafsma/mini-FLARE) and head and neck SLNB (Bredell/PDE, van der Vorst/mini-FLARE) among others. These imaging systems and studies will be discussed in more detail later in this dissertation.

Gamma and NIRF imaging have been used together in a recent preclinical study in pigs (Fujii/Coded aperture with a SMART camera and FLARE), showing promising results for using these two modalities complementarily (27). However, the authors reported that the system used in their preclinical study exhibited poor logistics and handling characteristics that are crucial for a successful SLN mapping and implementation of any new imaging systems in surgical mainstream. The authors were only able to position the coded aperture system to image the patient in upward facing direction due to the size and bulk of the coded aperture mask, detector/shielding combination and rigid attachment to the FLARE imaging system. Combined with other confounding factors related to the performance of the gamma camera, this system in particular was not deemed potentially useful in the OR environment in its present condition.

The visible/NIRF and gamma modalities could be implemented in intraoperative use if the logistics can be synchronized not to impede the standard intraoperative surgical flow and the imaging systems provide clear access to the surgical field. The NIRF imaging task can be done in real-time, and the gamma imaging modes can be adapted to provide good images to the surgeon in less than 30 seconds. These properties allow a combined gamma/NIRF system to be used in a way that will not hinder surgical flow

physically or temporally. This dissertation describes the development of an Intraoperative Multimodal Imaging System (IMIS) to aid image guided surgery in a wide range of procedures including but not limited to the SLNB and tumor surgery. The IMIS consists of an unique small field of view (FOV) gamma camera based on the silicon photomultiplier (SiPM) technology and a video camera for simultaneous visible and near infrared fluorescence (NIRF) imaging. In the following chapters, the physics behind the imaging modalities of the IMIS and the technical components that comprise both subsystems will be described. The performance of the subsystems working separately and in unison through a series of bench-top experiments, preclinical and clinical studies will be presented.

CHAPTER 2: GAMMA MODALITY

The core of the gamma modality consists of a gamma camera that is able to detect gamma rays being emitted by radioactive tracers injected in the patient. In this section, the principles of gamma ray imaging, detection and interaction with matter as well as the equipment and parts used to construct the gamma subsystem are described.

2.1 Gamma ray imaging

Gamma rays are an example of electromagnetic radiation of high energy, which are most commonly produced by radioactive decay from high energy states of atomic nuclei, but also by other nuclear and sub-atomic particle interactions. The types of interaction of gamma rays with matter are Compton scattering, photoelectric ionization and pair production. The nature of interaction by which most gamma rays are detected is photoelectric ionization and this detection process, as well as the necessary equipment for the gamma camera described in this dissertation, will be discussed in subsequent sections. The discovery of radioactivity and radioisotopes in the late 19th century quickly led to their use in the field of medicine. However, it was not until the late 1930s and emergence of appropriate facilities that could produce artificial radioisotopes (cyclotrons and fission reactors) that the field of nuclear medicine fully emerged (28). These radioisotopes were used progressively in therapeutic and laboratory procedures, which fueled the

development of radiation monitoring equipment to track the distribution and amount of radioisotopes in-vivo or in-vitro. Initially, these devices were limited to output only a count-rate value, but with work of Cassen (29) and later Anger (30), they evolved to a point where they could output a two dimensional image, which significantly improved the surgeon's ability to judge the radioisotope distribution and concentration. The advent of PET and SPECT concepts in the 1950s and their widespread use from 1960s through 1980s was respectively followed with concepts like fusion of PET and SPECT with CT (1990s) and MRI (2000s). Coupled with the development of targeted tracers and molecular medicine, the nuclear medicine has become one of the major contributors to improving patient outcomes in oncology and beyond.

At present, mobile gamma cameras (MGCs) with small form factor offer surgeons the ability to assess the distribution within the surgical patient of injected radiotracers or radiopharmaceuticals, a task currently left to inspection of preoperative scintigraphic or SPECT images and the intraoperative use of non-imaging gamma probes. Small FOV MGCs have been used in various procedures as mentioned in the previous chapter to assist the standard non-imaging gamma probes by providing more precise information (and in a shorter time) on the distribution of radioactivity in the cancerous versus surrounding healthy tissue. The present standard of care non-imaging probes suffer from a number of limitations, including limited to no spatial resolution, operator dependence, difficulty in quantification of radioactivity because of the strong dependence of their sensitivity upon probe-to-source separation, and no ready means of providing documentation of activity spatial distribution.

2.1.1 Gamma ray detection

The first attempts at building a gamma camera came in 1952 (31) by Hal Anger; however, his blueprint of the camera in 1957 (32) is better known, and this basic design is still used today (Figure 1). In general, a gamma camera consists of one or more crystals (scintillators) coupled to an array of photomultiplier tubes that are connected to readout electronics and a computer; the camera can also make use of a collimator. The scintillators are materials that exhibit scintillation, a physical process in which the material emits photons as a result of an ionization event in the material.

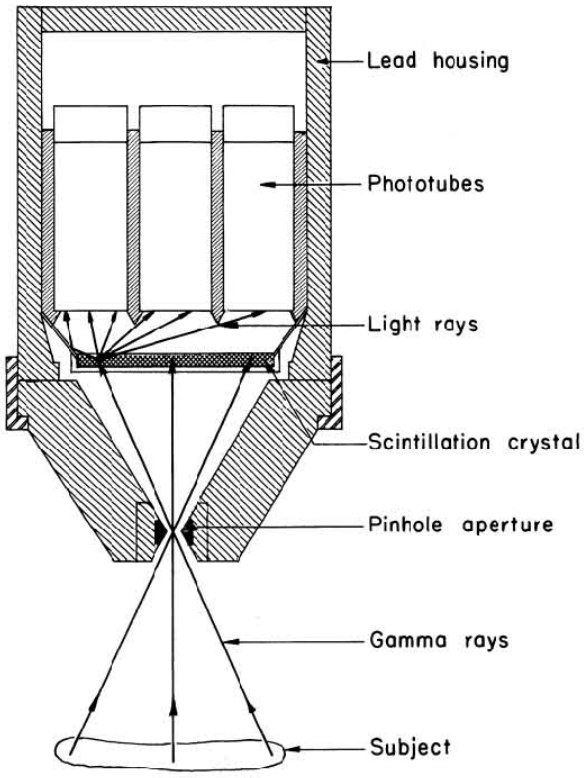

Figure 1: Sectional drawing of Anger's gamma camera (32)

The scintillator material can be organic or inorganic, and the most commonly used scintillators in imaging detector technology are certain types of inorganic crystals which can be seen in Table 1. During the photoelectric absorption process, the gamma ray gives all of its energy to an electron in the scintillator detector and knocks it out from the atom. Filling of the vacated hole by the electrons from the outer shell produces a characteristic photon that is collected by photodetectors such as photomultiplier tubes (PMTs). By optically coupling the scintillator crystal to arrays of PMTs, the photons incident on the photocathode of a PMT liberate photoelectrons through the photoelectric effect. These electrons are then accelerated by a strong electric field in the PMTs into dynodes, releasing additional electrons, and this process is repeated several times (Figure 2). After the charge amplification process (with the gain typically on the order of 10^6), the charge packet reaches the PMT anode, which is connected to the electronic readout equipment; the magnitude of the charge is ideally proportional to the incident energy of the gamma ray.

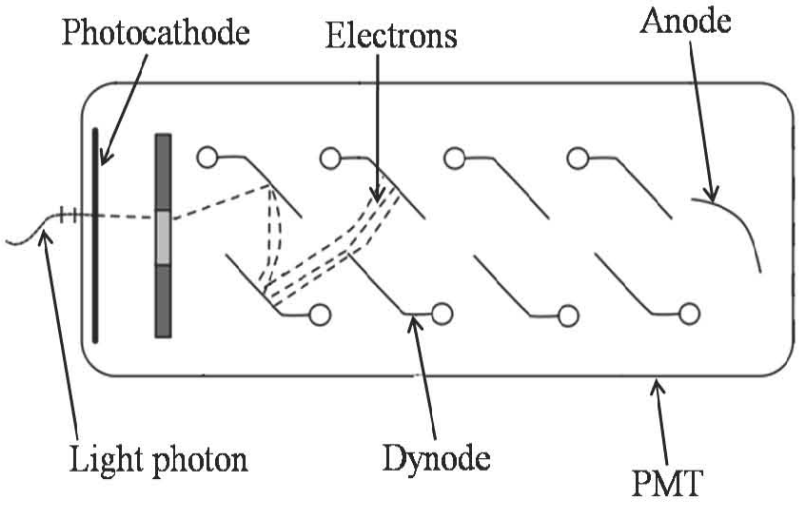

Figure 2: Photomultiplier tube schematic (33)

	Hygro-scopic	Peak wavelength emitted (nm)	Attenuation coefficient at 140 keV (cm^{-1})	Light yield (photons/keV)	Density (g/cm^3)	Decay time (ns)
NaI:Tl	Yes	415	3.12	38	3.67	230
CsI:Na	Yes	420	4.46	43	4.51	630
CsI:Tl	Slightly	540	4.53	56	4.51	1000
$LaBr_3$:Ce	Yes	380	3.42	63	5.1	16
BaF_2	Slightly	220	1.82	2	4.89	0.7
$Bi_4Ge_3O_{12}$ (BGO)	No	480	11.76	9	7.13	300
LYSO	No	425	11.28	27	7.1	41

Table 1: Properties of common scintillation materials (34; 35)

2.1.2 Properties of gamma scintillators

The properties of scintillators determine their usefulness for a particular task like the application in medical imaging. Some of the important characteristics relevant to this task are short decay time, high density, low cost, high light yield, transparency to its own emitted light and linearity. There are often small amounts of impurities (dopants) introduced in these crystals (a process called activation) to improve some of the above mentioned properties. In a pure inorganic scintillator, the process of emission of light photons after absorption of gamma rays is inefficient. By adding proper impurities, some of the newer inorganic scintillators can achieve very high light output and good energy resolution with solid physical properties compared to typically used thallium doped sodium iodide and cesium iodide (NaI:Tl and CsI:Tl); Lanthanum (III) bromide ($LaBr_3$:Ce) is an inorganic halide salt that was discovered by researchers in Delft and Bern Universities in Europe (36). With the developments in the manufacturing and crystal growth process, the $LaBr_3$ crystal is made today as robust as the conventional NaI crystals, and packaging the crystal properly minimizes the effects of its poor hygroscopity properties. For example $LaBr_3$ is ~ 1.4 times as dense as NaI:Tl, has ~ 1.6 times the light yield of NaI:Tl and has a 16 ns decay time (NaI:Tl has a 230 ns decay time). Based on these properties, a $LaBr_3$:Ce single crystal scintillator (BrilLanCe 380, Saint-Gobain Crystals, Hiram, OH) was selected for the gamma camera described in this dissertation.

2.1.3 Silicon Photomultipliers

Until recently, conventional PMT vacuum tubes were almost exclusively used in the construction of gamma cameras, to perform the charge amplification. The main drawback of using conventional PMTs in gamma cameras for intraoperative use is their size and the resulting weight of the camera housing, which limits the mobility, maneuverability and practical hand-held use of the camera. In recent years, Multi-Pixel Photon Counter (MPPC), also called a Silicon Photomultiplier (SiPM) has been introduced as a replacement for conventional PMTs. The MPPC is a type of a photon counting device that is made up of multiple avalanche photodiodes (APD) connected in parallel and operated in Geiger mode. Geiger mode is achieved by biasing the SiPM with a voltage higher than the breakdown voltage by a few volts (37). APDs are in themselves high-speed, high-sensitivity photodiodes. When light photons are incident upon an APD, electron-hole pairs can be generated if the light energy is larger than the band gap energy. In Geiger mode the APD then internally multiplies the number of valence electrons, thereby converting a low-level light signal into a large electrical signal. Each APD pixel of the MPPC generates a pulse signal when it detects a photon. To create an area photodetector, arrays of MPPCs are used. SiPMs have been shown to be comparable in total quantum efficiency (~ 20 %) and gain performance (10^6) to the conventional PMTs (38), in addition to having several advantages like the lower voltage bias operation, insensitivity to magnetic fields, and most importantly, ruggedness and a significant reduction in size. The insensitivity to magnetic fields is an added bonus for general use in the OR as it allows for wide array of surgical tools to be used near the camera, as well as

the option for integration of the camera with any magnetic resonance equipment. SiPMs exhibit thermal noise that increases with increasing ambient and device temperatures. The significant reduction in size is crucial as it improves logistics and allows the cameras to be used in a hand-held operation compared to an operation mode where the camera is connected to a gantry arm or a part of a larger, non-moveable imaging system. The Hamamatsu SiPMs were a chosen for the system described in this dissertation. This choice was made partly due to the fact that their photon detection efficiency (PDE) spectrum (Figure 3) is better matched to the emission spectrum of $LaBr_3$:Ce (Figure 4) compared to a different SiPM model (SensL Corp., Lexington, MA) that was tested during the design process (39).

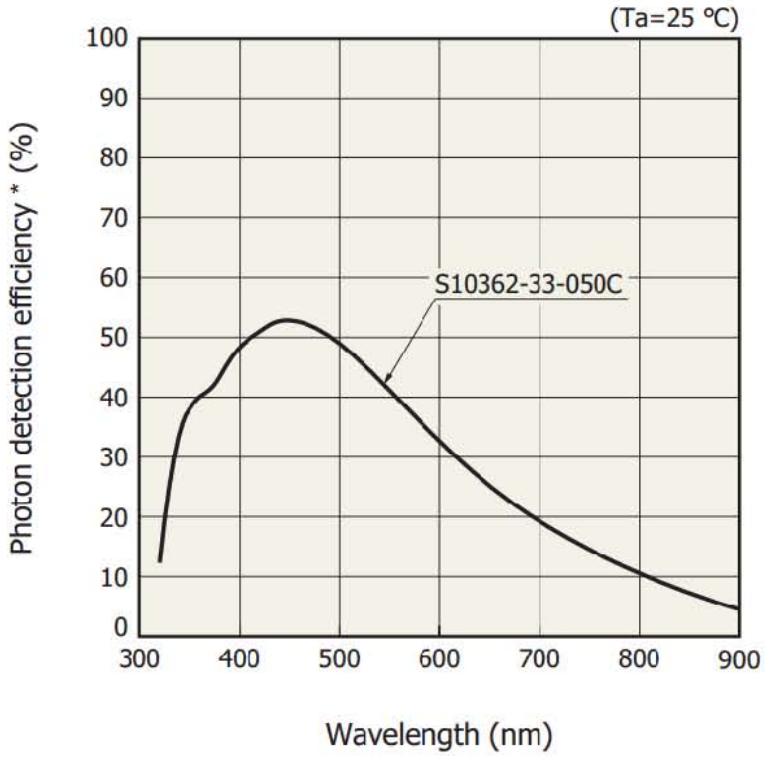

Figure 3: Photon detection efficiency of Hamamatsu S10362-33 MPPC (40)

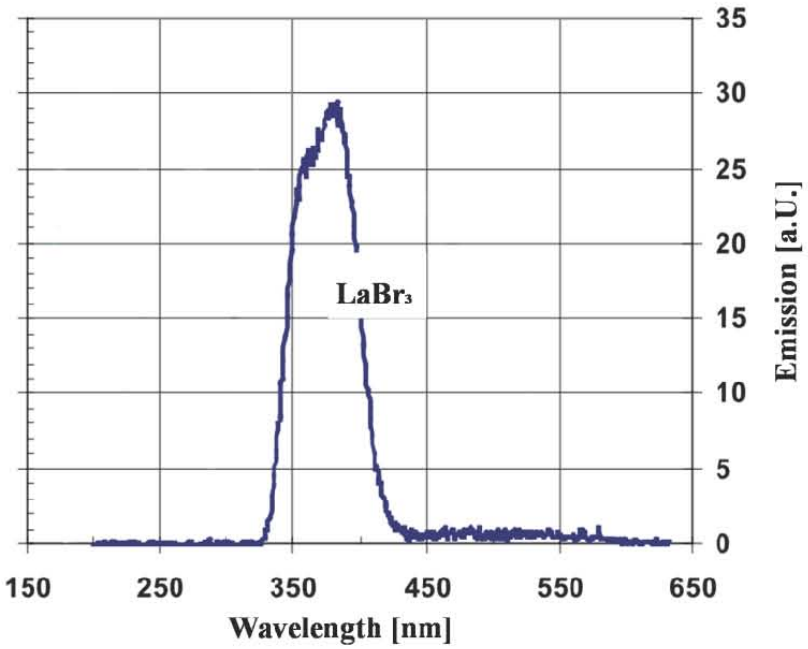

Figure 4: Scintillation emission spectrum of the BrilLanCe380 crystal (35)

2.1.4 Gamma ray collimation and image formation

Due to the fact that the gamma ray emission from a radioactive source is an isotropic process (non-preferential in terms of direction), a collimator is required in front of the gamma camera to aid image formation by helping define the incident direction of the gamma ray and avoid flooding of the gamma camera. A common image forming element for gamma camera imaging with a good balance of detection efficiency and spatial resolution is a parallel hole collimator. This collimator typically has an array of closely spaced holes of same shape (they can be square, round or hexagonal), and projects an image of the same size as the object onto the detector. The collimator is a necessary piece of the gamma imaging system and it is an important factor in determining the camera's performance due to the fact that by design it rejects the vast majority of the

incoming gamma rays. It must be carefully designed in order to maximize the gamma detection efficiency (the ratio between the photons that pass through the collimator compared to the number of photons incident on the collimator), while providing a spatial resolution that is adequate for the imaging task at hand.

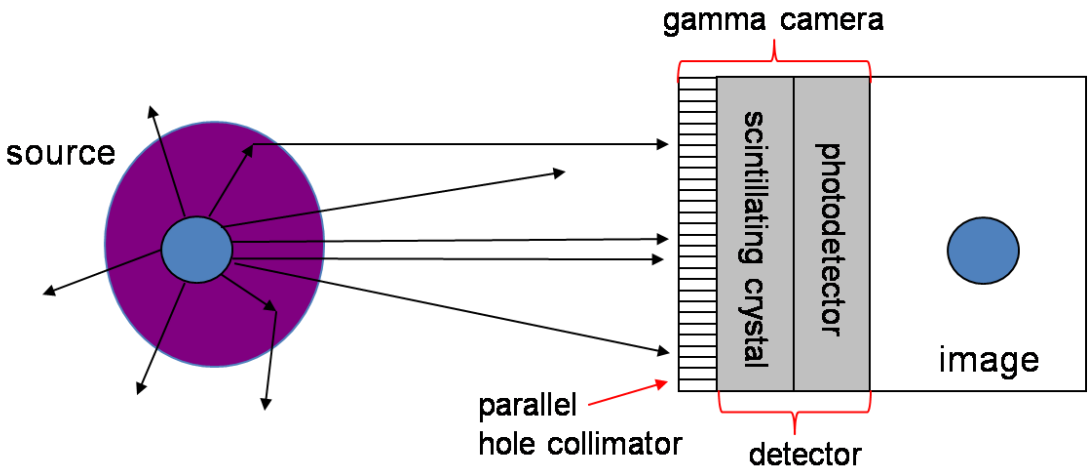

Figure 5: Parallel hole collimator principle

A primary consideration (30) in designing a parallel hole collimator is to make sure that the wall (septal) penetration of gamma rays from one collimator hole to another is sufficiently small. A standard rule of thumb is to keep septal penetration under five percent (30). The dimensions of the holes also play a vital role in the performance of the collimator. Collimator hole length l, diameter d and shape constant K all affect the resolution and efficiency of the collimator according to the equations below (30):

$$R = \frac{d(l_e + b + c)}{l_e} \qquad \text{equation 1}$$

$$g = \left[\frac{Kd^2}{l_e(d+t)}\right]^2 \qquad \text{equation 2}$$

where b is the distance between the source and the collimator, c is the distance between the collimator and the scintillator and t is the wall (septal) thickness. The quantity $l_e = l - 2\mu^{-1}$ is the effective length of the collimator, where μ is the total linear absorption coefficient of the material and its inverse is the mean free path of the gamma ray in a given material. The shape constant K depends on the shape of the holes and their distribution pattern, with values of K = 0.282 for square holes in a rectangular array, K = 0.238 for round holes in a hexagonal array and K ~ 0.26 for hexagonal holes in a hexagonal array (30).

Note some interesting properties of equations 1 and 2. The spatial resolution of the parallel hole collimator changes linearly with the distance of the source from the collimator, while the efficiency does not depend on this parameter. This is because the efficiency of a single hole decreases as b^2 as b increases, while the total number of holes that the photon can possibly pass through the collimator increases as b^2 as b increases, so these two factors cancel each other. Note that the resolution depends directly on the factor $\frac{d}{l_e}$, while the efficiency depends inversely on $(\frac{d}{l_e})^2$, which means that the collimator resolution can only be improved at the expense of collimator efficiency. As a final remark and an order of magnitude example, for a typical high efficiency low energy collimator with a hole diameter of 0.25 cm, hole length of 2.5 cm, septal thickness of 0.03 cm and hexagonal hole shape, the resolution at b = 0 and efficiency are 0.25 cm and ~ 6×10^{-4} respectively (41).

2.2 Hand-held SiPM gamma camera design

Based on the experience from a previous evaluation of a larger, arm-mounted MGC (42), our University of Virginia surgeon collaborators desired a more compact camera with a round shape for easier positioning in tight locations. Ideally, this camera would be capable of both hand-held and arm-mounted operation. Facilitated by the recent increased availability and lower cost of SiPMs, a round format, lightweight gamma camera was designed and built. In the following sections, the setup and hardware of the gamma system will be presented.

2.2.1 Gamma scintillator

The scintillator used in this gamma camera is a single crystal of 5 % cerium doped $LaBr_3$, commercially available as BrilLanCe 380 from Saint-Gobain Crystals, Hiram, OH. The crystal is 6 cm in diameter and 6 mm thick and is packaged in a hermetic aluminum package (visible at the bottom of the stack of components shown in Figure 7). The hermetic package has overall diameter of 7.5 cm and height of 9.5 mm and is necessary due to the hygroscopic nature of $LaBr_3$.

2.2.2 MPPC module

The SiPM array was built from eighty 3 x 3 mm² model S10362-33-050P MPPCs from Hamamatsu Photonics, Hamamatsu, Japan. Each MPPC has a 50 μm pixel pitch.

The MPPCs were arranged in a roughly circular pattern with a central 8 x 8 square array bounded on each side by a 1 x 4 array (Figure 6). The diameter of the printed circuit board (PCB) module is ~ 65 mm and the thickness is ~ 5 mm. The MPPC pitch is 6 mm. Although the inter-MPPC gaps are not minimized, this pitch is adequate to sample the broad light distribution of the $LaBr_3$ scintillator. The scintillator is coupled to the MPPC array using polydimethylsiloxane (PDMS) coupling compound to improve the scintillation light transfer to the MPPCs and insure a sturdy coupling between the SIPM board and the scintillator. Assembly of the MPPC array on the amplifier board was executed by Adaptive I/O technologies (Newport News, VA). In this setup, each MPPC is supplied with its own readout channel. Note that the reason for not placing the MPCCs closer to each other is to achieve a balance of performance versus cost.

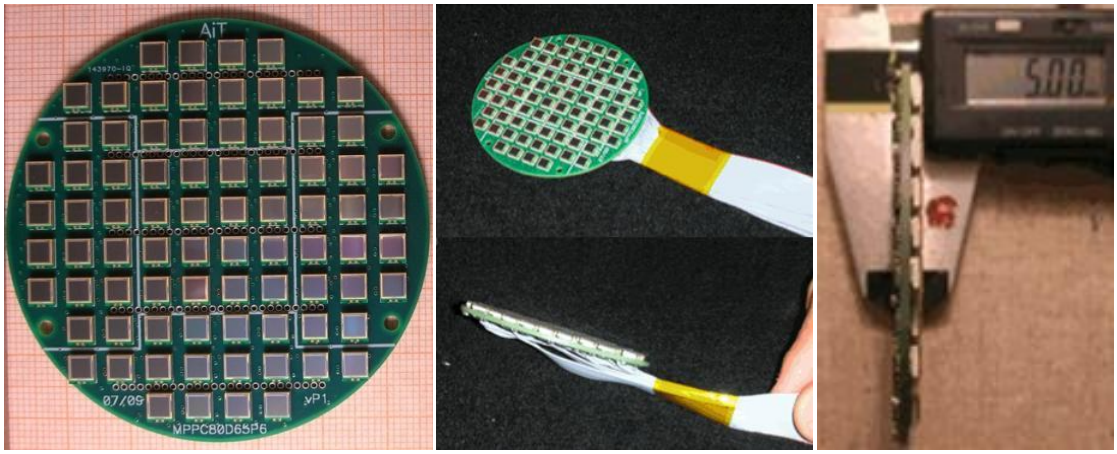

Figure 6: Hamamatsu MPPC arrangement of 80 units (left); module connected to the readout system (middle) and PCB thickness measurement (right) (43)

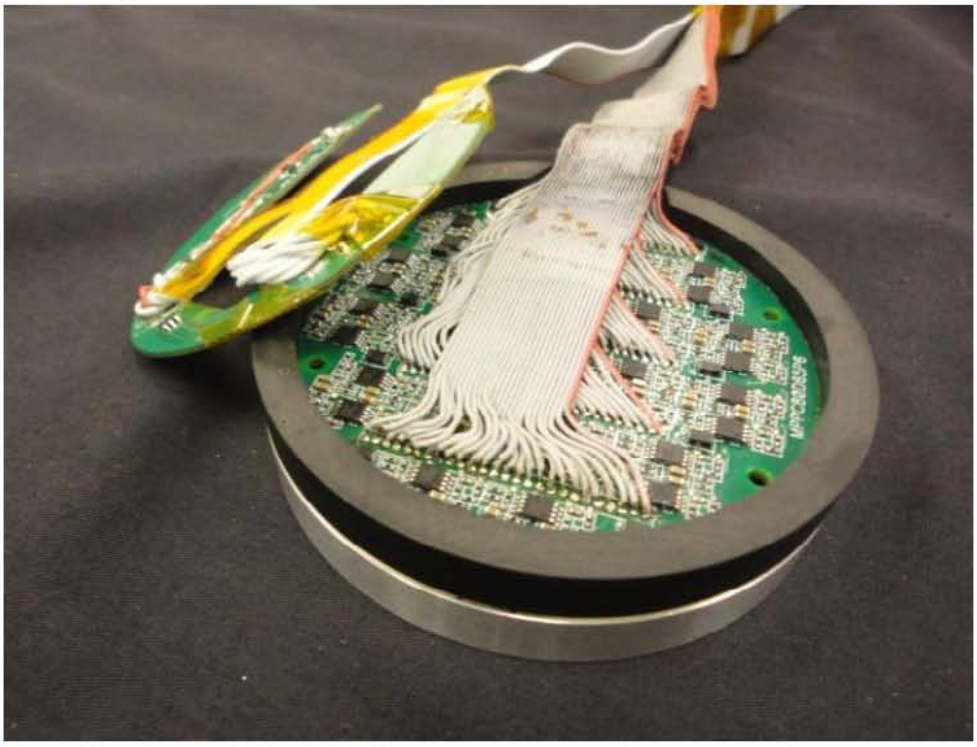

Figure 7: Back of the PCB with Hamamatsu MPPCs inside the delrin ring housing with cables leading to the readout electronics system

			1	2	3	4			
	1	2	3	4	1	2	3	4	
	5	6	7	8	5	6	7	8	
5	9	10	11	12	9	10	11	12	9
6	13	14	15	16	13	14	15	16	10
7	1	2	3	4	1	2	3	4	11
8	5	6	7	8	5	6	7	8	12
	9	10	11	12	9	10	11	12	
	13	14	15	16	13	14	15	16	
			13	14	15	16			

Figure 8: Map of five regions of 16 MPPCs powered by separate SIP90 power supplies

2.2.3 Power supplies for the SiPMs and the temperature compensation

To supply the bias voltage, the MPPCs are split into five groups of 16 MPPCs (Figure 8) with each group powered by a separate SIP90 power supply from EMCO High Power Corporation, Sutter Creek, CA (Figure 9).

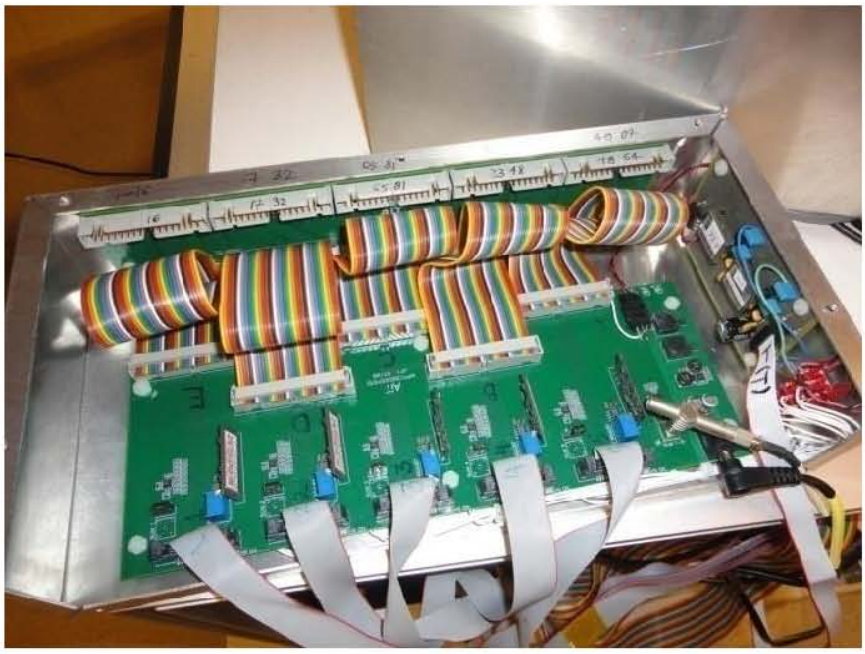

Figure 9: Power supply box for the MPCC array with SIP90 power supplies along the bottom of the photo and the Hamamatsu power supplies and the temperature compensation circuit on the right

The temperature effects on the MPCC reverse voltage have been explored with the rapid development of the SiPM technology (44; 45). With the decreasing bias voltage, the photopeak position also decreases and this effect can be seen in Figure 10 (decrease by a factor of about two in 10 ºC). The instability of the photopeak position in human studies in the OR can lead to false negatives if the peak moves too low and outside the

energy acceptance window (the photopeak position data from the clinical SLNB study will be shown in chapter 5). This is an unacceptable variable in human studies, and the implementation of a temperature compensation circuit is necessary. To avoid these temperature related issues, Hamamatsu C11204(X) high voltage power supplies can be used, providing up to 90 V output (Figure 9). This allows for more precise matching of the gains and improved energy resolution performance of the camera overall.

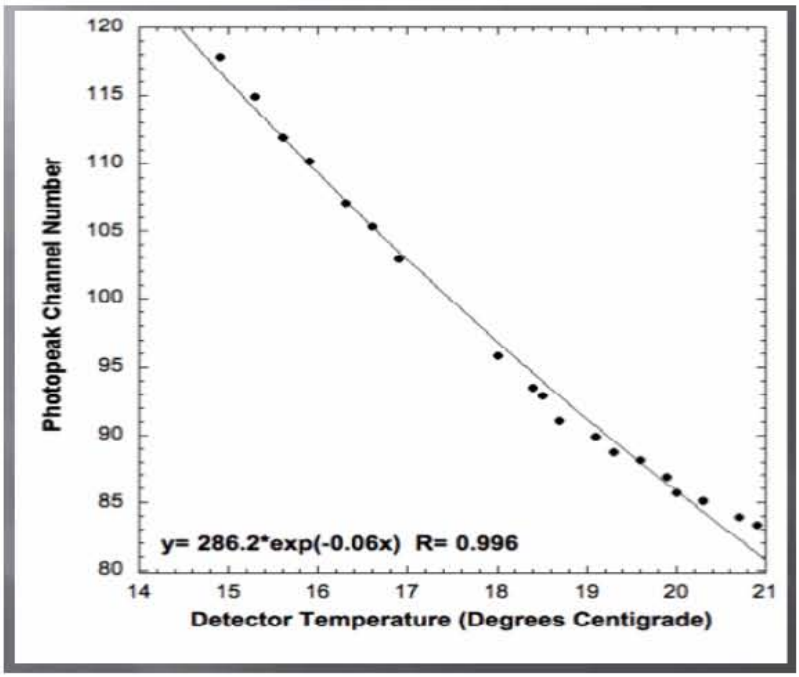

Figure 10: Hamamatsu MPPC temperature effects - photopeak position vs. temperature of the MPPC (43)

Each Hamamatsu power supply has an integrated microcomputer with an automatic temperature compensation function. This temperature compensation method allows the MPPC gain to be kept constant by changing the reverse voltage according to the ambient temperature. Two LM73CIMK-0 (National Semiconductor Corporation) sensors have been mounted on a dedicated PCB on top of the SiPM array inside the

camera housing to track the temperature (Figure 11). The formula for the temperature compensation is:

$$V = A\,(T\text{-}BASE) + V_c\,, \qquad \text{equation 3}$$

where V is the high voltage output, A is the temperature coefficient [V/ºC], T is the temperature of the sensor in the camera housing [ºC], BASE is the reference temperature [ºC] and V_c is the reference voltage [V] (46). The default values in equation 3 for the two Hamamatsu power supplies are a temperature coefficient of 0.056 V/ºC and reference voltages of 72.5 and 72.7 V respectively at room temperature of 25 ºC.

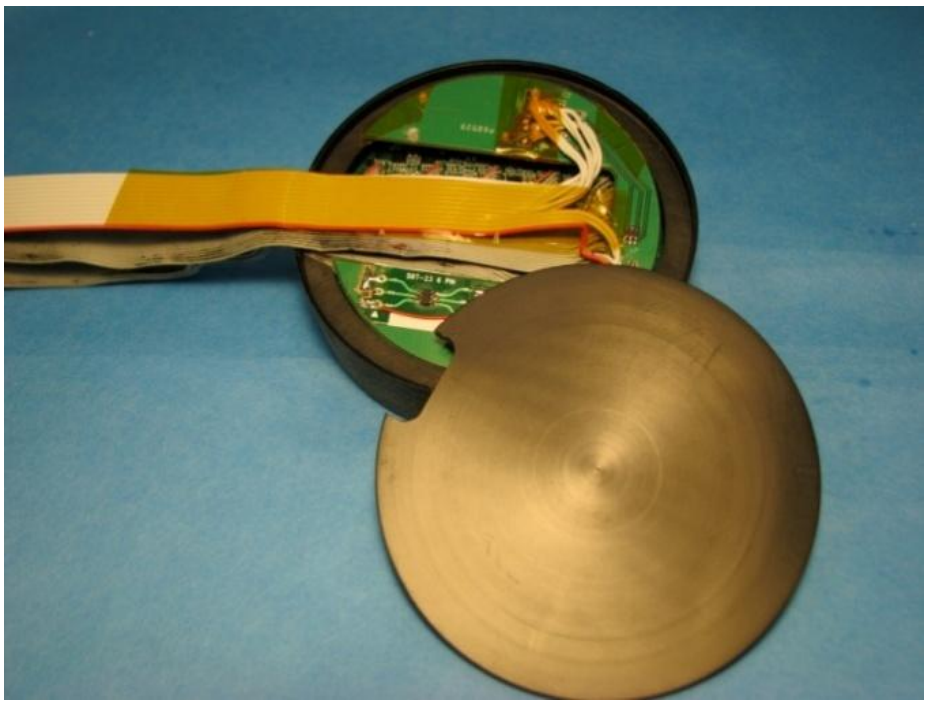

Figure 11: Gamma camera assembled with the temperature sensor board on top

2.2.4 Electronics readout system

The sum of the signals from the eighty SiPMs is sent to a leading edge discriminator (Figure 12) whose input is buffered and amplified by a wide bandwidth op-amp and then compared to a potentiometer-set threshold in a high speed comparator MAX901. The output of the comparator triggers a one-shot circuit which generates a potentiometer-controlled pulse. A second one-shot circuit is also triggered which inhibits re-triggering the first for a fixed time period, thereby avoiding undesirable ringing trigger response. Two user-controlled potentiometers control the threshold and the dead time. Depending on these parameters and the activity of the source measured, effects like pulse pile-up and loss of counts due to high count rate may occur. The final output signals a trigger for the ADC conversion. The camera analog data is read out by two high speed FPGA-based multichannel data acquisition (DAQ) modules designed and built by AIT Instruments, Newport News, VA: one with 64, and a second one with 16 ADC channels (DAQ6400U and DAQ1600U respectively) (47). The 16 channel module reads the four outer groups of 4 MPPCs, while the 64 channel module reads the inner square group of 8 x 8 MPPCs. The ADC module's design permits event timing synchronization via CAT5e connection between the units (48). The ADCs transmit conversion data over USB to the acquisition computer where the core acquisition functions are performed with custom-written software. Basic data acquisition functionality is implemented with a set of Java based routines, and Java extensions are used to interface with a graphical user interface (GUI). The GUI is written in the data acquisition programming environment Kmax (Sparrow Corporation, Daytona Beach, FL). Java modules are used for energy and center

of gravity (COG) position calculation, while the GUI displays the raw and the uniformity-corrected images with an ability of applying various energy or positional conditions. The GUI will be described in more detail in chapter 4. The schematic of the hardware described in the previous paragraphs can be seen in Figure 12.

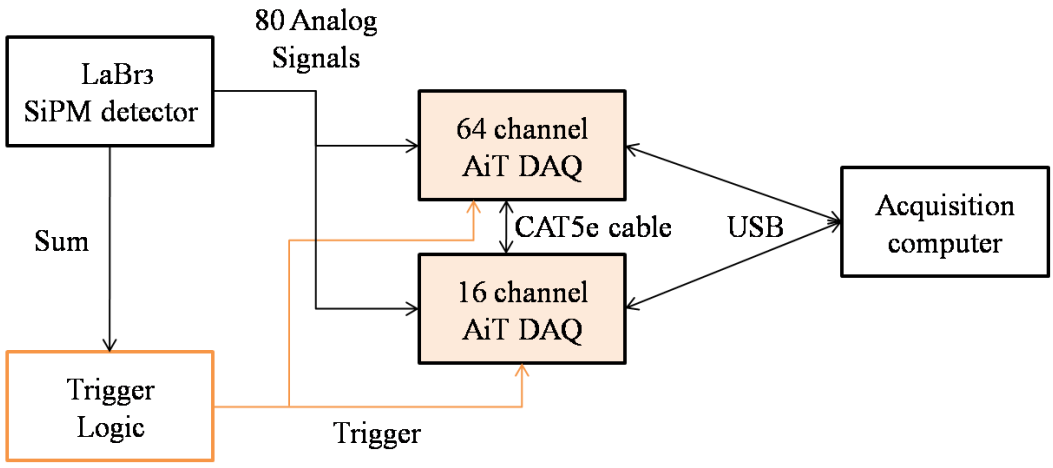

Figure 12: Schematic of data acquisition hardware used to read out the SiPM gamma camera

2.2.5 Camera assembly and housing

The outside housing for the gamma camera was designed and built in Thomas Jefferson National Laboratories out of CMW-1000 machinable tungsten. There is an inside housing layer (Figure 13) made out of black Delrin (polyoxymethalyne) that has a dual purpose – it seals the scintillator, MPCC board and the temperature sensor board from light leakage, and it also improves the sturdiness of the gamma camera by eliminating possible movement of components within the tungsten housing during hand-held operation.

Figure 13: Delrin light shield housing

Figure 14: Demonstration of hand-held operation of the gamma camera

2.2.6 Parallel hole collimator

The camera is equipped with a custom designed tungsten-polymer composite two-part collimator fabricated by Mikro Systems (Charlottesville, VA) with an active diameter of 60 mm and overall diameter of 75 mm. The collimator has a unique magnet-based quick assembly/disassembly alignment mechanism (49) that allows precisely aligned stacking of two layers of the collimator to accommodate either high resolution (two-layer) or high sensitivity (single layer) imaging (Figure 15).

Following equation 1 and equation 2, the system and collimator performance were designed to be comparable to a conventional gamma camera while keeping size considerations in mind and keeping the weight of the camera down. The collimator hole pitch was chosen to be 1.0 mm in order to assure that the collimator geometric blurring had minimal impact on the overall camera spatial resolution.

Figure 15: Parallel hole collimator with the magnetic locking mechanism on the perimeter

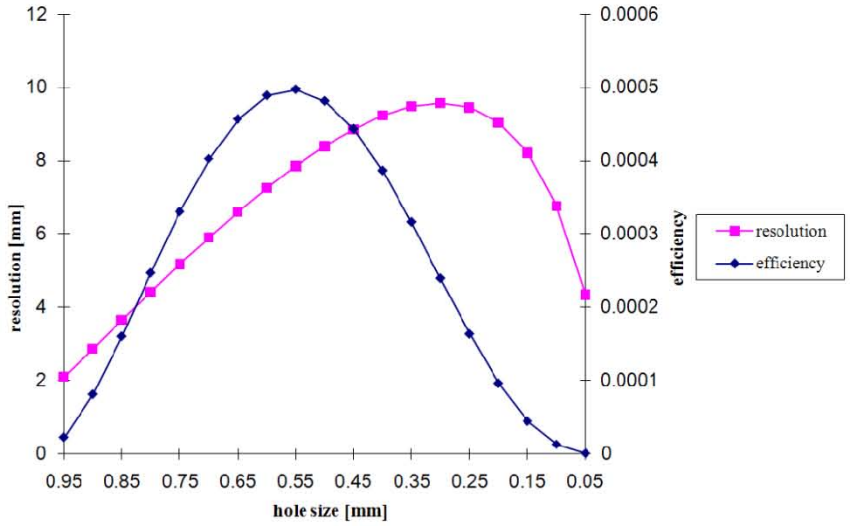

Figure 16: Collimator efficiency and resolution versus the hole size

Figure 16 contains plots of the theoretical collimator efficiency and spatial resolution for a 1.0 mm hole pitch, with varying hole size. For each hole size, the hole length was adjusted to result in a 5 % septal penetration (30). This figure shows that, given above mentioned constraints, the maximum geometric efficiency (4.8×10^{-4}) occurs for a hole size of 0.6 mm. The corresponding hole length is 5.5 mm, which was on this basis chosen as the single layer thickness. Figure 17 plots the collimator spatial resolution and geometric efficiency for changing hole length. Two vertical red lines show the length corresponding to one and two layers. The figure shows that for a single layer operation, the collimator resolution at a source-to-collimator separation of 5 cm is 7.2 mm FWHM and the geometric efficiency is 4.8×10^{-4}. For two 5.5 mm layers stacked, the resolution becomes 3.7 mm FWHM and the collimator geometric efficiency is 1.0×10^{-4}. The corresponding theoretical septal penetration of the collimator for these particular hole lengths is then 4.5 % and 0.2 % respectively.

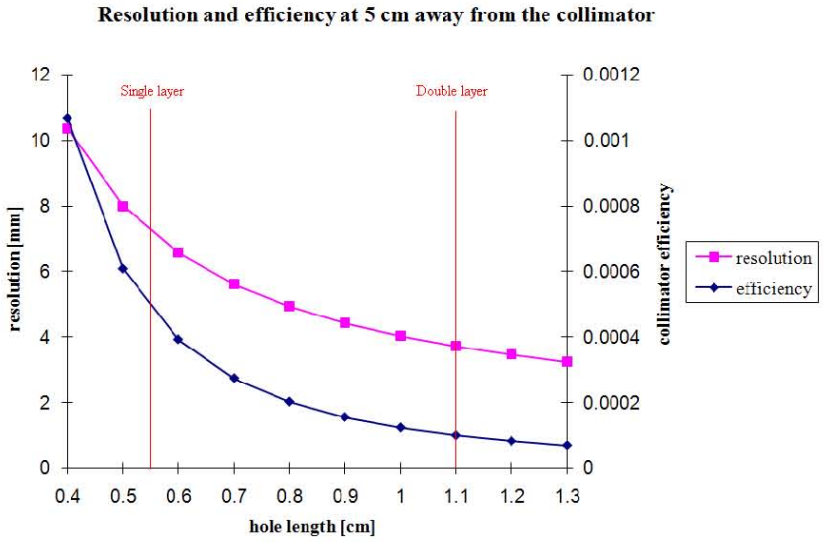

Figure 17: The efficiency and resolution trade-off with single versus double collimator layer

The linear attenuation coefficient of the tungsten polymer material that was used to manufacture the collimator for the gamma camera was measured using thin tungsten polymer samples acquired from Mikro. A small acrylic lesion (9.9 mm OD) was filled with a ^{99m}Tc-pertechnetate solution (activity of 37 MBq) and positioned 1 cm above a 40º acceptance angle 1 mm diameter pinhole collimator from Mikro. The pinhole collimator material was otherwise comprised of 10.6 mm thickness tungsten and covered the parallel hole collimator of the gamma camera completely. The available tungsten samples ranged in thickness from 170 µm to 530 µm and were combined to produce materials of thickness up to 2 mm in between the source and the pinhole collimator to cover the pinhole collimator completely. The ^{99m}Tc-pertechnetate source, pinhole collimator and the gamma camera were at fixed relative positions during this experiment. For each thickness of the material, an image was acquired for a fixed amount of total counts in the image and saved. The thicknesses of the material were 170, 330, 530, 780, 1000, 1310,

1530 and 1860 µm. For each acquired image, the sum of the counts in a fixed circular ROI centered on the image of the acrylic lesion was measured and plotted against the thickness of the tungsten.

The linear attenuation coefficient of the tungsten polymer was calculated to be 18.7 cm^{-1} in this experiment. This value differs slightly from the expected value of 21.9 cm^{-1} used in the original collimator design calculations. The reduced linear attenuation coefficient negatively affects the septal penetration of the collimator which was targeted to be less that 5 % for one collimator option as described in previous paragraphs. With the manufactured dimensions of the collimator, the new theoretical septal penetration becomes 7.6 % using the new measured linear attenuation coefficient. This measured value of the linear attenuation coefficient of 18.7 cm^{-1} will be used in further theoretical calculations and discussion.

The overall system size and mass of the camera are about 40 mm thickness and below 1.4 kg (Figure 18), which permits comfortable hand-held use by the surgeons in the OR (Figure 14).

Figure 18: Physical characteristics of the assembled gamma camera

CHAPTER 3: VISIBLE/NIRF MODALITY

The core of the visible/NIRF modality consists of a two charge coupled device (CCD) camera and NIR light excitation subsystem that facilitate the excitation and detection of NIR light being emitted by fluorescent tracers that are injected in the patient. In this section, the principles of NIRF imaging, detection and interaction with matter will be described, as well as the hardware used to construct the visible/NIRF subsystem.

3.1 Visible/NIRF imaging

Visible imaging in the form of macroscopic observation of patients by doctors or surgeons is one of the oldest imaging methods used in clinical practice. With the discovery of microscopes, visible imaging on a microscopic level has added a whole new dimension to medicine, biology and life sciences. Ever since, the microscopy continues to be the gold standard in visible imaging with many novel techniques developed over the recent years. At the same time, macroscopic optical fluorescence imaging has re-emerged as a valuable tool for research and clinical and surgical practice, most intriguingly in the near infrared (NIR) part of the spectrum. It has been long known (50; 51) that the light in the NIR part of the spectrum is prone to penetration in tissue to a higher degree compared to visible light, which is crucial to the design and development of the visible/NIRF system described in this dissertation. Furthermore, there has been a rapid development of high quality and high detection sensitivity visible and NIR imaging components in recent

years. Coupled with increasing availability of fluorescent targets and probes, this allows for compact, portable and moderately expensive options for research and further advancement and refinement of present imaging techniques. Main advantages of fluorescence imaging are high sensitivity, long term tracer stability post labeling, low hazard in terms of radiation dose and possibility for multi-fluorophore detection with the appropriate tools. In a recent review of in-vivo near infrared fluorescence imaging, Frangioni (52) outlined the most important parameters for successful in vivo NIR fluorescence imaging overall. Furthermore, translation of NIRF imaging specifically to imaging in clinical trials has been reviewed by Sevick-Muraca (53; 54), citing increasingly positive clinical experience. Following Frangioni's discussion on significant imaging system specific parameters, the means of excitation light delivery and collection of emitted fluorescence as well as the hardware relevant to these parameters will be discussed in the following sections.

3.1.1 Principle of fluorescence

Fluorescence is a process of light emission by certain molecules (fluorophores) after they have absorbed light or other form of energy. It is a form of luminescence and is usually a result of a three-stage process illustrated by the electronic state diagram in Figure 19 below. Initially, the fluorophore is in its ground state S_0, and is supplied energy from an external source, usually in the form of light. With the energy being absorbed by the fluorophore, the electrons from the ground state are excited into one of the vibrational levels of an excited singlet state. This excited state exists for a short amount of time (on

the order of 10 ns), during which the electron is subject to losing some energy, due to interactions with its environment among other processes that can depopulate S_1. The photon is then emitted spontaneously when the fluorophore returns from the lowest vibrational level of the excited singlet state S_1 to the ground state S_0. Due to the energy losses mentioned above, the energy of the photon emitted is lower (and wavelength longer) compared to the photon that was absorbed. The difference in these wavelengths (maxima of the absorption and emission spectra of the same electronic transition) is called the Stokes shift, and gives us information about the fluorophore environment and its interactions. The Stokes shift is an essential parameter in designing the light excitation and collection subsystem of an optical fluorescence system.

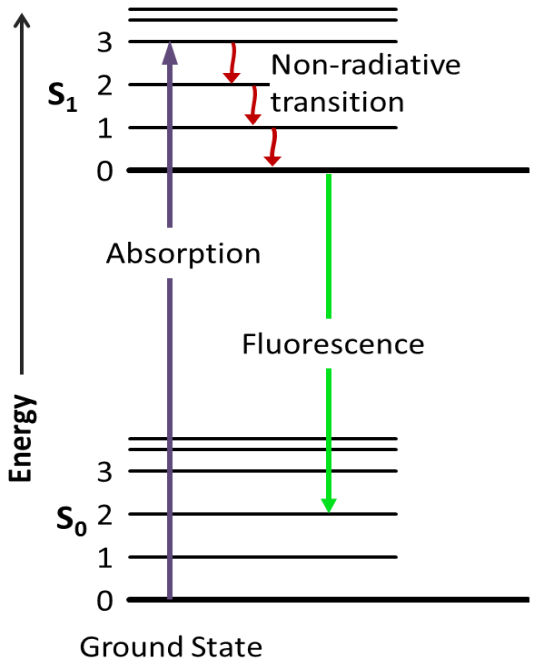

Figure 19: Jablonski diagram showing the excitation of an electron after absorbing a high energy photon. The electron fluoresces at a longer wavelength compared to the absorbed photon (55)

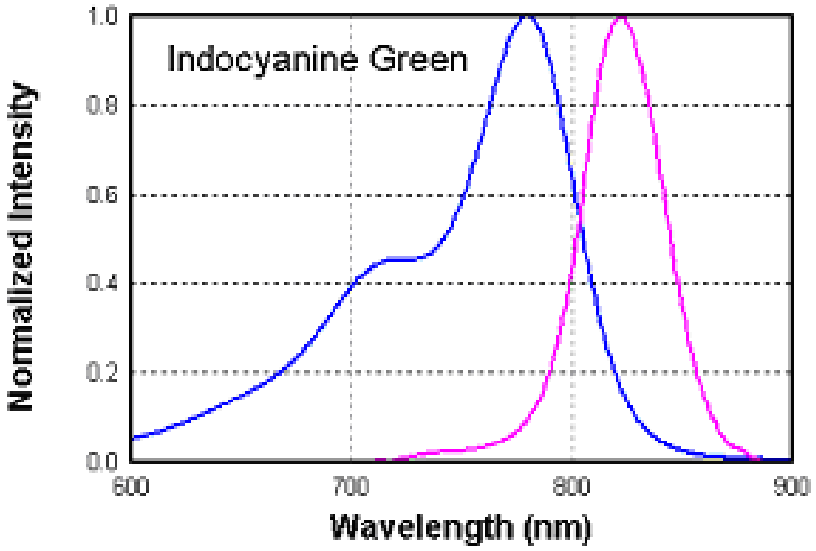

Figure 20: Absorption (blue) and emission (purple) spectra of indocyanine green (ICG) in water (56)

Some of the important characteristics of fluorophores are the excitation (absorption) and emission spectra, quantum yield and quenching properties and limits. The spectrum of the excitation light should be close to the peak and shape of the absorption spectrum of the fluorophore to allow for optimal excitation. The emission spectrum is usually a mirror image of the longest wavelength part of the excitation spectrum (example for indocyanine green (ICG) in Figure 20), shifted by the fluorophore's Stokes shift towards longer wavelengths. The quantum yield is an important parameter in this process, being an efficiency measure to compare the amount of the photons emitted to the number of photons absorbed. It is also worth mentioning quenching here, which is a loss of fluorescence signal due to short-range interactions between the fluorophore and the environment. Self-quenching occurs for example when the concentration of the fluorophore in a solvent is too high. Other examples of quenching can include chemical effects as well as illuminating the fluorophore with too much light (photobleaching), which will be discussed in the following sections. The type

of a solvent can also have a strong effect on the shape and position of the excitation and emission spectra of a fluorophore (57).

3.1.2 Planar (epi-illumination) imaging

The most common, and one of the simplest methods of fluorescence imaging consists of collecting the fluorescence emitted towards the camera by fluorescent objects that were illuminated by a plane wave. This method is usually referred to as planar epi-illumination imaging, which is of most relevance to this dissertation in which the illumination source and the camera are located on the same side of the target object. In this imaging method, the excitation light of appropriate wavelength reaches the surface of the object being imaged and can propagate for several millimeters under the surface to excite shallow and sub-surface fluorophores. The fluorescence light from the fluorophores is emitted in an isotropic fashion and a part of it can be captured by an appropriate detector.

Epi-illumination methods utilizing the NIR part of the spectrum have gained popularity in recent years, with several research groups developing imaging systems with good results in animals and bench-top imaging (58; 59; 60; 61). The advantages of this imaging method are ease of development and possibility for high excitation light output which is proportional (to a point) to the intensity of the emitted fluorescent light. This method also has good intraoperative translation properties in terms of ease of operation (it does not require limiting patient motion or positioning), and is in general more safe than some other optical methods from the excitation light standpoint as it can use

incoherent light sources for excitation instead of lasers. However, similar to all planar imaging methods, epi-illumination cannot resolve depth nor account for nonlinear photon diffusion due to propagation in human tissue, and it does not account for shielding of the deeper fluorescent targets by the more superficial ones. Given the low penetration ability of the NIR photons in human tissue, the shielding issue is not a significant problem compared to imaging with a gamma probe.

3.1.3 Therapeutic window and NIR light penetration in tissue

Photon propagation in human tissue is characterized by the absorption and scattering properties of the tissue, which determine the amount of photons transferred between two points within the tissue. The absorption and scattering of light depend strongly on the composition of tissue as well as the wavelength of light travelling through it. The NIR therapeutic window defines a range of wavelengths where the penetration of light is at maximum in tissue. This occurs in the near-infrared part of the spectrum, more specifically between about 700 nm and 900 nm, and is caused by the lower absorption and autofluorescence of tissue in this region. Autofluorescence of tissue is lower in this NIR region (52) compared to visible and UV regions because of lack of endogenous fluorophores which allows for low background during imaging and consequently higher signal to background ratio when imaging desired fluorescent targets.

Absorption in tissue is a physical process in which the energy of the photon is taken up by the atoms of the transporting medium; depending on the energy gap of molecules in tissue, the energy of the photon can be absorbed or converted into

vibrational energy of the electrons in the atoms. The absorption can be modeled by Beer-Lambert's law, which states that the measured intensity of the transmitted light through tissue is governed via the inverse exponential power relation as follows:

$$I = I_0 e^{-ax} \qquad \text{equation 4}$$

where a is the linear absorption coefficient. Major photon absorbers in living tissue are hemoglobin, water and fat (lipids). From Figure 21 we can see that the absorption coefficient reaches minimum for these absorbers within the therapeutic window, which is also true for other endogenous chromophores in tissue like melanin or porphyrins.

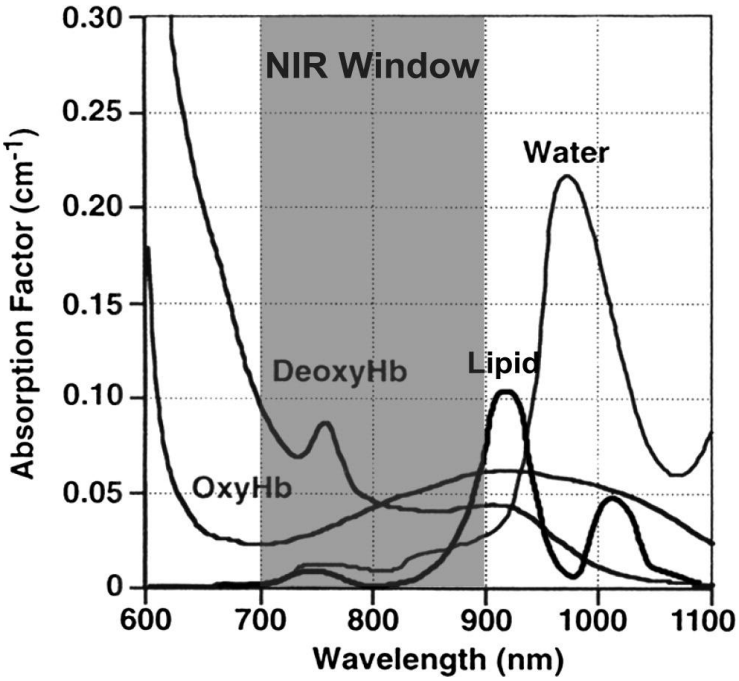

Figure 21: NIR therapeutic window is deemed ideal for optical fluorescence imaging due to the minimum in the value of the absorption coefficient (62)

Scattering is the second key factor that hinders photon propagation, and is a physical process by which photons interact with matter, causing them to deflect their path from their initial direction after an interaction event. The anisotropy factor g is important in this concept, defined as the mean cosine angle of the scattering angle θ between the directions of the photon before and after the scattering event. Compared to absorption, scattering is a much bigger contributor to photon attenuation in tissue and is dependent on many variables, including the size of the scattering particles in tissue, wavelength of incident light and the inhomogeneities in tissue. Both elastic and non-elastic scattering events can cause photon attenuation, but in general, the major types of scatter (Mie, Rayleigh) tend to be weaker in the NIR portion of the spectrum (62). Furthermore, for most human tissue the anisotropy factor g is typically high (63), being in the range of 0.95 for most normal tissue, 0.77 for adipose tissue and about 0.63 for some tumors. The scatter is thus highly forward-peaked which further aids propagation of photons deeper in tissue. This suggests that there is a degree of blurriness that scattering introduces in the imaged position of the photon for a number of scattering events.

3.1.4 Visible/NIRF photon detection and image formation

Given all the imaging related advantages of the NIR light in the NIR therapeutic window discussed in the previous section, the reality is that the NIR light is invisible to the human eye, and a way to collect and detect the emission from the fluorescent targets needs to be available. Due to recent advances in semiconductor technology, charge coupled devices (CCDs) are becoming the dominant detection method in medical

imaging. The CCD was invented in 1969 by Boyle and Smith at the AT&T Bell Laboratories (64) and marked a major revolution in imaging device development. The CCDs are silicon-based circuits consisting of densely packed photodiodes that convert the light energy into electronic charge. In theory, when a photon of sufficient energy (higher than the band gap energy of silicon) strikes a silicon atom near a CCD photodiode, it produces a free electron and a hole in the silicon lattice is left vacant. The free electrons are then collected by potential wells deep inside the silicon. During a user-specified integration time period, these potential wells fill up with charge proportional to the intensity of the incident photons, acting as capacitors in a way. The measurement of the stored charge (readout) is accomplished by series of parallel and then serial transfers of accumulated charge to an output node at the edge of the chip, and is usually done concurrently with the next integration cycle. Once the charge packet is shifted fully by parallel shifts and reaches the end of the chip (serial shift register), it is shifted serially to an output amplifier and the voltage is digitized and stored off the chip.

In order to focus the image properly onto the CCD and collect the fluorescent light emitted from the imaging field efficiently, a lens is placed in front of the camera. Given the dynamic nature of the surgery, the optical system needs to have the flexibility to be operated at varying working distances. Therefore, a lens system needs to have the auto-focusing capability implemented so that the images at different working distance can be captured free of image blur.

3.1.5 Light emitting diodes (LEDs)

A success of an NIRF imaging setup depends a great deal on the intensity of its illumination source which is proportional to the fluorescent output. In the early days of fluorescence imaging, the investigators used filtered halogen lights to achieve adequate levels of illumination of the field of interest. However, the efficiency of halogen lights is rather low, with more than 90 % of the energy delivered by the lamp being converted to heat rather than the luminous output. Development of light emitting diodes (LEDs) led to replacement of halogen and incandescent lighting (broadband sources) as the LEDs use much less power at a higher efficiency percentage, thus alleviating heat problems. LEDs are in brief, semiconductor light sources consisting of a diode that is most commonly potted in plastic shells. When the diode is forward-biased, the potential barrier of the p-n junction becomes smaller and there is a charge flow between the two; the electrons recombine with electron holes and in that process a photon is emitted. This light is emitted isotropically, and light reflecting layers are usually placed below the p-n layer and on the sides to point the light forward. The wavelength of the emitted photons depends on the band gap of the materials that comprise the p-n junction and the dopant. LEDs usually emit light over a wider range of wavelengths compared to lasers, but much narrower than halogen and incandescent lights, whose large emission solid angle also means that most of the light they emit falls outside of the desired field of view. Concept of a figure of merit for judging efficient distribution of forward emitted light is the full width at half maximum (FWHM) and is shown in Figure 22. It is worth noting that the laser diodes are also an option for use in NIRF imaging as an illumination source, being

most spectrally and spatially confined of the above mentioned options. However, the downsides of high cost and complicated integration of laser diodes, especially concerning safety issues in terms of high exposure to the patient effectively rules them out for the imaging tasks concerned with in this dissertation. The high power delivered by the laser diodes is not necessarily a plus either, as fluorophores can undergo irreversible damage when illuminated with light of high intensity, a process called photobleaching (65; 66). For indocyanine green for example, this threshold is found to be around 50 mW/cm².

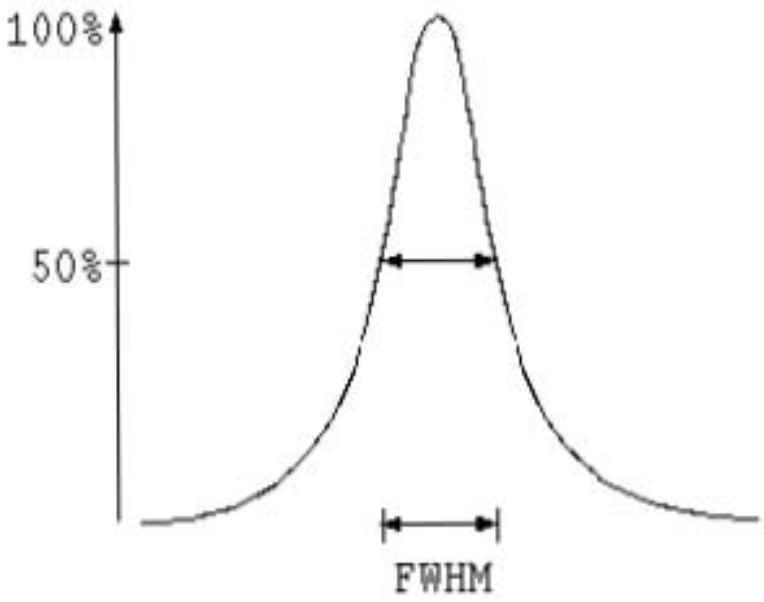

Figure 22: Full width at half maximum (FWHM) concept

3.1.6 Optical filters

Optical filters selectively transmit light of specific wavelengths and are usually positioned in the optical path of the light beam that needs to be filtered. They can be of absorptive (made with addition of organic or inorganic compounds that absorb the

unwanted light) or dichroic type (using sophisticated optical coatings to reflect the unwanted light using the interference principle). Filters are further separated into three major categories by filters that pass longer wavelengths only (longpass), shorter wavelengths only (shortpass), or a band of wavelengths, blocking the shorter and longer wavelengths with respect to the desired band (bandpass). Bandpass dichroic filters are of most relevance to the system described here, as the bandpass range of these filters can be finely controlled.

A successful NIRF imaging setup cannot be imagined without a proper filter set combination for successful rejection of unwanted backscattered illumination and stray light. The importance of filtering the collected light to visualize the true fluorescence from the target has been explored in more detail recently (67; 68) and has been deemed a crucial step in achieving acceptable signal-to-background ratio (SBR) of imaged targets. These studies stressed the importance of using high optical density (OD) filters, with OD values of over 5 in a NIRF imaging system setup, where OD is defined as a logarithm of the transmittance of the light through the filter. The reason for this is that the fluorophore emission signal can typically be five or more orders of magnitude less than that of the excitation illumination light. Hence, improper rejection of reflected illumination light can overwhelm the true emission signal if the OD of the filter is not high enough or if the filter OD curves overlap (Figure 23). This would cause a false background or even possibly a false focused signal in the final images, and therefore contribute to the poor SBR values or false positives. The manufacturing process and design characteristics of the filter play an important role in choosing the proper filter, as this determines the OD and the fall-off slope of the cut-ons and cut-offs of the bandpass filters.

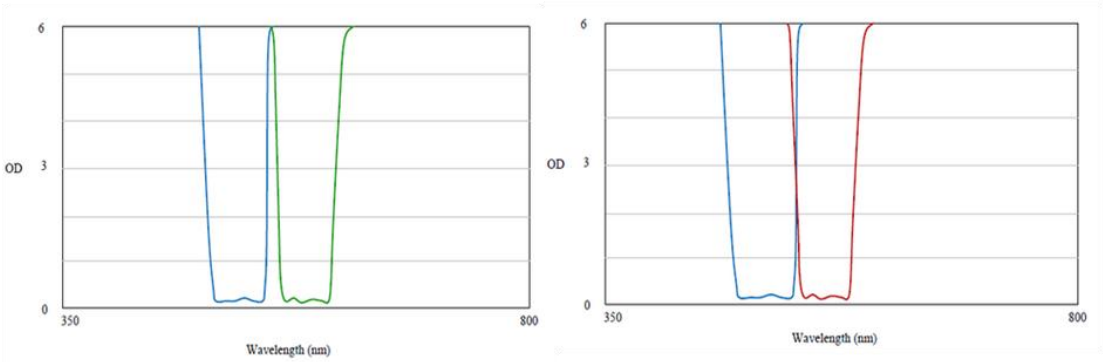

Figure 23: Appropriate (left) and inappropriate (right) blocking/attenuation characteristics of the excitation and emission filter pairs (69)

3.2 Visible/NIRF system setup

In the following sections, the setup and hardware of the visible/NIRF system will be described, following the design considerations discussed in the previous sections.

3.2.1 CCD camera

The heart of the visible/NIRF setup is a unique prism based multi-spectral AD-080CL CCD camera which can be seen in Figure 24 (JAI Inc., San Jose, CA). This camera uses two CCDs to image the visible and NIR portions of the spectra by using a shared optical path and a 1/3” dichroic prism that allows for precise separation of the visible (400-700 nm) and near infrared (700-1000 nm) spectra, seen in Figure 25 below. The camera has a small form housing of 55 x 55 x 80 mm, and also features a thread for standard C-mount lenses to allow for high lens flexibility. The camera uses standard Camera Link interface (70) for each CCD for serial communication with the computer

vision applications. The camera has a resolution of 800k pixels in a 1024 (h) x 768 (v) setup with a pixel size of 4.65 µm. The temporal resolution of the camera is up to 30 frames per second (fps), with several options for a shortened exposure time or faster frame rate up to 60 fps in partial scans. The camera is generally operated in a continuous (free-run) mode.

Figure 24: JAI AD-080CL multi-spectral 2-CCD camera (JAI Inc., San Jose, CA)

The CCDs that are used for color and monochrome imaging are respectively Sony ICX204AK and Sony ICX204AL chips. The ICX204AK chip is a 6 mm diagonal (type 1/3") progressive scan image sensor. It allows for RGB 24-bit or raw Bayer 10 or 8-bit output for visible light. The Bayer mask on the color CCD is an array of filters over the imager set in a characteristic Bayer mosaic pattern, where for each square of four pixels, one is filtered blue, one red and two green, as the human eye is most sensitive to green light. This allows each pixel to record information about only one of three colors. Demosaicing algorithms are then used to interpolate values for red, green and blue values

across the imager. The ICX204AK chip is similarly a 6 mm diagonal (type 1/3") progressive scan image sensor and it allows for 10 or 8-bit output for NIR channel. Note that both of these chips are high-precision bonded directly onto the prism assembly, which allows for crucial precise alignment between the visible and NIR images within one fourth of a pixel. This level of precision is hard to achieve with two separate cameras, and makes it very suitable for the imaging purpose of the system described here.

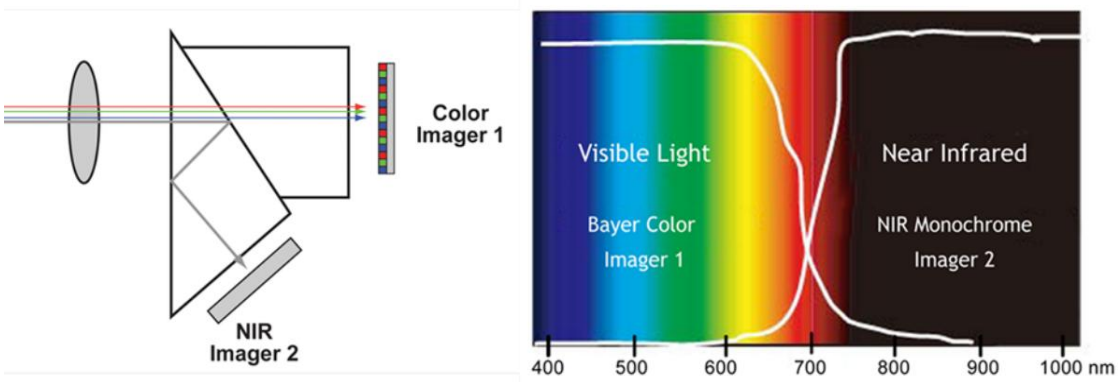

Figure 25: The dichroic coatings on the prism separate the color and NIR light information (left). The spectral curves show the transmitted light's spectral behavior (right) (JAI Inc., San Jose, CA)

The frame grabber board for transferring the data from the camera to the computer is a NI PCIe-1430 dual channel Camera Link image acquisition board from National Instruments, Austin, TX. The RGB CCD is connected to the Camera link channel 1 (port 0 in NI MAX) and has a 24 bit depth. The NIR CCD is connected to the Camera link channel 2 (port 1 in NI MAX) and has 8 bit depth. Reading, processing and display of acquired data is handled via custom developed NI LabVIEW software, which will be discussed in more detail in chapter 4.

3.2.2 Optical lens

Due to the optical prism design described in the previous section, the optical path to the two CCDs is not precisely equal, so the focus points for the visible and NIR area are slightly different from each other (Figure 26). Therefore, the camera manufacturer recommends using lenses designed for three CCD cameras which are characterized by minimal chromatic aberrations and large enough depth of field to allow for both visible and NIR images to be in focus at the same time. Furthermore, a requirement posed by the surgeons during the design stages of this system was that the working distance (WD) for the visible/NIRF system should be about 30 cm; this would allow them to have enough space below the camera to perform the surgery, while still having the camera image a large field of view within the surgical field. Additionally, it is important for the lens to have good transmission properties in the infrared portion of the spectrum to minimize the losses of the weak fluorescence signal.

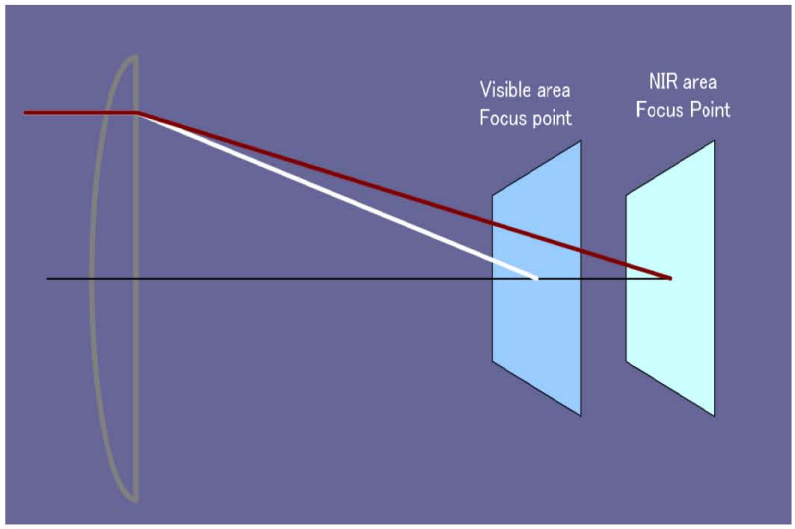

Figure 26: Visible and NIR focal points (JAI Inc., San Jose, CA)

To satisfy all these requirements, a Xenoplan 1.4/17 mm Compact C-Mount Lens from Schneider-Kreuznach (Bad Kreuznach, Germany) is used, with an 11 mm diameter image circle. The lens is broadband coated and corrected for uninterrupted imaging from 400-1000 nm (visible through NIR spectrum), making it ideal for the purpose of the system described in this dissertation. The spectral transmittance property of this lens is shown in Figure 27. The lens has a focal length of 17.6 mm and a f-number (ratio of the diameter of the lens aperture to the length of the lens) of 1.4, meaning that the aperture size is large and the light gathering properties of the lens are excellent; this was one of the key requirements in the design process due to the expected faint fluorescent signal that will be imaged with this system.

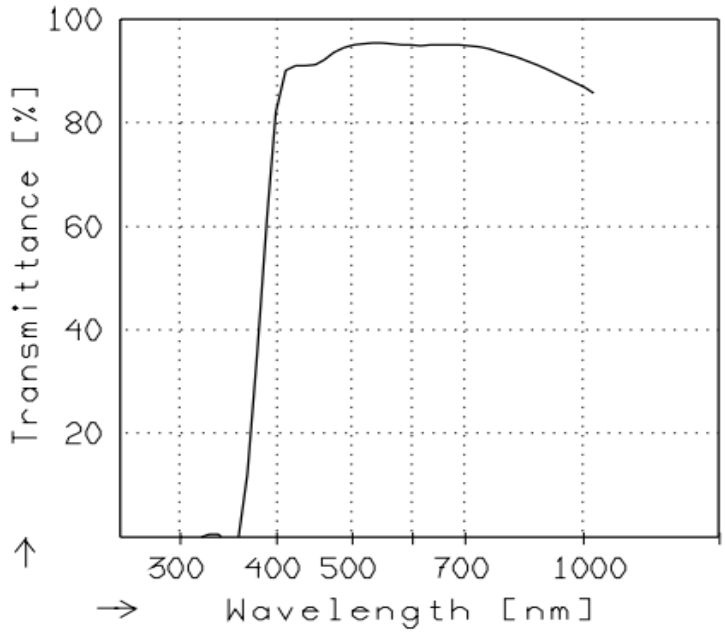

Figure 27: Spectral transmittance properties of the Xenoplan 1.4/17 lens (71)

3.2.2.1 Auto-focus subsystem

The nature of imaging in surgical procedures like the SLNB or tumor surgery is very dynamic in sense that the surgeon moves the imaging system in and out of the working area frequently. In the case of the gamma camera described in this dissertation, the sensitivity does not depend on the working distance; however, the resolution does degrade with working distance (which usually does not exceed several centimeters). In case of the optical imaging system, the surgeon can position the optical camera anywhere from 20 cm to 45 cm working distance, depending on the field of view they want to image. The Xenoplan optical lens described in the previous section does not have a depth of field that could cover this entire range without changing its focus, which means that the image of the object would not be acceptably focused on the CCDs in the entire range of these working distances. Hence, there needs to be a way for the surgeons to quickly and seamlessly re-focus the lens when they move the camera to a different location.

In terms of hardware and considerations in modifying the system to address this need, the lens needs to be focused remotely due to the sterility issues in the OR. For this reason, a computer controlled stepping motor from Velmex, Bloomfield, NY is used with a set of modified steel finished gears from McMaster Carr, Robbinsville, NJ that are connecting the motor and the lens (Figure 28). The gears (catalog numbers 6867K25 and 6867K19 respectively) were modified in such a way so the inside bore of the larger gear matched the diameter of the lens, while an additional cylindrical piece was added inside the smaller gear so it can fit and be driven by the stepping motor. In this fashion, the stepping motor and its controller (parts number PK245M-01AA and VXM-1

respectively) can be controlled by a custom written LabVIEW code to turn the gears in a desired direction and hence focus the lens as required by the surgeon.

Figure 28: The auto-focusing system connected to the lens and the camera (middle). Stepping motor (top) is connected to the lens via custom set of gears and is controlled by a Velmex controller (bottom)

There are two types of auto-focusing algorithms: the active approach, where the distance between the lens and the object is consistently monitored and the lens is focused to the necessary position accordingly, and the passive approach, where the distance to the object is unknown and the measure of focus is determined by analyzing the acquired image. To preserve the simplicity of the setup, a passive method is used in the system described here, utilizing the information from the Fourier transforms of the acquired images. When the image is in focus, the edges in the image are sharp, and this corresponds to image containing more of the higher frequencies in the Fourier space and

vice versa. Hence, a ratio of high versus low frequencies in the Fourier transform of the image is used as a merit value for determining when the image is in focus.

Using the principle described above, the lens is first focused to a starting (home) point that corresponds to the camera being at a WD of about 20 cm. The stepping motor and the gears are then driven through a series of pre-determined positions, 200 motor steps apart between each other. At the end of this path, the lens is focused to a point that corresponds to the camera being at a WD of about 40 cm. At each of the intermediate positions, a ratio of high and low frequencies in the Fourier transform is recorded in a temporary array. The lens is finally focused to a position which corresponds to the highest ratio in this array, and this whole process takes less than 20 seconds to complete. The auto-focusing routine is written in LabVIEW and the surgeon only needs to click the "auto-focus" button in the GUI every time they want to re-focus the image after moving the camera.

3.2.3 Illumination system

Two types of LEDs are utilized in the IMIS. Red, green and blue LEDs (RGB) are combined to produce white, NIR-free light for illuminating the surgical FOV, and high power near infrared LEDs are used specifically for excitation of fluorescent targets. In following sections, their utility and setup is described in more detail.

3.2.3.1 NIR LEDs and illumination uniformity optimization

The decision on LED illumination setup was arguably one of the most important parts of designing the IMIS. In consultations with surgeons and experience from previous surgical studies, it was determined that for the SLNB procedure, a FOV of approximately 10 cm x 10 cm at a working distance of 30 cm needs to be illuminated. Furthermore, it was crucial that the LED spectrum matches the absorption spectrum of the fluorophore (ICG) that will be used in clinical studies, being at the moment the only NIR fluorophore approved by the U.S. Food and Drug Administration (FDA) for use in human clinical studies. Therefore, four high power NIR LED modules L760-66-60 (Marubeni America Corporation, Santa Clara, CA) were selected. The L760 LED module is an epoxy lens type illuminator with an extremely high output made up of sixty high efficiency Aluminum Gallium Arsenide (AlGaAs) diode chips. These chips are packed tightly in a square fashion, mounted on a piece of ceramics on a metal stem and covered with clear silicone and epoxy resin. The whole package is very small in size (Figure 29) measuring less than 32 x 18 mm across. In terms of the electro-optical characteristics, each LED module has a maximum rated value of 750 mA of forward current for continuous operation at a typical forward voltage of 9 V, with total radiated power of 1000 mW at 600 mA test forward current. To operate the LED within the safe temperature range required by the manufacturer (30 ºC to 80 ºC), a heat sink is utilized to dissipate the heat away from the LEDs during continuous operation (Figure 30). The peak wavelength of the emission spectrum is at 760 nm with the FWHM of 30 nm and a large viewing angle of ± 60º. Note that this large emission angle at a WD of 30 cm would cover much more

than the necessary FOV, which would result in unnecessary spread of the LED light beyond the desired FOV. To focus the light from the L-760 LEDs into a narrower emission angle, a 25º FWHM lens (72) is placed in front of each LED. To optimize the illumination uniformity provided by the NIR LED and focusing lens setup over the surgical FOV, an optical engineering and design software package called LightTools from Synopsis, Pasadena, CA is used.

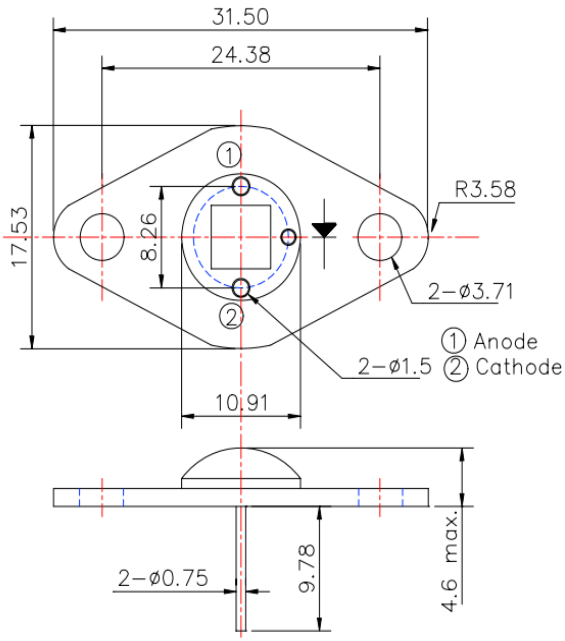

Figure 29: Mechanical drawing of the L760-66-60 LED module (dimensions are in mm) (73)

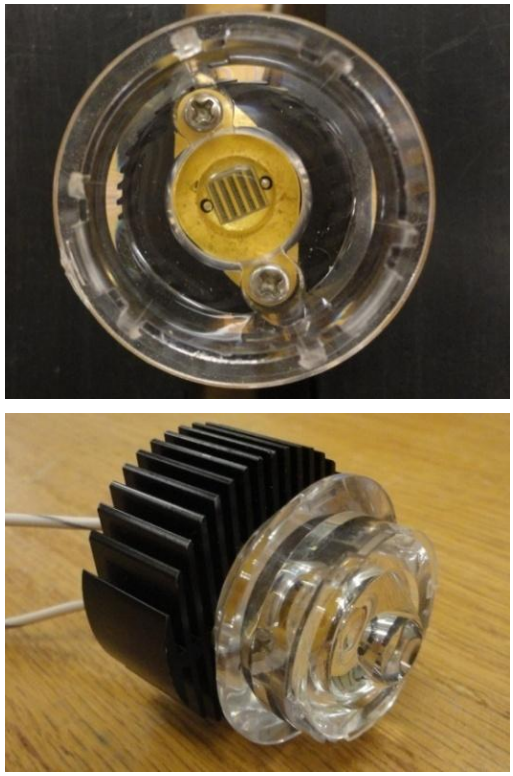

Figure 30: NIR LED photos showing a close-up of the LED array (top) and the assembled LED with the heat sink and lens (bottom)

3.2.3.2 RGB LEDs

The rejection of unwanted light is crucial for proper visualization of true fluorescent targets. However, initial experiments showed that the room and overhead lights in the operating room have a strong NIR component that saturate the NIR CCD (Figure 31), making it necessary to turn them off during the NIRF acquisition as it would not be practical to filter them at the source. This situation posed a need for white, NIR-free light to be provided to the surgical FOV during procedures in which IMIS is used.

Figure 31: NIR channel image of a hand illuminated with the OR overhead lights

Most of the 'white' LEDs available commercially are similar in operation principle to the fluorescent light – they use a phosphor material to convert the monochromatic light from a blue or an UV LED to a broad spectrum white light. This method is much simpler and cheaper than the alternative which uses a combination of red, green and blue LEDs to spectrally mix into white light. However, the phosphor-

based LEDs have a characteristic long tail-off in the IR region, so they are inadequate for the use in the OR as they would contribute unnecessary NIR background in the acquired images. Hence, three RGB Titan light modules (NT-53F0-0428, Lamina Lighting Inc., Westampton, NJ) are used in the IMIS, with each LED providing 418, 599 and 169 lumens respectively of red, green and blue light at 1 m WD and 1400 mA operating current. Similarly to the NIR LEDs, the RGB LED modules also have focusing lenses to confine the illumination light within the ± 30º region (part number OP-5LM3-0455) and large heat sinks (5.9" diameter by 1.2" thick) to guide the heat away from the LEDs (part number HS-5410-0537). The RGB LEDs are operated by three LED60W-043-C1400-D drivers from Thomas Research Products, Huntley, IL that help control the individual LED power output. The power and dimming circuit for three red LEDs in series is shown in Figure 32; the blue and green LED circuits are identical to the red LED circuit. One of the inputs of the power supplies for the LEDs (purple and gray wire in figure below) serves as a control for the 1400 mA current driver. A voltage divider with a 200 kΩ resistor and a variable resistor (user controlled potentiometer) is used with each color channel to control its individual output. The dimming option is available to offer an ability to modulate the relative intensity of the red, green and blue channels. This modulation effectively allows the appropriate change in the resulting color of the white light to comply with the International Electrotechnical Commission (IEC) requirements for white light illumination in the OR that will be discussed in more detail in chapter 6.

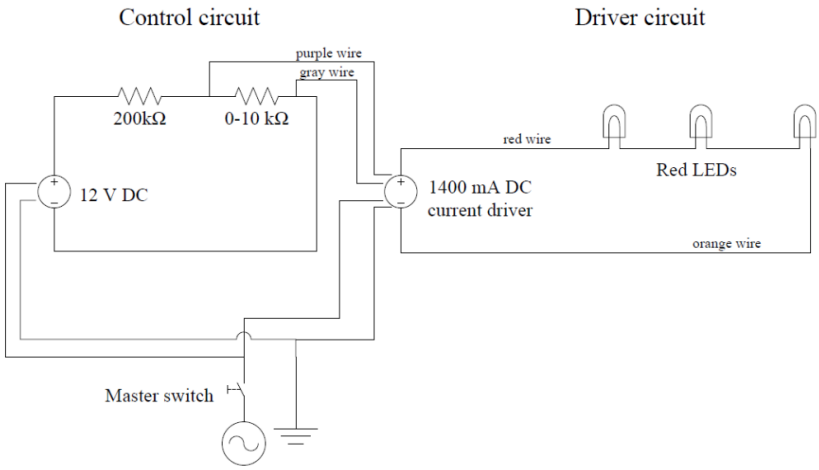

Figure 32: RGB LED dimming circuit for red LEDs (74)

3.2.4 Optical filters

As described in previous sections, the IMIS requires use of optical filters to provide surgeons with useful and meaningful data about the exact location and extent of the fluorescent targets they are looking to remove from the patient. The excitation filters are used in front of the illumination NIR and RGB LEDs and the emission filter is used in front of the optical lens. The reason the excitation filters are needed is to prevent the light from the LED that is in the range of the emission wavelength of the fluorophore being imaged from reflecting from the patient and passing through the optical lens and to the NIR CCD. The NIR LEDs have a FWHM of only 30 nm spectrally; however the tail-off of the emitted light does not fall sharply enough and has a significant component in the region above 800 nm. Thus, the IMIS uses a bandpass HQ760/20x excitation filter for the NIR LEDs from Chroma Technology Corporation in Bellows Falls, VT to ensure the unwanted reflected LED light is not collected by the NIR CCD. The peak of the

transmission band of this filter is at 760 nm with a FWHM of 20 nm and this particular filter reaches OD of 5 at 744 nm and 777 nm respectively (Figure 33 on the left). Regarding the emission optical filter, an important consideration to take into account is that some visible light needs to be passed through the same optical path as the NIR light to the visible CCD so the functional data from the NIR CCD can be overlaid on top of the structural map from the visible channel. The appropriate filter for this purpose is a HQ845/55m bandpass emission filter, with a peak of the transmission band centered at 845 nm and a FWHM of 55 nm. This filter reaches OD of 5 at 801 nm, and has a transmission band in the visible range; the OD falls below 5 at 601 nm and reaches 5 at 374 nm again (Figure 33 on the right), allowing adequate visible light to pass to the visible CCD for an appropriate structural map to be produced from the visible channel.

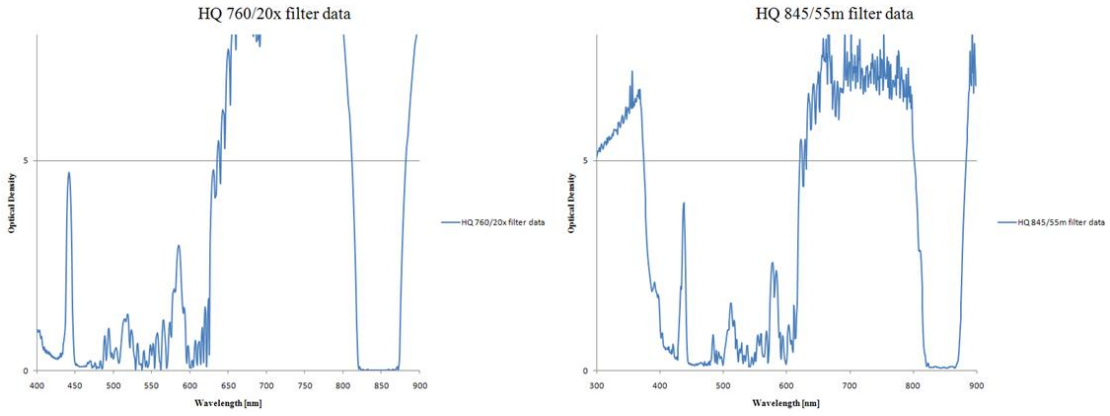

Figure 33: Optical density versus wavelength data for the excitation (left) and emission filter (right)

The excitation and the emission filters should reach the merit value of 5 close to each other like shown in Figure 23 if the filters' performance was ideal; however the optical density of an interference filter depends on the angle of the incident light. The performance of the filter can deteriorate drastically with the increasing incident angle of

the incoming light. At a specific wavelength, the OD of 5 can degrade to 2 or even lower even for the light incident at an angle of 10º (67; 75). The theoretical performance degradation with respect to the angle of incidence is shown in Figure 34. Due to this fact, the emission and excitation filters were chosen with the adequate gap between the points at which their optical density curves reach a value of 5 to account for any stray light that could geometrically be reflected from the NIR LEDs to the camera from the proposed surgical FOV of 10 x 10 cm^2.

Initial experiments with the RGB LEDs showed that these LEDs have a weak NIR component that can add a low level of unwanted NIR background to the NIR CCD during the NIRF acquisition. Similarly to the NIR LEDs, bandpass filters E650sp-2p from Chroma Technology Corporation were positioned in front of each of the RGB LEDs to reject any NIR light from contaminating the surgical FOV.

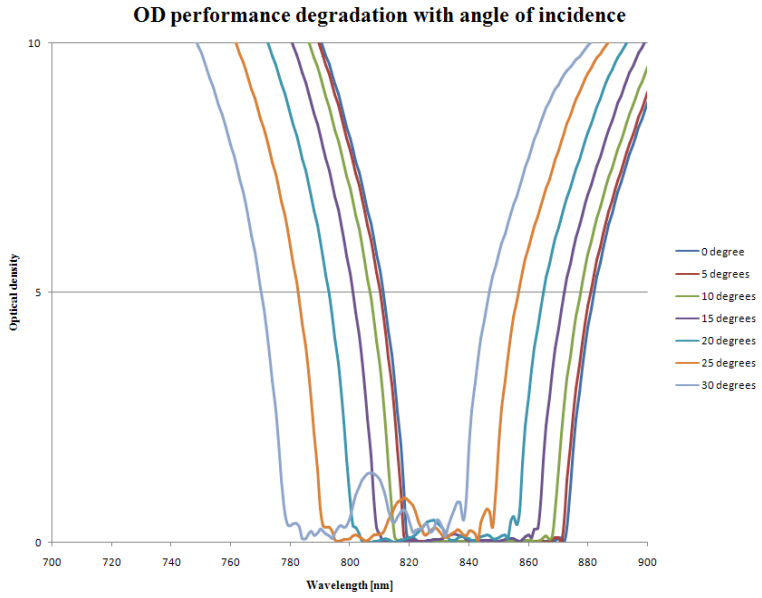

Figure 34: Optical density variation with changing angle of incidence (76)

CHAPTER 4: VISIBLE/NIRF AND GAMMA HARDWARE AND SOFTWARE INTEGRATION

The components of the visible/NIRF modality and gamma modality were described in detail in the previous two chapters. In the following sections, the task of integrating both modalities in a single mobile cart for logistics and operation convenience inside the OR will be discussed. Software integration between the modalities and the acquisition, processing and display of the acquired data as well as other control of the modalities will be described. Finally, hardware and software used to co-register the gamma and visible/NIRF images will be described to show how the information about the location and extent of the fluorescent and radioactive targets is presented intraoperatively to the surgeons in real-time.

4.1 Hardware integration of the optical and gamma modality

4.1.1 Mobile cart description

The IMIS is housed in a mobile cart previously used for a Captus 2000 thyroid uptake system (Capintec, Inc., Ramsey, NJ). The thyroid uptake system has been stripped down of its detectors, electronics, and calibration modules and the cart has been modified

to suit the needs of the IMIS with several shelves added inside the cart to house the IMIS hardware components (Figure 35).

Figure 35: IMIS components housed inside and on top of the mobile cart

In the figure above, the CPU that operates the IMIS subsystems is inside the cart on the left. The CPU is a Dell Precision T3400 Core 2 Duo machine with 32 bit Windows XP operating system installed, 3.25 Gb of RAM and a 300 Gb hard drive. The AiT 64 and 16 channel DAQ units described in chapter 2 are on the top right shelf, and the power supplies for the gamma camera subsystem are located inside the cart on the bottom right. The Velmex power controller and the RGB and NIR LED control boxes are located on top of the cart cabinet. The cart can be moved easily by the surgeons or medical staff in and out of the OR and has a suitably small enough form factor not to interfere with the standard OR logistics. The entire IMIS setup including both imaging modalities is shown in Figure 36 below.

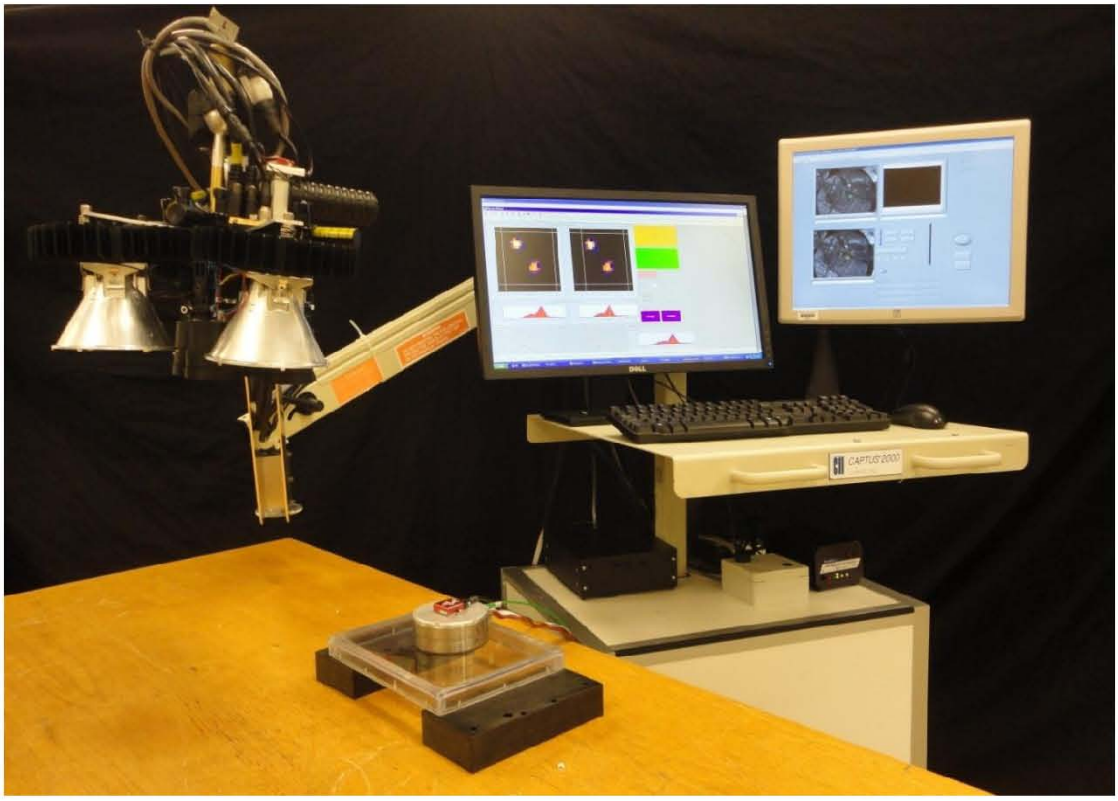

Figure 36: IMIS setup with the NIRF/visible system (left), gamma camera (bottom) and the mobile cart carrying the CPU and IMIS hardware (right)

4.1.2 Camera head adapter description

The adapter and the extension arm for the visible/NIRF camera were designed by the Jefferson Lab and are shown on the left of the Figure 37 below. The adapter between the arm and the camera head allows surgeons to rotate the camera head and the existing extension arm mechanism allows for the camera head to be moved up and down to image the target at various working distances as desired by the surgeons.

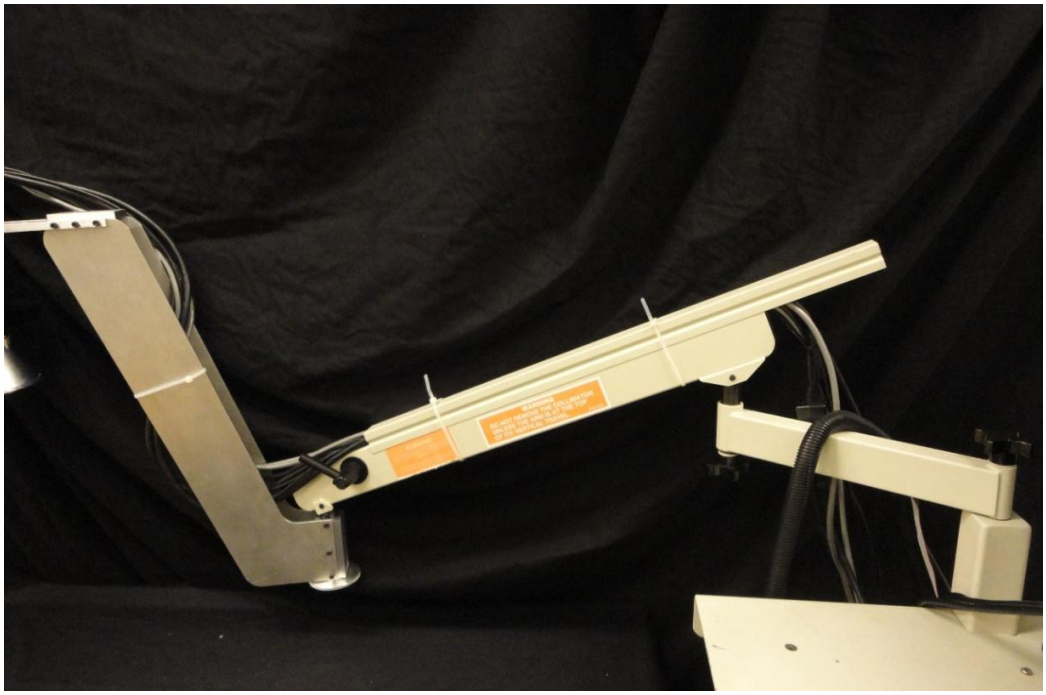

Figure 37: Adapter/extension arm for the visible/NIRF camera

The camera head with the auto-focus system and the optical lens is connected to the extension arm by a custom adapter that also holds the illumination LEDs (Figure 38) and allows for camera head rotation. The NIR LEDs are mounted to the radiating delrin bars on the camera head by a custom adapter and a handlebar mount (GRH30, GoPro/Woodman Labs Inc., Half Moon Bay, CA). The radiating bar setup and the handlebar mount allow sufficient degrees of freedom for positioning the LEDs in any desired fashion to satisfy the present procedure requirements and accommodate future applications. The handle for the surgeon is designed following the design of the standard handles for the overhead lights and similar intraoperative equipment in the OR, which allows the standard plastic sleeves to be fit over it for sterile intraoperative use.

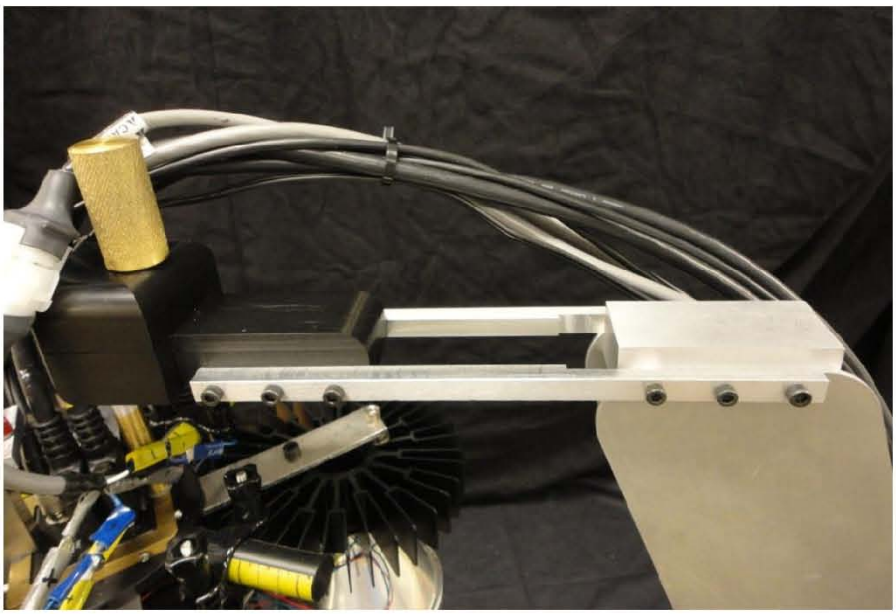

Figure 38: Adapter between the camera arm and the camera, the auto-focus system and the delrin radiating bar setup with the NIRF and RGB excitation lights

4.2 Software integration of the optical and gamma modality

In this section the GUIs used to acquire and display images for both the gamma and the visible/NIRF modalities will be described. The co-registration concept and the implementation of this feature in the GUI will be discussed in more detail.

4.2.1 GUI and software development for the IMIS modalities

The acquisition and the display of acquired data and control of all subsystems for the visible/NIRF modality is carried out through LabVIEW (Figure 39). This GUI was fully developed at University of Virginia. LabVIEW is an object based language, and the operation of the program is broken down into sections in the figure below.

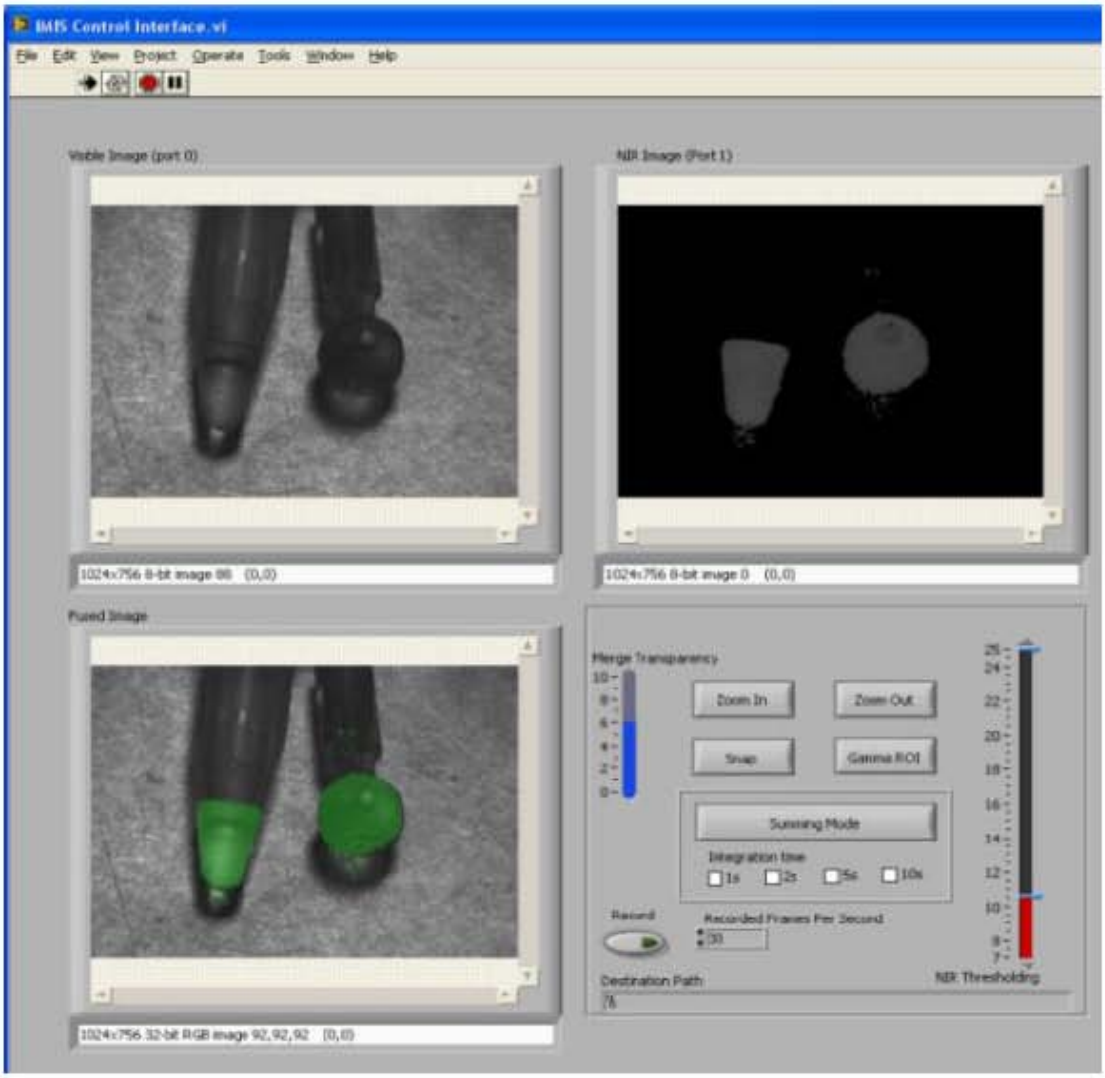

Figure 39: LabVIEW based GUI for the acquisition and display of the data from the visible/NIRF modality

The top left window in this figure shows a visible only image (grayscale), and the top right window shows the NIRF only image. The combined gamma, visible and NIRF image can be shown in the bottom left window, with fluorescence signal colored green and gamma outline (not enabled by the user in this example) colored red. The controls in the bottom right area allow the user to perform a range of visual adjustments to the combined visible/NIRF image, including changing the transparency of the NIRF image

and adjusting the window level of the NIRF image that is shown in the fused image. User can also choose to record the video from separate or combined channels, display the gamma image ROI if desired and save a snapshot of the active image for reference.

The gamma modality is controlled by the data acquisition programming environment Kmax (Sparrow Corporation, Daytona Beach, FL). Figure 40 shows the gamma camera GUI while imaging a patient during a clinical SLNB study described in more detail in chapter 5. The two imaging windows in the top row show a persistence mode image in the 10x binning mode (left) and a normal acquisition mode image in the 5x binning mode (middle). The buttons on the right in Figure 40 allow user to (from top to bottom) start and stop the acquisition, scale the display if the "automatic scaling" box is unchecked and clear the imaging windows. In the bottom row, the energy histograms for both images are shown and the limits on the energies of the accepted events can be adjusted to reject scattered events. The raw image is shown in the "Control Panel" tab, but this feature was deemed less desirable compared to the binned images by the surgeons during the clinical study due to the lack of clarity of the raw images caused by the low acquisitions statistics in a typical acquisition time of one minute. The sliders at the bottom of the energy histograms below the images are used for adjusting the persistence factor and timing threshold parameters for the persistence mode, which are active only if the persistence mode box is checked for each image respectively.

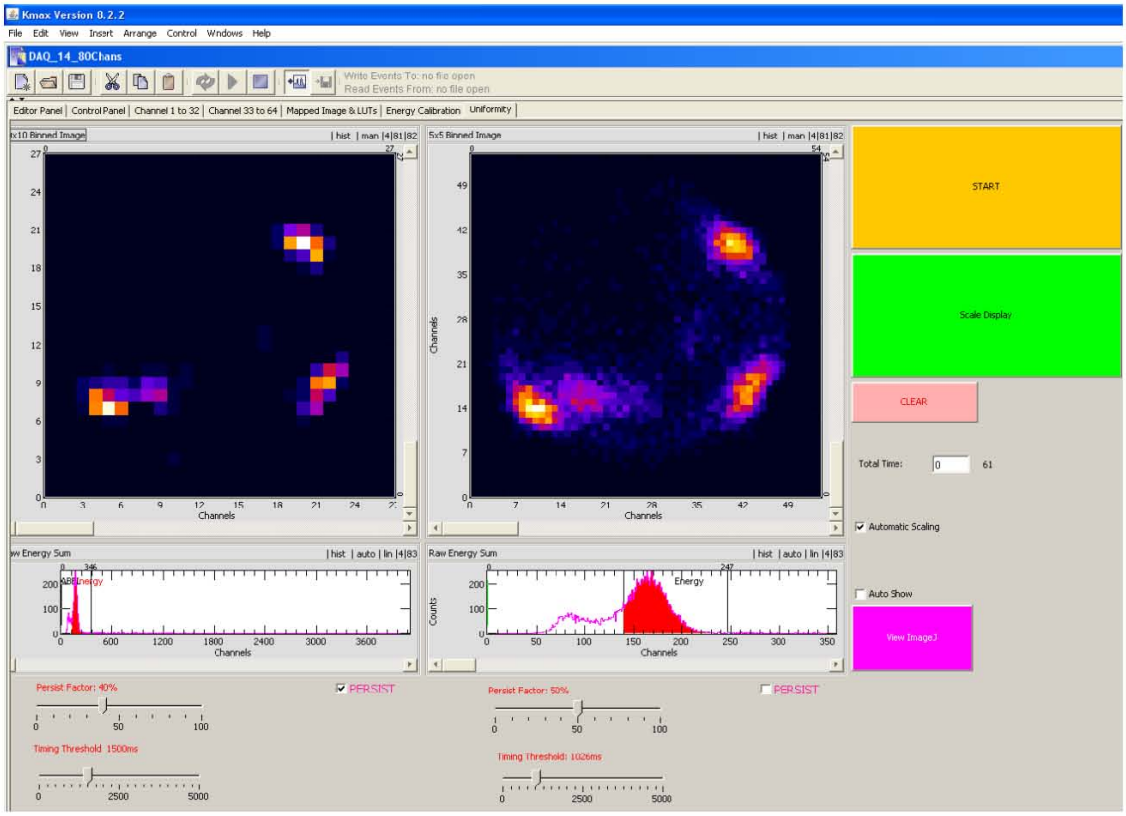

Figure 40: KMax GUI for the gamma camera showing an image of four SLNs inside a patient

The binning and persistence modes were introduced to the gamma GUI early in the clinical SLNB study described in more detail in chapter 5. As mentioned above, the visual display of the raw images was not satisfactory due to sparseness of the data, and a 5x binning mode was used to improve the perceived concentration of the radioactive tracer as demonstrated in Figure 41. Binning is essentially a process of clubbing sparse data together to form denser images. At each pixel location in the binned image, the intensity of a given pixel is replaced by a sum of the intensities in the N x N neighborhood centered on that pixel in the original image. The matrix size of the raw images is 270 x 270 pixels for the FOV of 60 mm, resulting in an effective pixel size of 0.24 mm. With the addition of the binning modes, the images can be displayed and saved

in 5x and 10x modes with image matrix sizes of 54 x 54 and 27 x 27 pixels, and pixel sizes of 1.2 and 2.4 mm respectively. Furthermore, the surgeons requested implementation of a persistence mode in the GUI to give them an option to perform imaging of the patient in more or less a “real-time” mode. The operation in this mode is shown in top left window in Figure 40, and presents to the surgeon only the regions of highest instantaneous concentration of the radiotracer in the patient, with the image refreshing itself depending on the user set parameters in the sliders below the energy histograms. This mode helped improve the usability of the camera tremendously and the logistic and the ease of use of the GUI were scored much more favorably after the implementation of these features (discussed further in chapter 5).

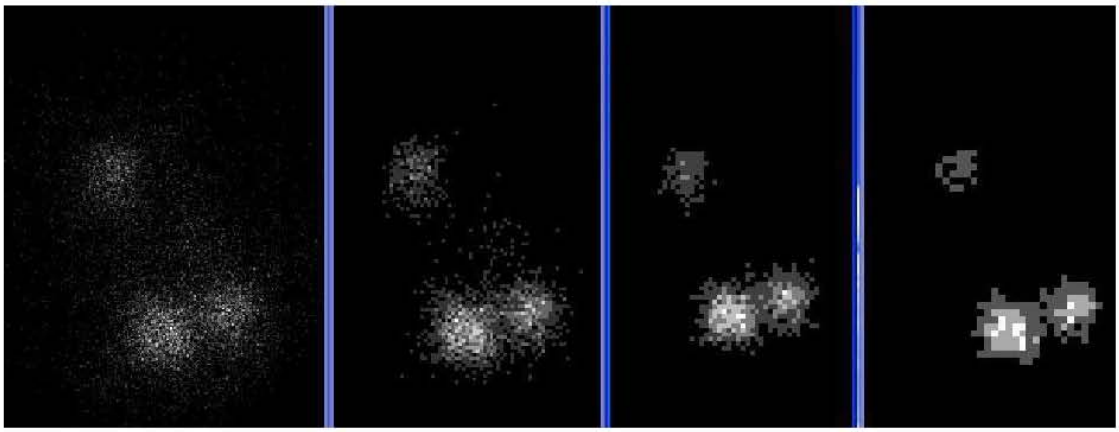

Figure 41: Examples of binning raw acquired images (from left to right 1x, 2x, 3x and 4x) to improve perceived regions of higher uptake of the radioactive tracer

4.2.2 Co-registration concept in IMIS

Co-registration of visible/NIRF and gamma images is a challenging step in the image display process as the cameras are not mechanically connected. The goal of co-

registration is to enable the information from the most recently acquired gamma image to be available during the visible/NIRF imaging to provide guidance to surgeons until the surgical targets are near the surface. The idea is to show the boundary outlines from radioactive targets in the gamma image on top of the visible/NIRF video, giving the surgeon an idea about the location and extent of targets prior to the incision. However, a minor misalignment of the gamma camera can cause large errors in the co-registration; this is due to the fact that the gamma camera can and does image targets at considerable depths in the patient, while the visible/NIRF camera only looks at most at subcutaneous information. This is illustrated in Figure 42, with the gamma camera being directly below the visible/NIRF camera but slightly misaligned in the z direction compared to it; due to this misalignment, the two cameras are not looking at the same FOV and the co-registration errors can occur.

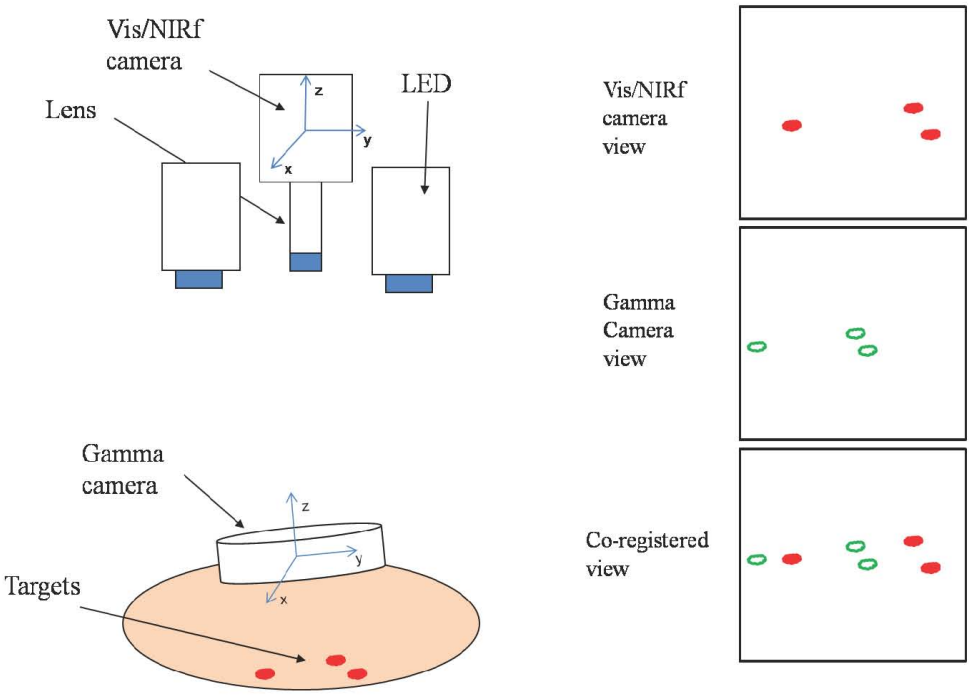

Figure 42: Illustration of the misalignment effect on the co-registration error

There are two major steps in the co-registration process described above. First the alignment of both cameras needs to be appropriate to help minimize the error described above. Then the offsets in resolution, rotation and center of FOV between the images acquired by two modalities have to be corrected. Alignment is achieved by using a set of attitude and heading reference system (AHRS) units positioned on each camera that provide their relative orientation information. In step two, a custom Matlab (Matrix laboratory, Mathworks, Natick, MA) routine is used to segment a boundary of the relevant target location from the gamma image, perform the offset corrections between the images from two modalities and overlay the boundary of the imaged gamma targets appropriately on the visible/NIRF video in real-time.

4.2.3 AHRS unit setup, alignment and co-registration

The AHRS units consist of set of sensors that provide the attitude, heading and yaw information (Euler angles). They have traditionally been used in aircrafts, most importantly replacing older and less reliable gyroscopic equipment. The accelerated development of the AHRS units in recent years makes them readily available for commercial use and they have been increasingly used in robotics and medicine.

Two AHRS VN-100 Rugged units from VectorNav Technologies LLC, Richardson, TX are used for co-registration purposes in IMIS. They employ a quaternion based and drift compensated Kalman filter with high update rates. In bench-top testing, good stability of the AHRS output in extended time studies in a surgery-like situation with presence of magnetic materials and tools was observed. The units are mounted with

custom adapters on the back of the gamma camera and on top of the visible/NIRF camera head (Figure 43 and Figure 44).

Figure 43: AHRS unit mounted on back of the gamma camera

Figure 44: AHRS unit mounted on the visible/NIRF camera head, also showing the delrin radiating bar adapter for the RGB and NIR LEDs

The GUI for the AHRS units is a software package provided by VectorNav called Sensor Explorer. Figure 45 shows program's ability to show the coordinate systems of both AHRS units on the screen at the same time and notify the user when their Euler angles are aligned to within a user defined tolerance value (located above the red "Out of Tolerance" display in the figure below). When the cameras are aligned rotationally, the red display changes to a green "In Tolerance" display and the surgeon can acquire the image with the gamma camera. The gamma camera can then be removed from the surgical FOV after the acquisition. The information from the acquired visible image of the back of the gamma camera (described below) is used to overlay of the gamma image onto the visible/NIRF image until the visible/NIRF camera or the patient are moved.

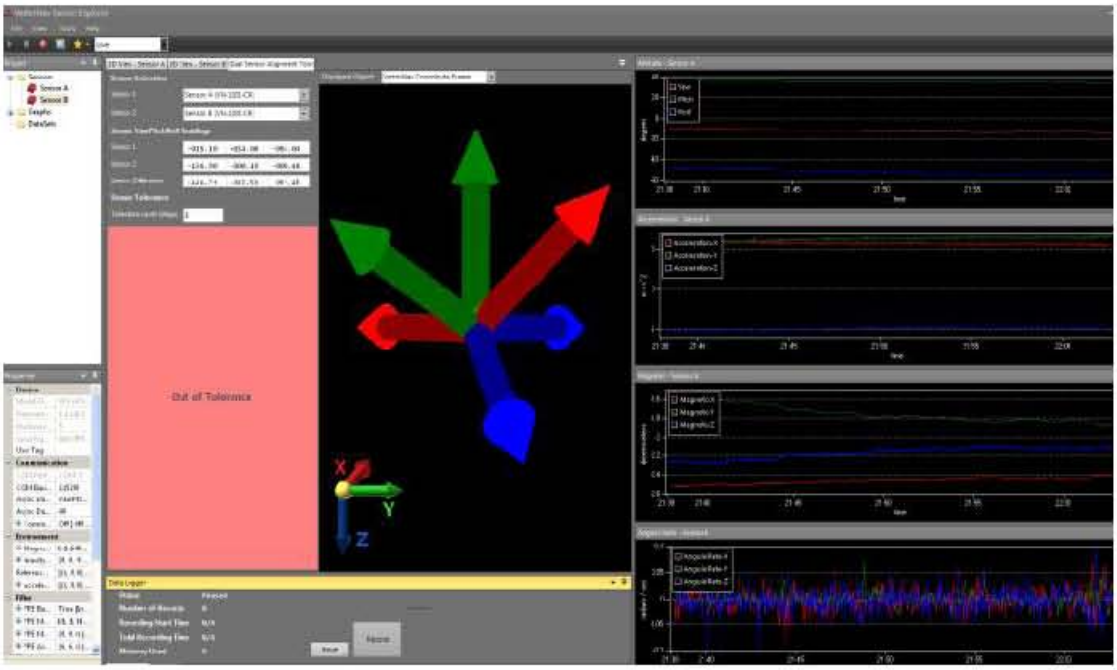

Figure 45: GUI for the Sensor Explorer software, showing the orientation vectors of the AHRS units

The remaining part of the co-registration process is to account for the differences between the centers of the images from two modalities and account for varying working distance of the visible/NIRF modality that changes the magnification of the images in the gamma modality relative to the visible/NIRF modality. Accounting for the WD and magnification is done with the help of the AHRS. The change in the stepping motor position for the lens changes the field of view seen by the visible/NIRF camera, and thus the area imaged by each camera pixel. The magnification factor is directly related to the WD, which in turn can be determined by the area of fine features of the VectorNav logo on the back of the AHRS unit when the image is in focus. While the gamma camera is acquiring the data, the back of the camera and the AHRS unit mounted on it are imaged with the visible camera. The logo on the AHRS unit (Figure 43) is segmented and its area in the image is calculated in pixels. The area in square millimeters is a known value, and this relation is used to calculate the area imaged in each pixel of the visible image. The area imaged by each pixel in the gamma image is a known value and we can compare the areas from gamma camera and the VectorNav logo as imaged by the visible camera to determine the relative magnification factor between the two images. This segmentation algorithm as well as the co-registration GUI and program in Matlab were developed with help of the fellow graduate student Anoosha Papireddy.

The next step in the co-registration process is to align the centers of the images acquired by each modality. The center of the gamma image is always the center of the gamma camera. On the other hand, the position of the center of the gamma image with respect to the visible/NIRF image can be acquired by using a segmentation algorithm to find the center of the gamma camera with respect to the position and orientation of the

AHRS unit logo in the visible image of the back of the gamma camera. The algorithm segmenting the logo feature from the back of the AHRS unit can reproducibly and singularly determine the center of the gamma camera in the visible image. With this information, centering and scaling the image from the gamma camera that can be overlaid appropriately on the visible/NIRF image is performed.

4.2.4 Segmentation of the targets of interest from the gamma image

The final step in co-registration of the images is to segment the target of interest from the gamma image and overlay the resulting outline on the visible/NIRF video in real-time during the surgery. The gamma images are loaded and displayed on the screen post acquisition in Matlab so the surgeon can either choose one or more of the specific high concentration spots in the image that they are interested in, or allow the automatic detection of the radioactive nodes. In this process, the gamma images are acquired and saved in Kmax as a text file which is imported in Matlab and converted to a grayscale image. Then a standard Gaussian filter is used to reduce the noise in the image and the image is binned in preparation for the segmentation step. Various edge detection algorithms exist, which work best on binary images, so the gamma image is converted to binary format. From the existing clinical study data, a 30 % threshold of the maximum intensity in the clinical images overall was found to be the optimal value in this step of the process. All pixels in the original image with intensities above this threshold are converted to a binary 1 (white) and those below are converted to a binary 0 (black) in a new image. Any remaining small holes are filled and small regions of isolated white

pixels are removed to get a clean binary image. Several different types of edge detection algorithms were tested and the Canny method (77) performed best for our task. However, the resulting edges can still be ragged, broken and may have unnecessary spikes from noise caused by low statistics clinical images.

To obtain smooth, closed edges and also to give the surgeon a flexibility of choosing multiple ROIs, active contours (78) are used. An active contour/snake is an energy-minimizing spline guided by external constraint forces and influenced by image forces that pull it toward features such as lines and edges. The active contour needs a point of initialization from where it deforms to encompass the nearby objects of interest. If the surgeon decides to select particular ROIs, he/she can click in the center of each target and a snake is initialized at each of those points. If the surgeon wants to select all the hot nodes without interaction with the GUI, the centroids of the nodes from the original Canny edge image are calculated and used as the initialization points for the active contours. Finally, an image containing the boundaries of the nodes is saved, and these contours can then be superimposed over the visible/NIRF image after all corrections are made.

For review of the co-registration process described in this section, a detailed walk-through summarizing the steps of the co-registration process is shown below; a flowchart summarizing the whole process is also shown in Figure 46.

A gelatin phantom was constructed to mimic the optical properties of human tissue in the NIR region. Two acrylic lesions filled with ^{99m}Tc-pertechnetate and ICG were placed in the phantom. In step one of this walk-through, the gamma camera is positioned above the phantom and the gamma image is acquired (right).

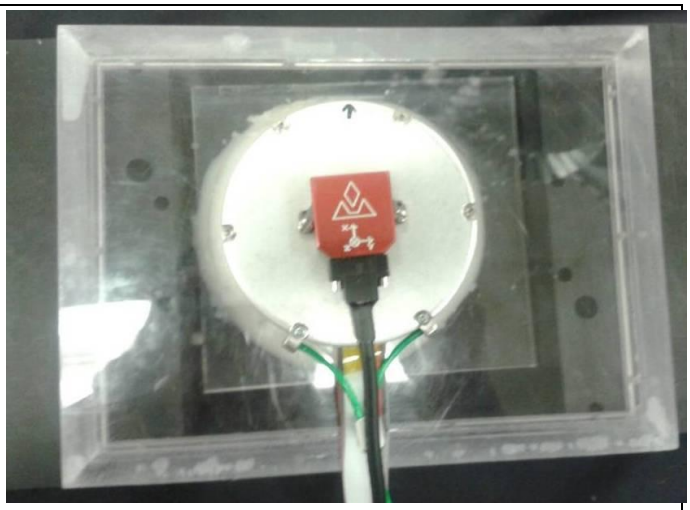

During the acquisition of the gamma image, rotational alignment of both modalities is achieved. The visible NIRF system is positioned over the gamma camera (left) until the AHRS systems are aligned in VectorNav software (bottom).

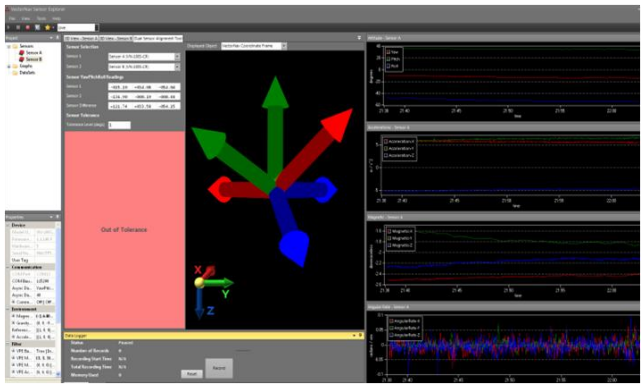

The back of the gamma camera and the AHRS unit is then imaged by the visible/NIRF system (right).	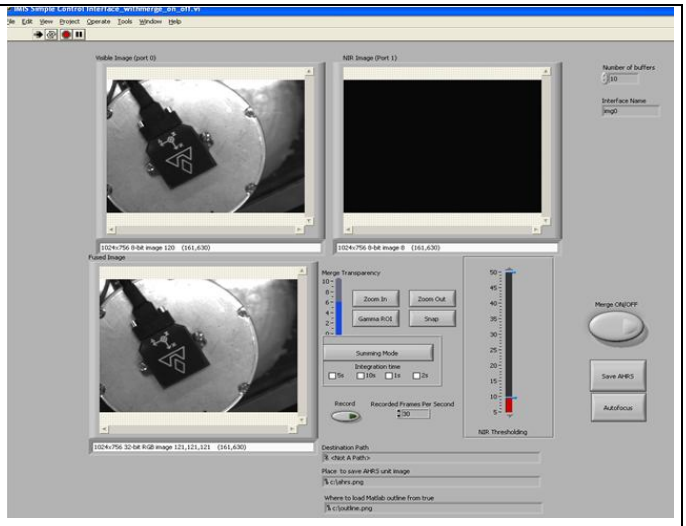
This image is segmented in Matlab and the parameters are acquired to determine the scaling factor and the translational shift between the gamma and the visible/NIRF images.	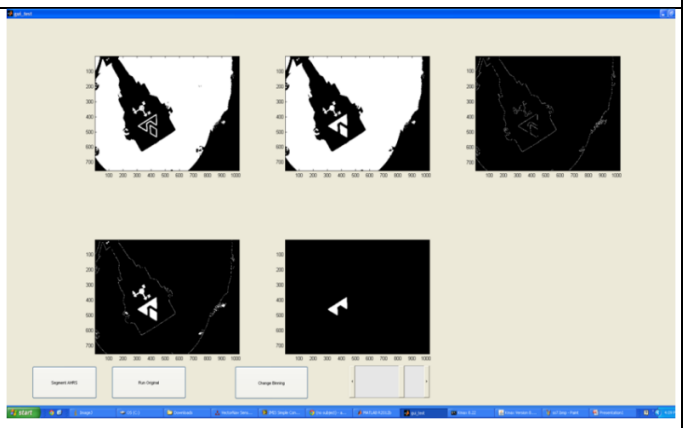
The gamma camera image is segmented and the scaling factor, rotation and translational shift corrections are applied to the gamma image. The final outline from the gamma image is saved. The gamma camera is removed from the imaging position and the phantom is imaged with the visible/NIRF modality.	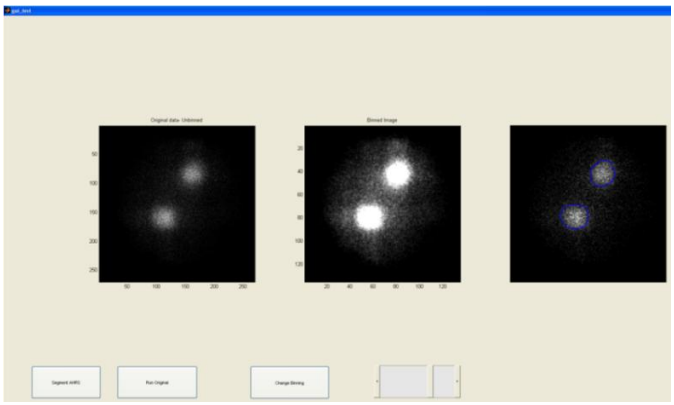

The final outline from the gamma image is overlaid on top of the visible/NIRF image. In this setup, the lesions are located deep inside the phantom, and the NIRF signal from the lesions cannot penetrate through the tissue; the surgeon uses the gamma outline to determine where the lesions are to guide the initial incision.	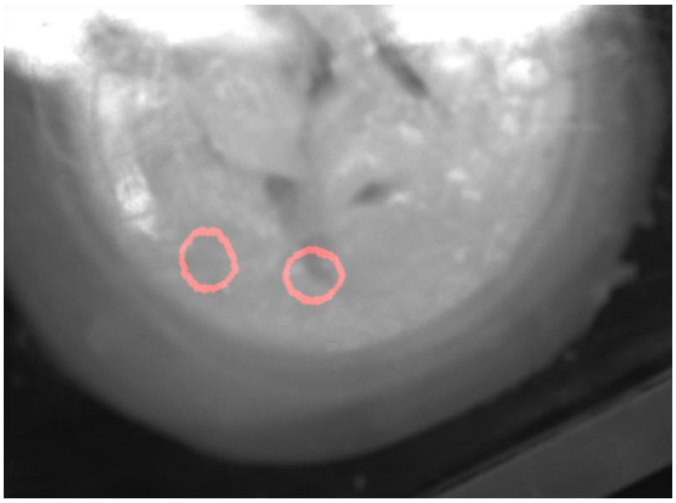
The surgeon pursues the incision of the phantom until the lesions are closer to the surface and the NIR fluorescence can be used to precisely locate the lesions in high resolution and real-time and remove them from the phantom/patient. The surgeon can use the visible/NIRF modality to assess positive margins and make sure that the lesions are fully removed to minimize the possibility of cancer reoccurrence.	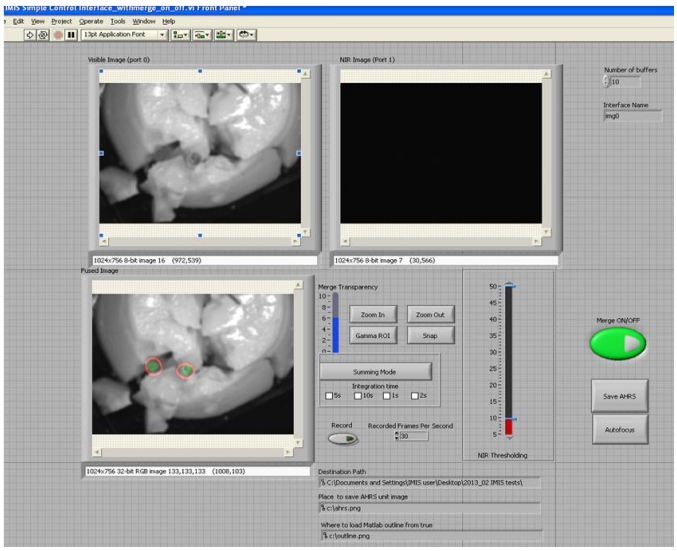

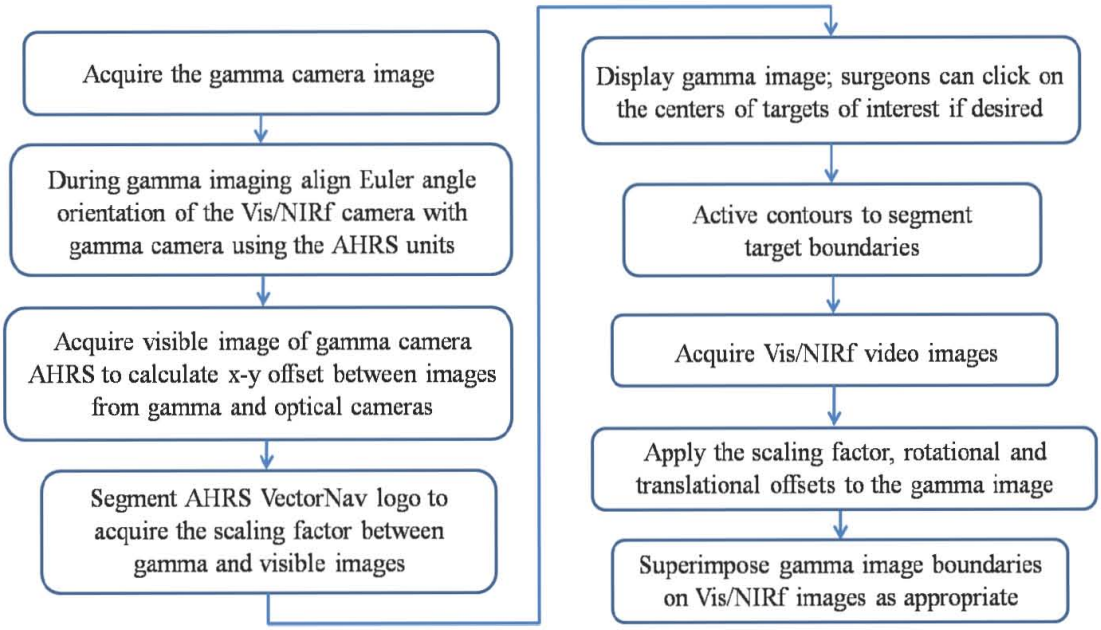

Figure 46: Co-registration process flowchart

CHAPTER 5: GAMMA SYSTEM CHARACTERIZATION AND RESULTS

A fundamental part of developing an imaging system involves characterizing its performance, especially in the task for which the system was developed for, as well as comparing those results with the theoretical predictions. In this section, the design and results of bench-top experiments with the gamma modality will be discussed, including the completed clinical SLNB study setup and results.

5.1 Gamma system characterization in bench-top testing

In this section the results of characterization tests of the gamma system are described, both in basic bench-top setups, as well as in more task specific situations that would mimic the intraoperative surgery setup.

5.1.1 Spatial resolution

Spatial resolution refers to the level of detail that can be resolved by the imaging system, and is usually simply envisioned by how closely two lines can be resolved in the acquired image (the shorter this distance, the higher the resolution). As this can be viewed as an arbitrary measurement visually, and can be manipulated by window

leveling of the image, the most common way to calculate the spatial resolution is by measuring the full width at half maximum (FWHM) of a sufficiently thin line source (79). Two different spatial resolution measurements are important and have become a standard practice in similar setups (80). They include measuring the intrinsic resolution of the camera (without the collimators attached to the detector), and measuring the extrinsic resolution (with one or two collimators attached to the detector) with increasing distance from collimator.

The intrinsic spatial resolution of the gamma camera was measured using a ^{99m}Tc-pertechnetate point-like source positioned greater than five times the useful field of view (UFOV) from the detector with the collimator removed and with a 0.3 mm wide tungsten slit placed 3 mm from the scintillator. The UFOV here is defined as a circular area with a diameter that is the largest inscribed circle within the collimated field of view (79). A program in Interactive Data Language (IDL, Exelis Visual Information Solutions, Inc, Boulder, CO) is used to manipulate the image in such a way to extract the perpendicular profiles from across the length of the slit and add them together while aligning their peak positions to form a line spread function (LSF) of the original image. A Gaussian is then fit to the LSF and has the following form:

$$f(x) = a + be^{\frac{-(x-c)^2}{2d^2}} \qquad \text{equation 5}$$

with $b = \frac{1}{\sigma\sqrt{2\pi}}$, $c = \mu$ (expected value), $d = \sigma$ (variance) and a to account for a possible zero offset. The FWHM can then be found to be $2\sqrt{2\ln 2}\, d$. The intrinsic resolution of the system is measured to be 4.2 mm by this method. This is a combination of the achievable

limits of the detector and the electronics. The resolution might be in theory improved with either a finer sampling of the SiPMs or a thinner crystal that could lower the amount of scattered light within the crystal before it reaches the SiPMs (41).

The second experiment characterizes the resolution degradation of the gamma camera with the increasing distance from the collimator. One of the reasons that this experiment is necessary is due to the fact that the camera will be used in clinical studies where the radioactive targets will be inside the patient, at some depth away from the camera. The extrinsic resolution of the camera was characterized by translating a small capillary (Kimble 71900-50 µL, 1 mm inner diameter) filled with the ^{99m}Tc-pertechnetate solution away from the collimator and obtaining images at discrete distances from the collimator. Two separate experiments are performed in succession, with one and two collimator options on the camera. The resulting data is compared to the theoretical curves, with the theoretical extrinsic resolution being a quadrature sum of the collimator resolution and the measured intrinsic resolution of the detector. The spatial resolution results for the one and two collimator option can be seen in Table 2 and Figure 47 below.

Distance from the collimator [mm]	Theoretical resolution [mm]	Measured resolution [mm]	Theoretical resolution [mm]	Measured resolution [mm]
	1 collimator option		2 collimator option	
0	4.2	4.8	4.2	4.3
10.1	4.6	5.4	4.4	4.5
20.3	5.2	6.4	4.5	4.9

30.5	6.1	7.5	4.8	5.4
40.6	7.1	8.9	5.1	5.9
50.8	8.2	10.4	5.5	6.5
60.9	9.3	11.6	5.9	7.1
71.1	10.5	13.0	6.3	7.7
81.3	11.7	14.2	6.7	8.4
91.4	12.9	15.5	7.2	8.9
101.2	14.1	16.6	7.7	9.6

Table 2: Theoretical and measured gamma camera spatial resolution for varying source-to-collimator separation

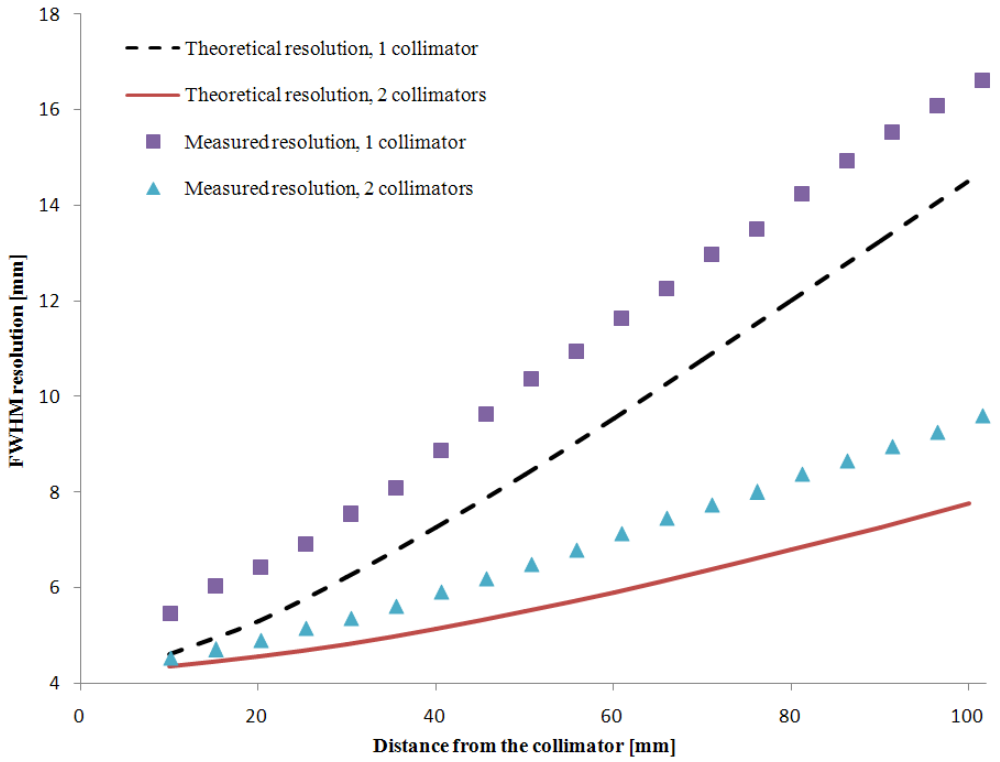

Figure 47: Gamma camera spatial resolution theory and experimentally measured values

5.1.2 Energy resolution

The energy resolution is a measure of how well the detector can resolve signals coming from two sources that have different energies. There are intrinsic hardware reasons that a signal coming from a radioactive ^{99m}Tc-pertechnetate source is not always resolved as being exactly at 140 keV. These include, but are not limited to, statistical fluctuations in the amount of scintillation light per keV of energy deposited in the crystal, statistical variations in light detection of the SiPMs and the noise sources near the SiPMs (optical coupling variations, possible temperature gradients). The most common figure used to express the energy resolution of a detector is the FWHM of the energy spectrum acquired when the detector is irradiated by a source of mono-energetic gammas. The resolution figure is usually calculated in relative terms with reference to the peak energy of the spectra and reported in percents (%). The smaller this number is, the better the detector is at resolving different energies that are hitting the crystal. The camera energy resolution was characterized using a solution of ^{99m}Tc-pertechnetate (activity of 3.7 MBq) in a petri dish placed on top of the collimator to produce a uniform low-scatter flood source. The petri dish had a diameter of 75 mm and extended across the entire face of the gamma camera, making it about 15 mm larger in diameter than the collimated part of the detector. A high statistics flood image was acquired with user defined regions of interest (ROIs) in different parts of the image, for purposes of examining the energy resolution over different parts of the FOV of the detector (Figure 48).

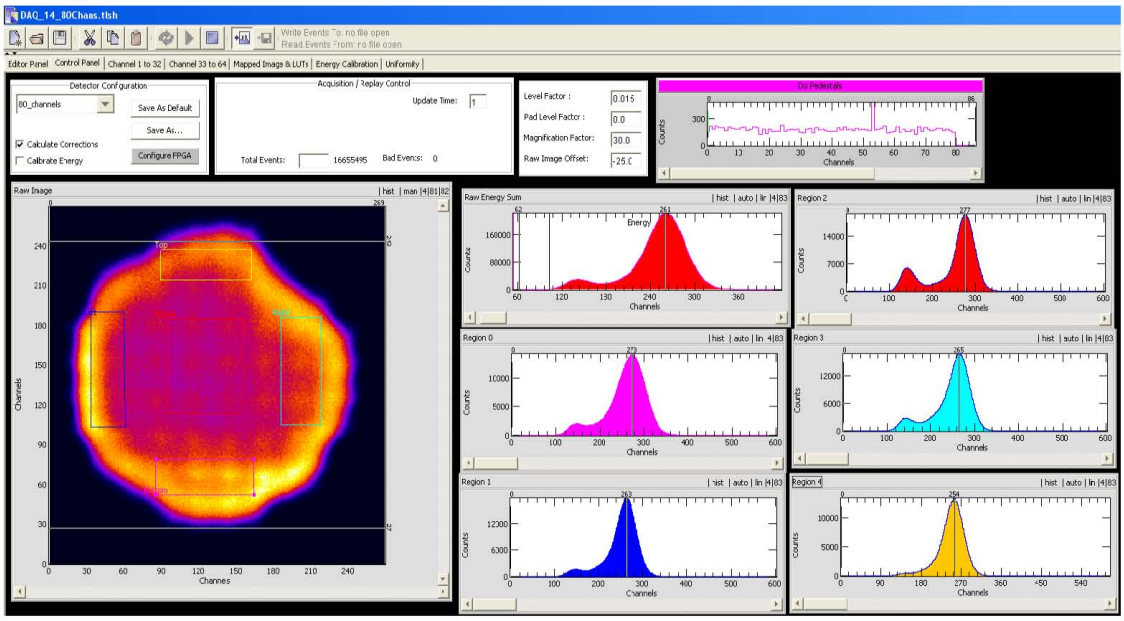

Figure 48: Flood image with several user defined ROIs (left) and their respective energy spectra (right). The full FOV energy spectra is shown in the "Raw Energy Sum" histogram and Region 0 to 4 histograms correspond to the bottom, left, middle, right and top ROI energy spectra respectively

The locations of the energy peaks of the different ROIs in figure above are not lined up at the same channel number in present setup. This is due to the hardware setup discussed in chapter 2 with eighty different MPPC units being powered in groups of 16 by 5 power supplies. The different gain properties of each MPPC result in different energy peak channel positions for each MPPC and therefore, for each summed group of 16 units. To account for the varying gain properties of the SiPMs in different regions, energy normalization is performed to the energy spectra. In this process, the energy spectrum for each pixel in the 5x binned image is recorded from the high statistics flood image. A look up table is then formed with energy spectrum peak position for each pixel in the 5x binned image. The normalization of the energy spectrum is performed by scaling the positions of all energy spectra to a fixed value, which minimizes the spread in

the final energy spectrum. The FWHM energy resolution for the entire FOV prior to energy normalization was found to be 24.3 %, with the measured FWHM of the energy spectra in the custom defined ROIs calculated at 28.8 % (bottom ROI), 22 % (left ROI), 19.1 % (middle ROI), 21.3 % (top ROI) and 23.5 % (right ROI). Energy normalization improved the energy FWHM resolution for the entire FOV to 21.1 %. The improved value shows that the energy resolution improvements could be made if each MPPC unit could be finely tuned to adjust the gains accordingly; however this would be unrealistic to translate in practice due to high cost. In conclusion, we see that the energy resolution across the ROIs is consistent with the overall detector energy resolution, and these values can be compared to the similar size single crystal detectors being developed (81; 82).

One of the practical reasons that the energy resolution is important is because of the gamma camera's use in clinical studies described later in this chapter. When imaging human patients that have a considerable amount of tissue between the surgical target and the camera, we have to consider the effects that the scattered gamma rays have on the energy spectrum. If a patient is injected with a ^{99m}Tc based tracer and a gamma is emitted from a source deep within the patient's body, the gammas can interact with the tissue between the camera and the source multiple times before being recorded by the camera. Even after one or two scattering events, a gamma can change its direction only slightly and hit the detector with a lower energy than 140 keV, contributing false information to the lower end of the energy spectrum. These scattering events can also have large scattering angles, and a scattered gamma that does not correspond to the true location of the radioactive target could be potentially recorded by the detector in a wrong location. The result of the two scenarios combined would be a blurred image with higher random

detected events and even possibly false hot spots, which further illustrates the need for a good energy resolution by the detector. Use of a tight energy window around the true photopeak would minimize the amount of scattered events accepted, albeit not necessarily fully eliminating them.

5.1.3 Spatial linearity, uniformity and sensitivity

One of the most common and basic problems that arises in detectors is the image nonlinearity, where distortions in the image can cause a straight line to appear curved in the image. These distortions happen when the x and y position signals do not change linearly with the changing position of the radiation source across the detector. A clear outward bowing of the line sources in the raw image is observable in the images acquired with the gamma camera described in this dissertation, which is also called a barrel distortion. A custom made aluminum phantom was constructed to hold two perpendicular layers of parallel and regularly spaced capillaries (Kimble 71900-50 µL) with inner diameter 1 mm, filled with a ^{99m}Tc-pertechnetate solution (Figure 49). In both layers, the capillary pitch was 10 mm. This setup was used to characterize the geometric nonlinearities within the image.

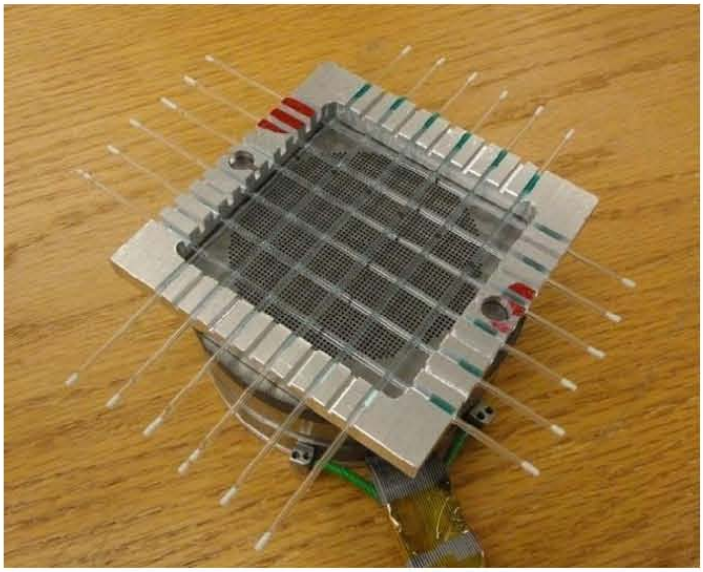

Figure 49: Custom phantom holding two layers of capillaries filled with ^{99m}Tc-pertechnetate

The acquired image is shown on the left of the Figure 50. The observed nonlinearities can be corrected in the software using a higher order polynomial fit correction. The nonlinearities are important to track over time as they can indicate issues with the optical grease coupling or other problems with the system electronics. To improve the image geometric linearity, the acquired raw capillary phantom image was loaded in Matlab and all grid intersections were selected. These intersections were compared to target grid intersection points for an ideal grid model using the cp2tform image processing toolbox. Two third degree 2D polynomial equations of the form:

$$\text{new\_x\_position} = a_0 + a_1y + a_2x + a_3y^2 + a_4x^2 + a_5xy + a_6x^2y + a_7xy^2 + a_8x^3 + a_9y^3$$

and

$$\text{new\_y\_position} = b_0 + b_1y + b_2x + b_3y^2 + b_4x^2 + b_5xy + b_6x^2y + b_7xy^2 + b_8x^3 + b_9y^3$$

were used to fit the original data to the ideal grid with the least-square fitting. To improve the linearity counts, each pixel in every original uncorrected image is transformed according to the above equations to shift their positions accordingly. The de-warping equations were implemented in the Kmax GUI for image correction during gamma camera image acquisition in real-time. As an example, a raw and a corrected image of the 2-layer capillary phantom are shown in Figure 50.

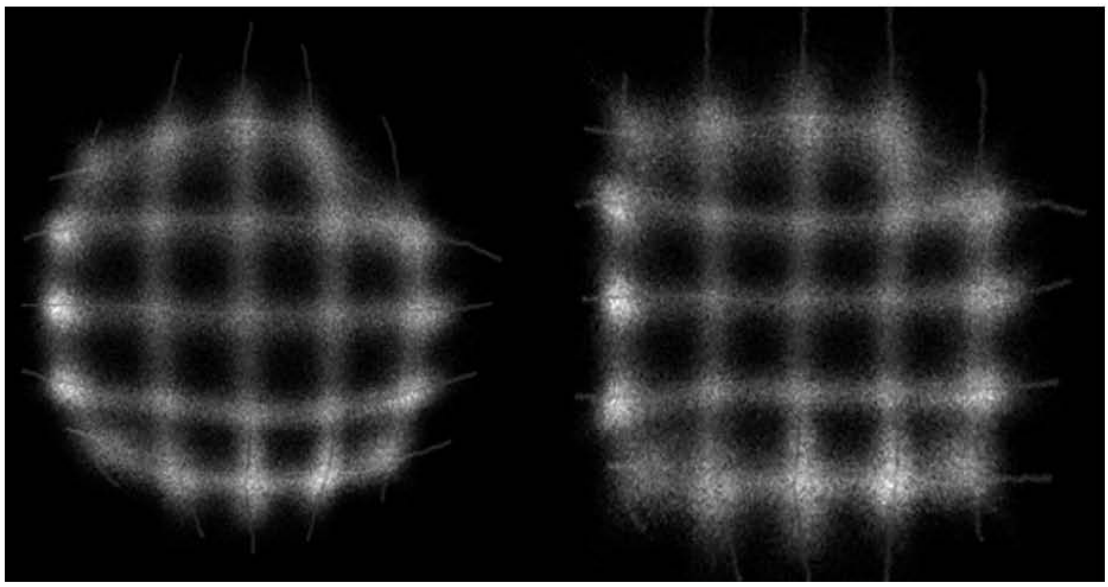

Figure 50: Barrel distortion example in the raw gamma camera image of a grid pattern (left) and a corrected grid pattern image (right) showing the improved linearity across the field of view

At the moment, this option is available to the surgeons to take advantage of in the upcoming clinical trials, but the real value of the linearity corrections will become obvious in a future project where the acquired gamma images are planned to be used as a

basis for reconstructing a real-time 3D model for image-guidance to radioactive targets in patient's body intraoperatively.

Furthermore, the spatial nonuniformities are also noticeable in the raw image in Figure 48 and can be a result of non-ideal components and design of the detector. The term uniformity here is being used to refer to the intensity variations within the image that is acquired using a uniform and low scatter radioactive source. The most important of the causes of nonuniformities in the system described in this dissertation are the non-uniform detection efficiencies of the separate SiPMs (a characteristic pincushion distortion in front of the individual SiPMs) as well as the effects causing a very prominent higher intensity ring shaped intensity profile in the raw image (see the raw image on the left of Figure 51). The latter effect is caused partially by the barrel effect nonlinearity and partially by the internal reflections of scintillation light from the sides of the detector crystal and housing back towards the SiPMs in the edge region. Furthermore, if an event occurs in the center of the crystal, there are SiPMs on either side of the event location, allowing the COG algorithm to recognize the true location easily. However, for the events that occur at the edge of the crystal, there are physically SiPMs on only one side of the event location, so the distribution of events is not uniform and the COG algorithm "pulls" those events towards the center of the crystal, further adding to the ring artifact. The non-uniformities described above can be partially corrected by applying standard high statistics flood normalization to the raw images. A ^{99m}Tc-pertechnetate solution in a petri dish (activity of 3.7 MBq) was placed on top of the collimator to produce a uniform low-scatter source first. A high statistics flood image ($Flood_{hs}$) was acquired in this fashion and used as a flat-field correction map to correct the subsequent

images on a pixel to pixel basis according to the formula: Corrected Image = (Uncorrected Image * Average ($Flood_{hs}$)) / $Flood_{hs}$. An example of a successful flood correction is shown in Figure 51. The validity of use of this method is discussed in more detail elsewhere (41).

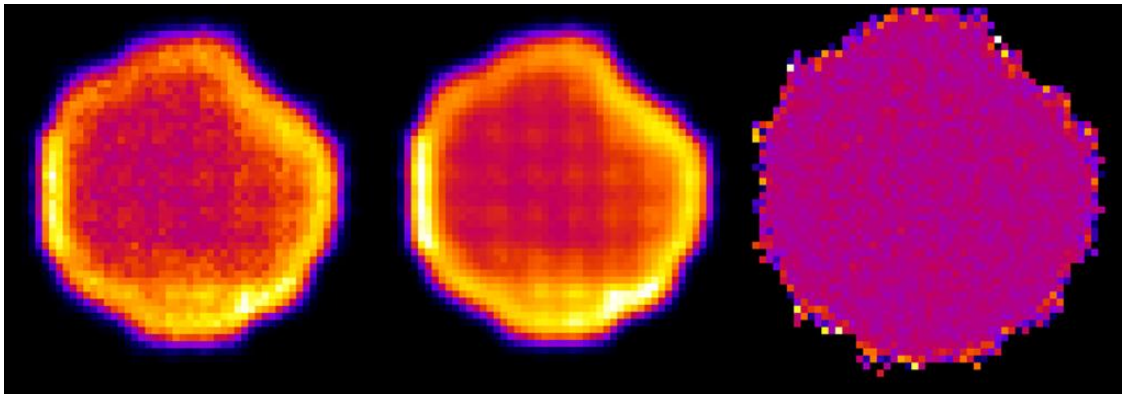

Figure 51: Image of a low statistics raw flood image (left) the high statistics raw flood image that was used for the correction (middle), and the resulting flood corrected low statistics image (right)

The uniformity of the corrected image on the right of this figure was judged by measuring and calculating the integral uniformity in the useful and central fields of view (UFOV and CFOV). The central field of view is defined as a circular area with a diameter that is 75 percent of the diameter of the UFOV. To measure the uniformity of the corrected image, integral uniformity is measured in the useful and central field of views (UFOV and CFOV) that contain respectively 95% and 75% of the image FOV. The integral uniformity is defined as:

$$\text{Integral uniformity} = \frac{Pixel_{max}\text{-}Pixel_{min}}{Pixel_{max}+Pixel_{min}} * 100 \qquad \text{equation 6}$$

The symmetry of the entire FOV is compromised by a dead SiPM in the top right corner, which would affect the integral uniformity for the UFOV if the full camera FOV was used as reference in equation 6. Consequently, the UFOV was adjusted to be a circular area in the center of the image with a diameter that is the largest inscribed circle within the collimated field of view not containing the missing SiPM. The CFOV was adjusted accordingly relative to the UFOV. After adjusting the FOV, the integral uniformity was measured to be 15 % and 26 % for the CFOV and UFOV respectively.

The sensitivity of the gamma camera is a measure of the efficiency with which the camera detects the incoming gamma radiation. Besides the design and build of the camera, it is also dependent on which collimator is used with the gamma camera. The system sensitivity, defined as the number of detected counts per second per kBq of source activity, was experimentally measured and also calculated for a ^{57}Co point source in air (activity of 0.17 MBq) placed above the collimator at the center of the FOV of the gamma camera. This measurement was performed for both one and two collimator options. The total number of counts in the image of the point source was measured in ImageJ and used to calculate the sensitivity in counts/min/μCi. The final results for the one collimator versus two collimators option are respectively 324 and 65.7 cps/MBq, which show efficiency ratio of 4.9 between the one and two collimator options and agree well with ratio of 5.0 expected by collimator theory.

The gamma camera sensitivity was also experimentally measured and calculated following the NEMA standard (83). A flat-bottom plastic dish with 26 mm ID was placed above the collimator at a distance of 100 mm from the gamma camera and with the dish positioned at the center of the FOV of the gamma camera. An image was acquired with

half million counts. This measurement was performed for both one and two collimator options. The sensitivity at the WD of 100 mm was then calculated as ratio of the total number of counts in the image as measured in ImageJ and the total activity in the plastic dish. The measured sensitivities using the one- and two-layer collimators are 481 and 73 cps/MBq, respectively. This efficiency ratio of 6.6 between one and two layer options compares well with the theoretical ratio of collimator geometric efficiencies of 5.0.

5.1.4 Photopeak channel position versus temperature dependence

One of the downsides of the SiPM technology is the variation of the MPPC gain with changing temperature and its negative effects on the photopeak channel number position and the count rate (21). The temperature effects on the photopeak position for the camera described here were first noticed during the MEL54 clinical SLNB study, which indicated a need for addition of power supplies for the camera with integrated temperature gain compensation. A sample of the data illustrating this behavior that was acquired during the clinical study is shown in Figure 52 below, with a clear decreasing trend of the photopeak position as the camera heats up from use over time. The change in temperature inside the camera during the SLNB study can be caused by various external sources, from heating from the overhead lighting and the fact the camera is prone to being heated in a plastic sterile sleeve, to leaving the camera near the patient's body and the heating pads used to promote the circulation in patient's extremities. This type of behavior was also observed during the regular gamma camera use in bench-top experiments (Figure 53). This drift of the energy spectra could be tolerated in qualitative

studies, but not in future quantitative and human clinical trials. This issue resulted in addition of the temperature compensating circuit and two Hamamatsu power supplies to the system.

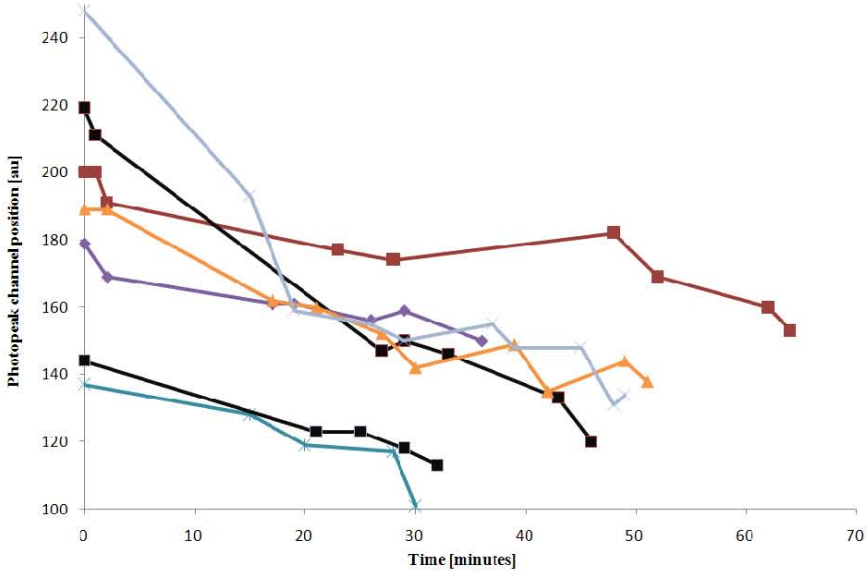

Figure 52: Photopeak channel position versus time (data from the clinical study)

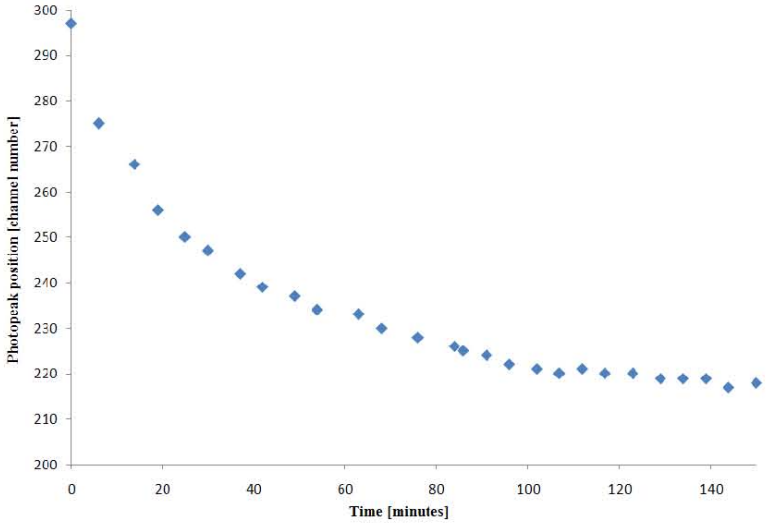

Figure 53: Photopeak channel position drift during normal bench-top camera use

5.1.5 Count rate performance

The effects of the spatial and temporal pile-up of counts in any imaging system degrade the total number of counts detected by the camera. These effects get worse as the count rate increases, and the observed count rate can be compared with respect to the expected count rate to assure that the camera is not operated with significant count losses.

Count rates were observed under intrinsic flood-field conditions with a ^{57}Co point source (activity of 0.17 MBq) that was initially placed one meter away from the camera without the collimators on and slowly brought closer to the camera. The expected count rate was calculated using the solid angle subtended by the gamma camera at the point source with respect to the position of the point source. Plot of the observed count rate against the expected count rate is shown in Figure 54. The dashed line indicates the ideal response (no count loss). Characteristic peak and drop-off in the observed count rate was not reached with this source, showing that the maximum count rate lies above 30 kcps. A 20 % loss count rate occurs at the input count rate of 2.7 kcps (observed count rate 2.15 kcps), indicating that any characterization measurements should be performed well below this count rate threshold.

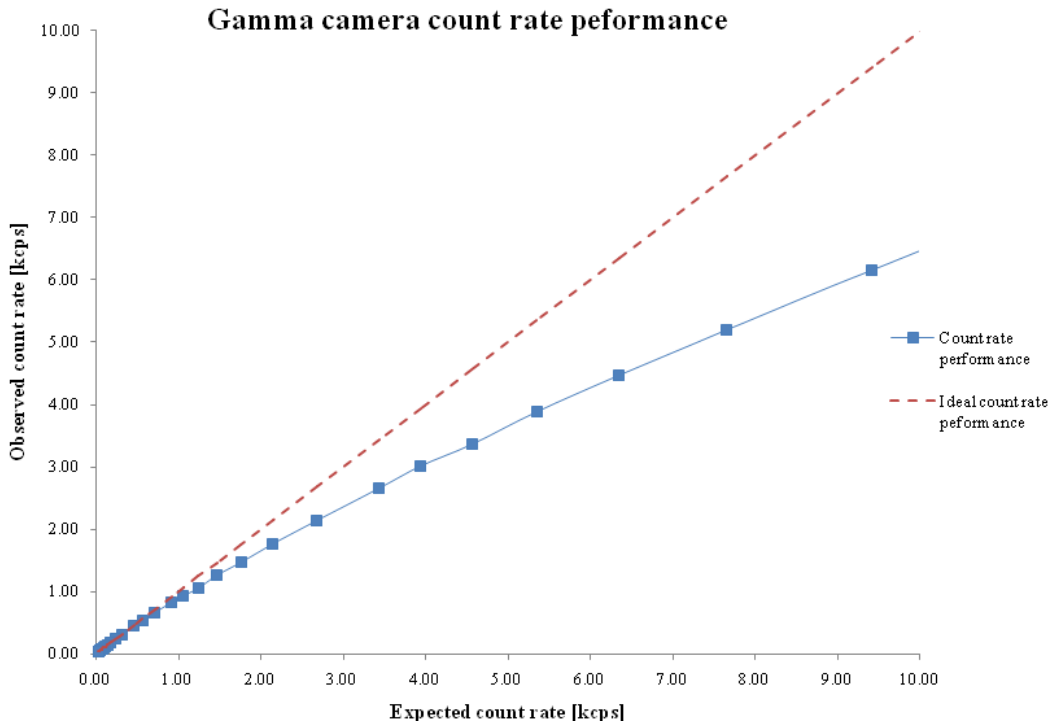

Figure 54: Observed count rate against the expected count rate of the gamma camera

5.1.6 Initial characterization of the profile response function

This gamma camera is slated to be used in a hand-held SPECT project in collaboration with Dilon Diagnostics (Newport News, VA) and SurgicEye (Munich, Germany). The freehandSPECT concept from SurgicEye provides a surgeon with intraoperative 3-D reconstructed data of radioactivity distribution based on hand-held gamma probe detectors. The acquisition and reconstruction of this data takes several minutes but it provides surgeon with important localization and guidance information in the OR with respect to patients' simulated anatomical information. Using a gamma camera instead of the non-imaging gamma probe is a second generation concept of the freehandSPECT product, and would radically improve on resolution of the reconstructed

volume as well as lower the time needed for acquisition of the data, thus improving the logistics and the chances that the product will be used extensively in the OR.

To help address the transfer of data from the gamma camera to the proprietary SurgicEye reconstruction algorithm and gauge the accepted linearity and sensitivity uniformity of the acquired images, a response function of the gamma camera was produced for a point source moving in a straight horizontal line across the FOV in discrete steps. A ^{57}Co point-like source (3.5 mm diameter, activity of 7.4 GBq) was collimated with a ~ 1 mm hole lead mask and moved across the FOV of the gamma camera in discrete steps of 2.5 mm. Thirty one images were acquired, one for every step with a twenty minutes acquisition time for each image. Each of the 5x binned images was inverted to produce a set of virtual images of the source as seen by each of the pixels along the scan dimension. For each pixel, these virtual images were summed and the peak location, FWHM and total counts in the distribution for each of the pixels were measured. The response function pixel peak position and the total number of counts for each pixel are plotted in Figure 55. Note that there is about a 40 mm region in the middle of the gamma camera FOV that demonstrates a very linear response in the pixel peak location change. This region also shows a uniform total number of counts per pixel for each pixel location, or good detection sensitivity uniformity. This initial characterization shows that a single response function could be used to describe the behavior of the pixels in this central region.

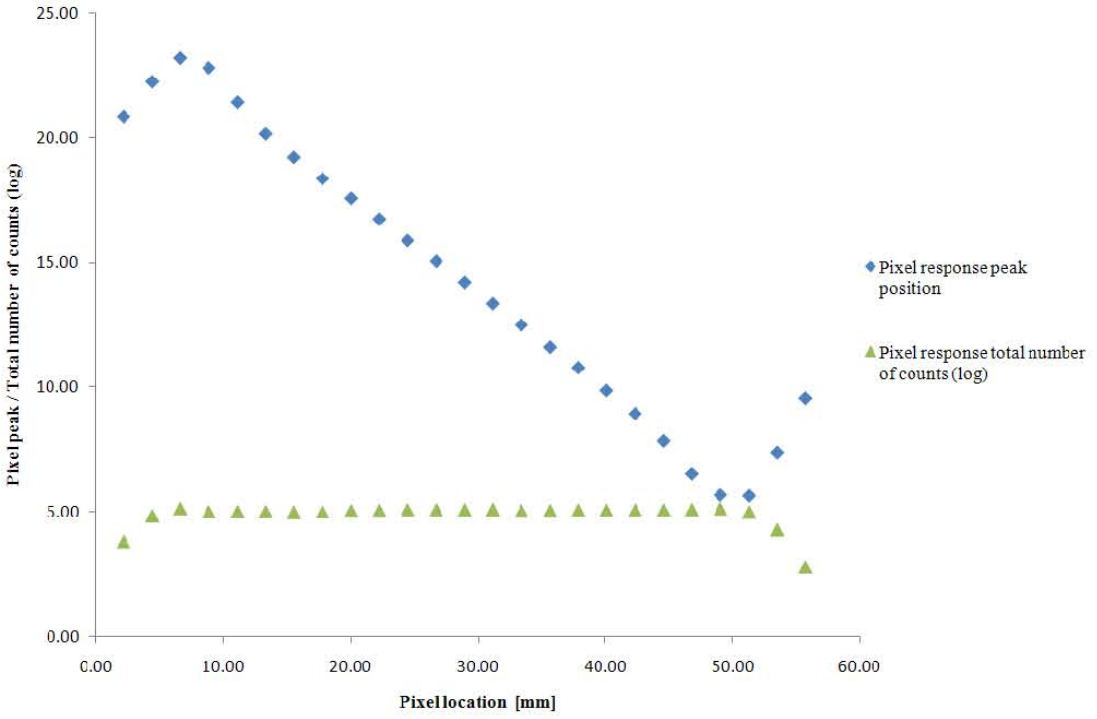

Figure 55: Characterization of the horizontal profile response function of the gamma camera (84)

5.2 Human studies at UVa using mobile gamma cameras

Mobile gamma devices have been studied in various settings, such as in the localization of parathyroid adenomas, lymph nodes in urologic malignancies, and other cutaneous malignancies (85; 86). There have been a number of investigations of small size gamma imagers in surgical procedures with small FOV imagers being increasingly utilized in SLNB (87; 88; 89; 90; 91; 42; 92; 93; 94) and recently in radio-guided occult lesion localization (ROLL) (95). A 'freehand SPECT' system that generated 3-dimensional maps of radiotracer distribution using a hand-rastered non-imaging probe has recently become commercially available as described in the previous section (96). The image information can be anticipated to be useful in more complex situations such as

multiple closely spaced SLNs (e.g. head and neck surgery) or combined SLNB and ROLL. Although the results of these studies suggest that intraoperative MGC imaging is feasible and decreases the length of the surgical procedure, MGCs have not yet been incorporated into the routine clinical care in the US. There is increasing evidence (89) that the MGCs can not only provide complementary information to that of the non-imaging gamma probe but could possibly become a substitute for it. With this in mind, a clinical study was proposed in collaboration with melanoma surgeons at University of Virginia with a goal of testing the gamma camera performance in task specific imaging cases as well as helping pioneer the use of hand-held devices for intraoperative surgical guidance as part of standard clinical care.

5.2.1 MEL54 setup

As described in chapter 1, the SLNB is the standard method for staging cutaneous melanoma and involves identifying the first node(s) draining a tumor by detecting an intradermally injected radioactive colloid tracer. Preoperative lymphoscintigraphy is usually obtained to identify the draining lymph node basins but requires coordinating schedules between the nuclear medicine department and the operating room. A pilot study at the University of Virginia utilized a MGC in conjunction with the conventional lymphoscintigraphy for intraoperative sentinel node localization and provided clinical benefit in 25 % of patients (42). In that study, the sentinel node(s) were identified intraoperatively with a hand-held non-imaging gamma probe and a 13 x 13 cm^2 FOV mobile gamma camera.

Following this experience and in collaboration with surgeons at the University of Virginia, the MGC described in this dissertation was used in a SLNB clinical study for melanoma patients to evaluate its performance compared to the non-imaging gamma probe. The main objectives in this study relevant to the mobile gamma camera imaging were to estimate the benefits of the increased mobility and positioning capabilities of the mobile gamma camera compared to conventional, large FOV gamma cameras. The added value of the hand-held gamma camera was also evaluated compared to the non-imaging gamma probe and to the SLNB procedure in general.

In terms of logistics, the patients in this study received standard lymphoscintigraphy in the nuclear medicine suite. The hand-held gamma probe and the mobile gamma camera were used to evaluate the patient immediately before the surgery at the outpatient center, to complement the information from the lymphoscintigraphy and the preoperative MGC imaging and help the final determination of true “hot” spots prior to the surgery. During the surgery, the participants were re-evaluated intraoperatively with the gamma camera (Figure 56 and Figure 57) and the hand-held probe after removal of each sentinel node and after completion of the sentinel node biopsy procedure. The individual sentinel nodes were imaged ex-vivo with the mobile gamma camera (Figure 58) and counted with the hand-held probe. In each of these assessments, the number, size and location of sentinel nodes were recorded and the correspondence with preoperative hot spots was determined by the conventional clinical gamma detection devices (lymphoscintigraphy and hand-held probe). The time required for imaging was recorded, as well as any notes on the use, advantages, and limitations of the MGC imaging system. During the course of the study, improvements to the gamma camera system were made

incrementally with the goal to have a more optimized system in all possible technical and logistical aspects during the MEL54 study and for the next clinical trial.

Figure 56: Photo of a patient being evaluated intraoperatively with a hand-held gamma camera

Figure 57: Close-up of a patient being imaged with the gamma camera

Figure 58: Photo of a node imaged ex-vivo with the gamma camera

5.2.2 MEL54 results

From April 2011 to February 2012, 20 patients underwent ^{99m}Tc sulfur-colloid lymphoscintigraphy in this study. Sixty-three total lymph nodes were excised in 24 identified lymph node basins. Of these 63 nodes, 60 nodes were found to be sentinel by the criteria of being the hottest node or within 10 % of the hottest node in that basin. In total, 6 sentinel nodes in 5 patients were found to be positive for metastasis, all of which were identified by the intraoperative imaging.

In 5 cases (25 %), additional information from the MGC images aided surgical decision-making. In one of the cases for example, the gamma probe missed a group of 3 nodes on the initial survey, which were in a group found to be harboring metastasis. These nodes were identified by the gamma probe after this cluster of nodes was visualized on intraoperative images using the MGC. In another two cases, the bed count continued to be higher than 10 % of the hottest node. The inspection of the energy histogram window demonstrated a lack of a well defined peak in the expected energy for ^{99m}Tc. This pointed to the signal likely being scattered by the tissue and coming from the deeper iliac region, which is usually not explored given the local practice guidelines. In both of these cases, the gamma camera helped avoid unnecessary surgery and decreased morbidity to the patient.

Gamma camera logistic scores were poorer for speed of node detection and for identifying the residual nodes in the first three patients (average 8 and 7.3 respectively) prior to the introduction of binning algorithms and persistence mode described previously in chapter 4, compared to the remaining cohort (average 1.8 and 2.3 respectively)

following the introduction of these features (p less than 0.01 in both cases). The scale for the scores goes from 1 to 10 with 1 being the best possible score.

5.2.3 Segmenting counts in images of ex-vivo SLNs versus gamma probe

A segmentation algorithm was described in chapter 4 for purposes of helping co-registration of gamma and visible/NIRF images in real-time. Another use for this segmentation algorithm is discussed here, with the goal of improving the accuracy of assessment of node activity during SLNB. As discussed in chapter 1, the standard guideline for lymph node mapping dictates that the surgeon removes all lymph nodes from the patient whose gamma probe count rate in-vivo exceeds one tenth of the count rate of the hottest lymph node ex-vivo. These count rate measurements are done with a non-imaging surgical probe that generally has a wide viewing angle. The combination of the large size of excised lymph nodes compared to the size of the pinhole aperture in non-imaging probe collimators and the strong dependence of non-imaging probe sensitivity with changing probe-to-source separation means that the excised node activity measured using the probe can be inaccurate. Furthermore, operator dependence was observed during the MEL54 study when comparing surgeon's and resident's gamma measured probe count rates of the same nodes. This problem could be readily resolved by using the gamma camera and the segmentation algorithm to have reliable and consistent real-time count rate information in the OR. Table 3 shows the count data for the ex-vivo nodes from the MEL54 study acquired by using the gamma probe compared to the segmentation algorithm and the gamma camera (second and third columns respectively).

Patient number	Gamma probe count (10 seconds)	Gamma camera count (60 seconds)	Gamma probe activity [kBq]	Gamma camera activity [kBq]
4	21315	4869	92.7	184.3
4	3292	495	14.3	18.7
6	23965	4545	104.2	172.0
7	1459	297	6.3	11.2
7	2768	405	12.0	15.3
8	5255	1008	22.8	38.2
8	3911	909	17.0	34.4
8	2131	270	9.3	10.2
8	1402	144	6.1	5.5
8	1359	216	5.9	8.2
8	1721	180	7.5	6.8
9	19573	4518	85.1	171.0
9	2872	1350	12.5	51.1
9	3919	2061	17.0	78.0
9	3646	1890	15.9	71.5
10	8152	3627	35.4	137.3
11	15133	2358	65.8	89.3
11	17794	2835	77.4	107.3
11	2583	162	11.2	6.1
11	8283	783	36.0	29.6
12	2496	297	10.9	11.2
12	6416	1242	27.9	47.0
12	1922	171	8.4	6.5
13	7702	1251	33.5	47.4

Patient number	Gamma probe count (10 seconds)	Gamma camera count (60 seconds)	Gamma probe activity [kBq]	Gamma camera activity [kBq]
14	4387	3168	19.1	119.9
14	29269	3960	127.3	149.9
15	3734	450	16.2	17.0
15	19978	4410	86.9	166.9
15	10756	1620	46.8	61.3
17	5146	1431	22.4	54.2
17	5443	1323	23.7	50.1
17	2422	216	10.5	8.2
17	1209	63	5.3	2.4
18	11474	6516	49.9	246.7
18	2526	414	11.0	15.7
18	2689	360	11.7	13.6
18	4695	495	20.4	18.7
19	1217	36	5.3	1.4
19	4806	783	20.9	29.6
19	19049	2889	82.8	109.4
19	5319	1017	23.1	38.5
21	54170	9315	235.5	352.6
21	32093	5013	139.5	189.8
21	17063	765	74.2	29.0
22	52727	7749	229.2	293.3
22	43902	5490	190.9	207.8

Table 3: Comparison of the MEL54 data from ex-vivo SLN counts from gamma camera and gamma probe

The fourth and fifth columns in Table 3 show calculated activities of the LNs from the clinical count data from gamma probe and gamma camera respectively. The gamma probe measured activity was calculated from the second column data. First, the gamma probe number of counts data was divided by 10 to get the count per second value. Then, it was divided by a value of 23 cps/kBq, that corresponds to maximum sensitivity of a point source as measured with the C-Trak Omni probe equipped with a standard collimator that was used in the MEL54 clinical study (97). The gamma camera measured activity was calculated from the third column data. The gamma camera number of counts data was first divided by 0.85, to account for the absorption efficiency of the $LaBr_3$ scintillator material at the energy of 140 keV (35). This number was then divided by the geometric efficiency of the parallel hole collimator, which is $5.2 \cdot 10^{-4}$ to acquire the activity of the source as measured by the gamma camera.

The average and median percent differences between the measured activities by the gamma probe and the gamma camera from this data are 52 % and 35 % respectively. This large percent difference supports the prior discussion regarding the likely inherent errors in acquiring the accurate number of counts and hence measured activity using the gamma probe. This comparison was not one of the endpoints of the surgical study, but the implications of this data can be used to potentially improve future procedures.

Segmentation algorithm used with the mobile gamma camera has been tested in bench-top experiments with lesions of differing activities of ^{99m}Tc-pertechnetate, showing a linear relation between the measured activity acquired from the number of counts measured by the algorithm and the true activity of the lesions. The accuracy of the measured activity as well as the variability of the measured activity versus actual activity

across the range of lesions of different sizes and activities was tested. The results of these tests further support the notion that the gamma camera segmentation algorithm can be used during SLNB as an improved method to accurately and more consistently measure the number of counts in LNs ex-vivo and in-vivo. The improvements in accuracy of the available information about the LN activity would arguably help surgeons' improved intraoperative decision-making.

CHAPTER 6: VISIBLE/NIRF SYSTEM CHARACTERIZATION AND RESULTS

One of the crucial steps in development of an imaging system is characterizing its performance, especially in tasks for which the system was developed for. In this section, the bench-top characterization and animal studies using the visible/NIRF subsystem of IMIS will be discussed in more detail.

6.1 Visible/NIRF system characterization in bench-top testing

The results of characterization tests of the visible/NIRF system in basic bench-top setups and in more task-specific imaging situations will be presented in this section.

6.1.1 Resolution tests

One of the fundamental characterizing parameters of an imaging system is its spatial resolution. A method that is widely accepted for optical resolution measurements utilizing the contrast transfer function (CTF) is used to evaluate spatial resolution of the optical part of IMIS (98; 99). The U.S. Air Force (USAF) 1951 resolution test chart (Figure 59) was used to determine the spatial resolution of the optical subsystem. This chart consists of groups of horizontal and vertical bars, each consisting of three sets of

black and white bars, called line pairs (lp). The spatial resolution of the bar sets as determined by width of the bars is given by the expression:

$$\text{Resolution(lp/mm)} = 2^{\text{Group}+(\text{element}-1)/6} \qquad \text{equation 7}$$

where the elements range from 1 to 6 and groups range from -4 to 7.

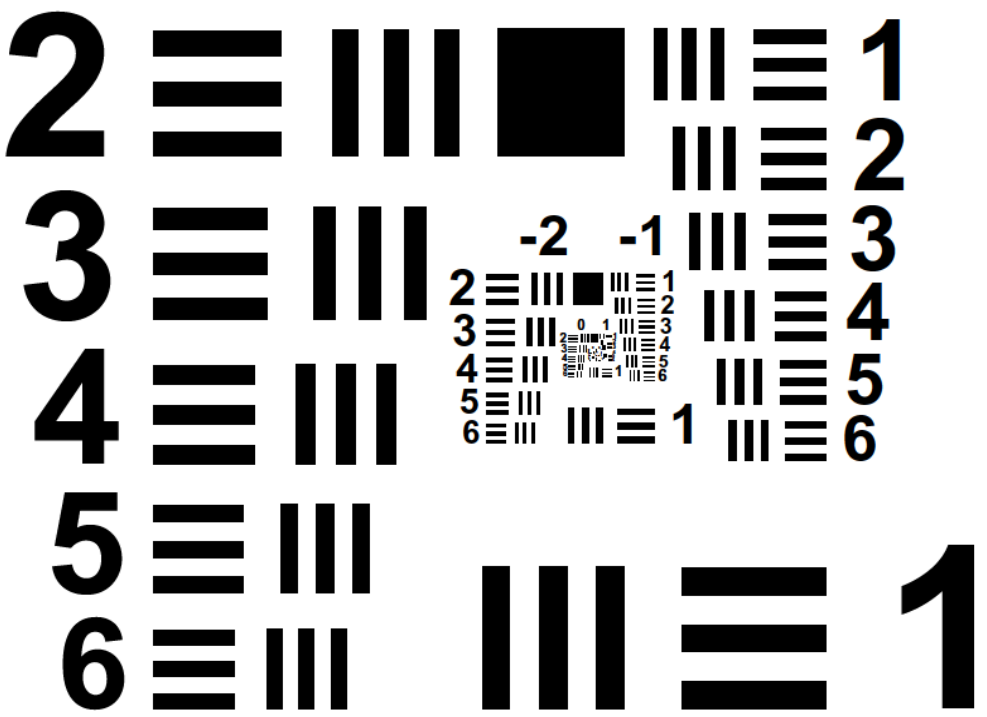

Figure 59: Image of the USAF 1951 standard resolution target

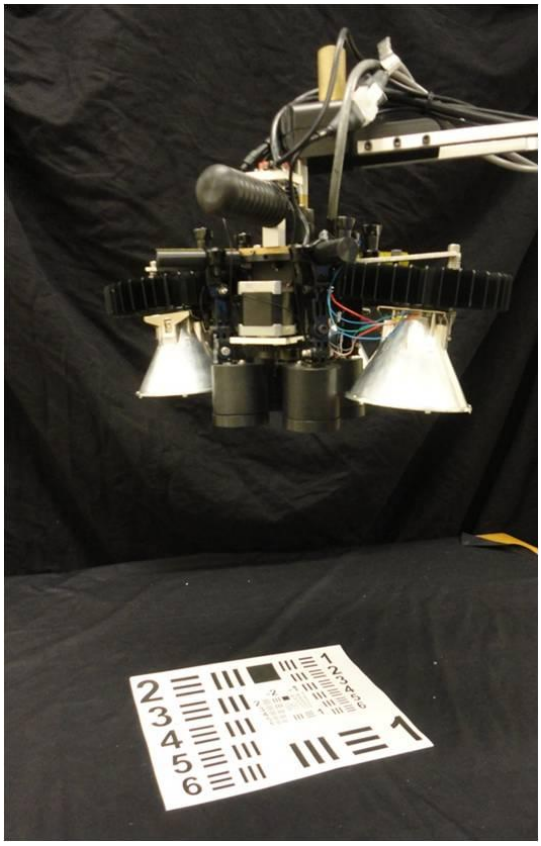

Figure 60: Imaging setup for measuring CTF

The USAF resolution test chart was placed at the optimal working distance of 30 cm below the camera, and an image was acquired in a typical imaging mode with a 1/30 s exposure (Figure 60). After imaging, the cross-sectional intensity profiles from each horizontal and vertical bar element were extracted, and the CTF for each group of bars was obtained following the equation:

$$CTF(f) = \frac{I_{max}(f) - I_{min}(f)}{I_{max}(f) + I_{min}(f)} \qquad \text{equation 8}$$

where I_{max} and I_{min} are the average maximum and minimum intensity values in the cross-sectional profile of a bar pattern, and f is the number of line pairs per millimeter (lp/mm) which corresponds to the respective bar pattern. The graph of the CTF versus f is then produced by repeating this process over a range of f values. Figure 61 shows two CTF graphs for the horizontal and vertical directions of the bars. To determine the horizontal and vertical resolution of the system from this data, the Rayleigh Criterion is used. This criterion defines the spatial resolution in terms of ability to resolve the dark bar stripes, as the point at which the minimum of the Airy disk object of one dark bar element coincides with the maximum of the Airy disk of the neighboring element. The contrast between the two objects becomes about 26.4 % at this limit. The line pairs corresponding to this contrast in were found to be respectively 1.71 and 1.75 lp/mm. The measured resolution values agree well with similar NIRF imaging systems (99; 52).

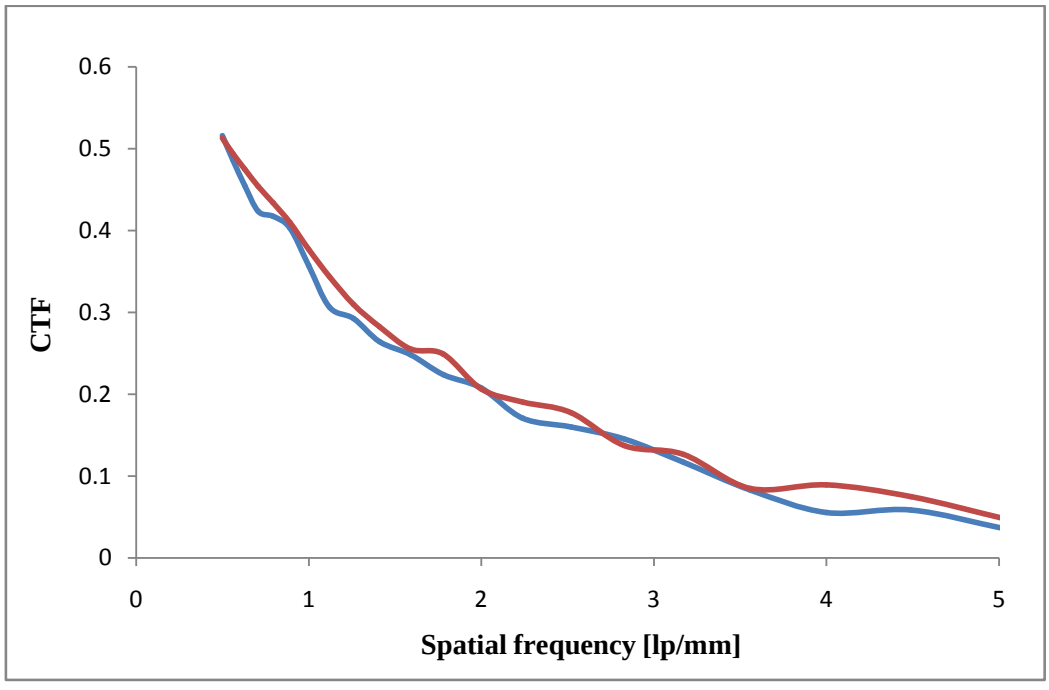

Figure 61: Measured horizontal and vertical CTF graphs

6.1.2 Sensitivity tests

The next parameter for evaluating the visible/NIRF system is the detection sensitivity. In this type of imaging, the true target image is formed by weak signals emanating from very low concentrations of targeted fluorophores. It is crucial to minimize the amount of background arising from leakage of light through the bandpass filters from the excitation LEDs by employing the optical filters of sufficiently high OD. In this section, the experiments undertaken to evaluate the detection sensitivity of the visible/NIRF system are described and the results of these tests are presented.

6.1.2.1 ICG concentration test

A number of plates in a standard 96 well plate were filled with ICG solution that was diluted in phosphate buffered saline (PBS). The ICG concentration in these well plates was varied over a range of values from 0.54 to 277.5 µM. This range includes the concentration shown by Ohnishi et al. (26) to provide the highest signal-to-noise (SNR) ratio in similar tests (~ 10 µM). The well plate was positioned at the optimal WD of 30 cm and illuminated by the NIR LED with 2.3 mW/cm^2 of filtered NIR excitation light. Care was taken to position each plate at same position for each of these measurements. An image of a fused visible and NIRF image of a well plate is shown in Figure 62, with high to low concentrations being arranged from top left to bottom right corner.

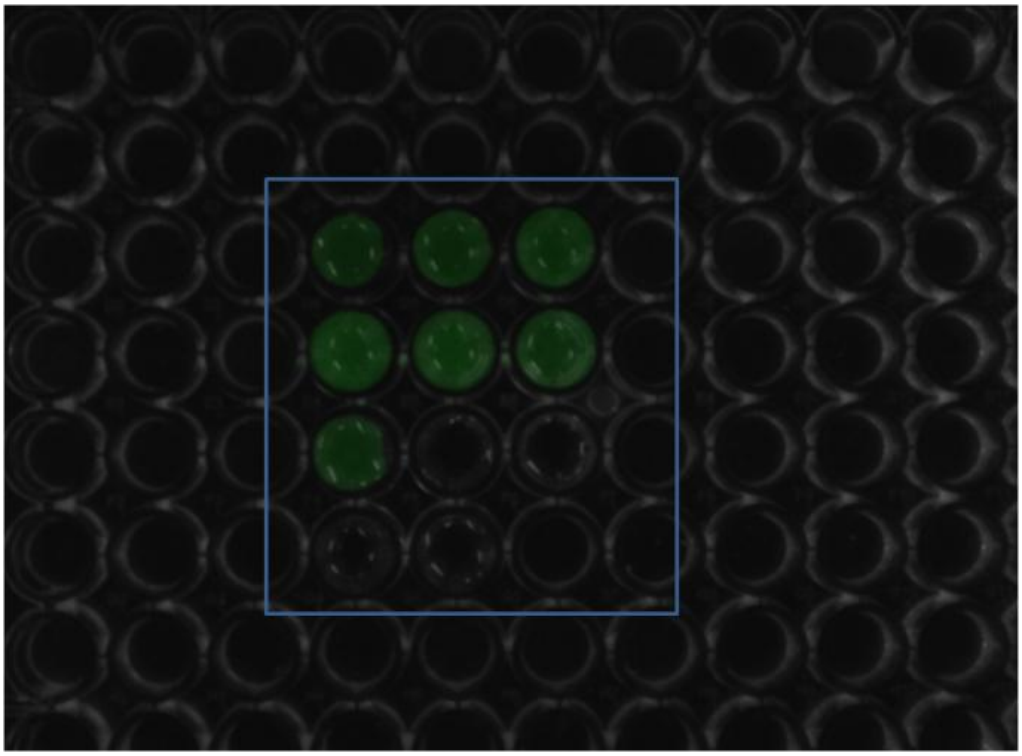

Figure 62: Visible/NIRF fused image of well plates containing ICG solutions of varying concentrations

The NIRF-only image was evaluated in ImageJ by measuring the average fluorescence intensity values for each well separately and calculating the respective SNR. The concentration yielding the highest NIRF SNR in our study was found to be 17.3 µM which can be seen in the graph in Figure 63, and agrees well with that reported by Ohnishi et al. (26).

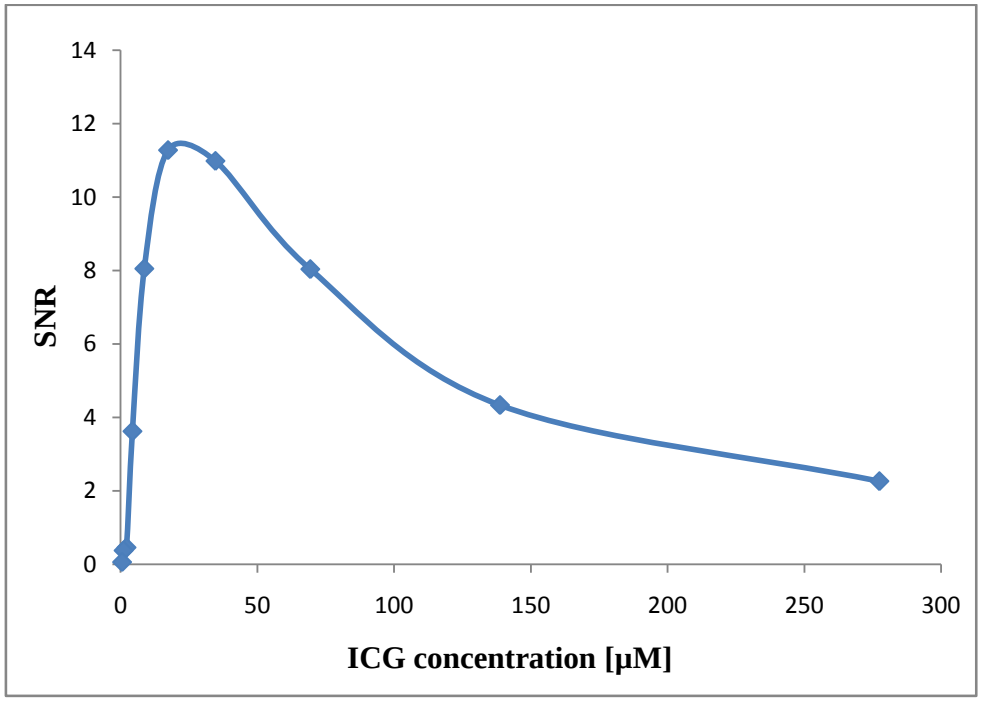

Figure 63: Measured SNR with respect to the ICG concentration

6.1.2.2. Lesion depth tests

Prior to performing the animal and human studies, the system performance needs to be evaluated in imaging tasks similar to the ones encountered in practice. More specifically, phantoms with similar optical and gamma attenuation properties to human tissue that also have embedded radioactive and fluorescent targets inside of them need to be imaged. This is an intrinsic component of evaluating an imaging system. However, considering that the field of NIR fluorescence has developed considerably over the last two decades, a routine set of phantoms for evaluating the imaging systems has not been developed. A number of different techniques for phantom fabrication have been proposed (100; 101) for imaging system performance testing, calibration and optimization as well as assessing intraoperative techniques (102) and training of surgeons in use of these

imaging systems. The phantom models range from phantoms that are fat/lipid based and polymer/quartz glass microspheres based to phantoms that attempt to mimic the human tissue by using whole blood or hemoglobin as their base. These phantoms can be aqueous for performance testing or can contain gelatin or agarose to solidify the phantoms for the surgery simulation procedures. For simplicity of approach and ease of acquisition of the necessary phantom constituents, a fat/lipid based phantom approach with gelatin (when needed) was used in phantoms for characterizing IMIS.

Figure 64: Imaging setup for evaluating the NIRf penetration depth

To evaluate the penetration depth of the NIR subsystem, a box phantom was filled with liquid emulating optical properties of human tissue in the NIR region (103). This phantom is shown in Figure 64 and consists of a mixture of water (475 mL), 10 % Intralipid fat emulsion (25 mL) and black india ink (12.5 µL) that contribute to scattering and absorption parts of the total attenuation coefficient respectively. A spherical acrylic lesion (10 mm ID, 12 mm OD) was filled with a 17.3 µM ICG solution and gradually submerged in the Intralipid mixture while the images at varying depths of the lesion were acquired. The WD between the camera and the top of the imaging surface of the phantom was kept constant during this experiment as the lesion was submerged deeper into the mixture. The images were acquired with the room lights turned off, excitation NIR LED intensity of 5.2 mW/cm^2 at phantom surface, and at the WD expected to be used intraoperatively by surgeons (30 cm). These images were then evaluated in ImageJ and the SNR was calculated and plotted versus the lesion depth on a graph in Figure 65. The example images of the lesion visibility with increasing lesion depth in the Intralipid phantom can be seen in Figure 66.

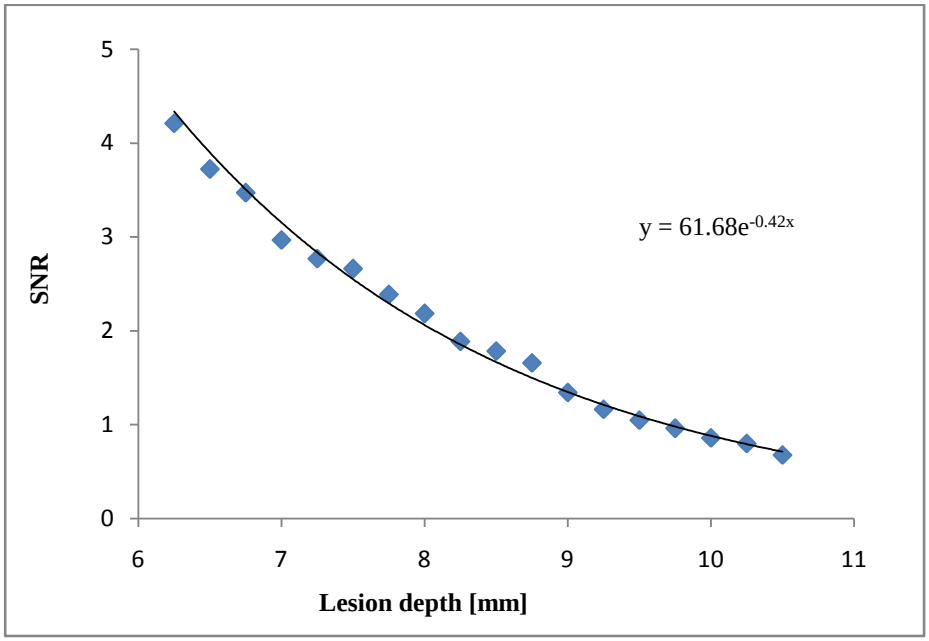

Figure 65: SNR of a lesion filled with ICG while being submerged in a tissue-like optical phantom

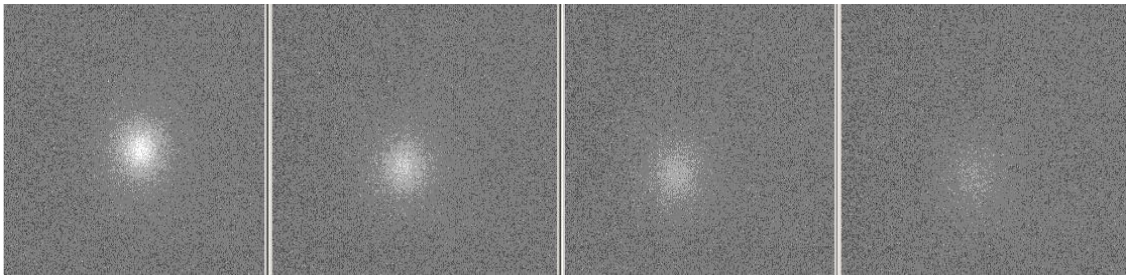

Figure 66: Example of lesion visibility with increasing depth of 6 - 10 mm (from left to right, identical window level)

6.1.3 LED characterization tests

The light sources are crucial components of an optical imaging system. For the imaging tasks described in this dissertation, a NIR excitation source that can provide a high fluence rate at long working distance and with precise wavelength spectrum is

required. Additionally, a white light source to replace the OR lights due to their strong NIR component is needed. Tests were performed to characterize the performance of the light sources and computer modeling of the positions and tilt of the NIR LEDs was performed to maximize the uniformity of the illumination light over the surgical FOV.

6.1.3.1 NIR LED modeling

The emission of light from a fluorophore molecule is directly proportional to the amount of excitation light directed on it, up to the photobleaching limit where the fluorophore molecules can undergo irreversible damage and lose their ability to fluoresce. Therefore, it is important to provide the uniform illumination to all points in the surgical FOV to ensure that the imaged emission light distribution provides a good estimate of the actual tracer concentration distribution. Due to the nature of most surgical procedures, the surgical FOV is not a uniform surface and often contains an incision that makes the depth of field vary significantly. This effect is unfortunately hard to correct for fully, as it would require mapping the surface topography of the surgical FOV and applying calculated corrections to the local brightness of the NIRf image in real-time. For the purpose of building the IMIS prototype, maximizing the uniformity of the excitation light over a square flat FOV was pursued to minimize excitation non-uniformity under ideal conditions. Keeping the system size as compact as possible was taken into account while maximizing the absolute uniformity, in order to minimize the size of the camera head that the surgeons will be handling.

First, the radiation pattern from a single L760-66-60 LED from Marubeni America Corporation, Santa Clara, CA (104) was measured. The NIR LEDs are housed in customized delrin housing that helps minimize the excitation light leakage. This radiation pattern with the LEDs setup was measured in bench-top experiments in order to have the true radiation information that can be input in the model for the four LED light distribution and uniformity. Single LED illumination measurements were taken at a WD of 30 cm with a photometer (IF-PM, Industrial Fiber Optics, Tempe, AZ) translated across the illuminated field on a translation stage. The measured data agreed fairly well with the nominal radiation pattern provided by Marubeni, with noted differences in the orientation of the LEDs due to the focusing lens asymmetry (104) and a faster tail drop-off in the measured data due to the illuminated light being blocked by the LED delrin housing. This data was used as a starting point for modeling the light distribution in a four LED setup.

Modeling the light intensity distribution over the surgical FOV was performed using the commercial optical design software package LightTools (Optical Research Associates, CA). LightTools is a CAD-like, 3D optical engineering and design software that supports virtual prototyping, simulation and optimization as well as photorealistic renderings of illumination applications. The GUI for the LightTools four LED setup and the resulting simulated illumination data from the final four concentric LED setup can be seen in Figure 67.

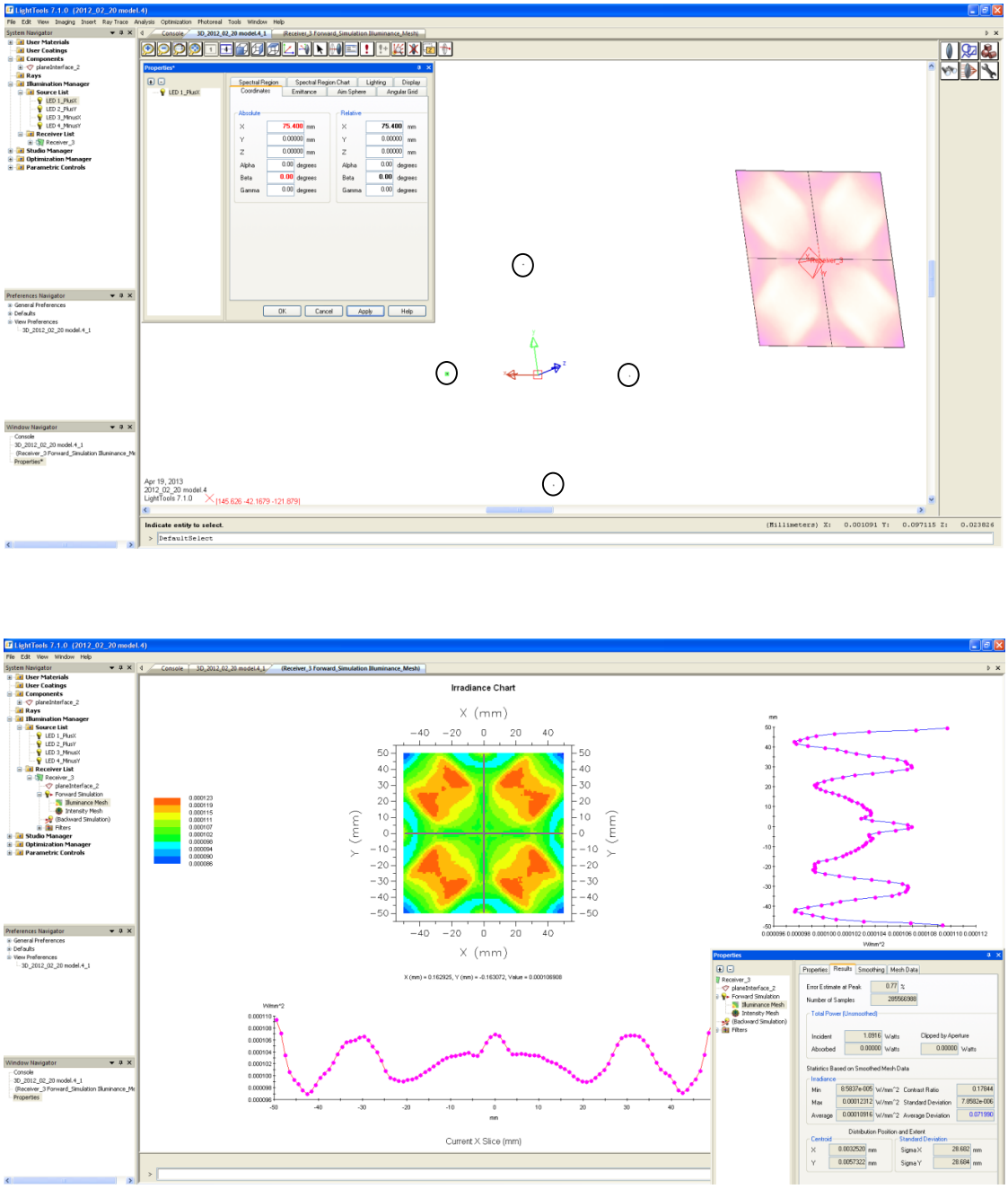

Figure 67: LightTools GUI showing the four LED illumination setup (top), user-defined LED position and tilt parameters (top left) and the resulting simulated illumination pattern (bottom)

On top screenshot of Figure 67, there are four dots (circled) located concentrically around the coordinate system, representing the positions of the LEDs in space, as well as the square planar receiver (right) that accepts the simulated light rays. The user can define all relevant parameters of the setup, like the position of the LEDs in space, angular tilt and illumination pattern of the LEDs, size of the receiver and the number of light rays to use for the simulation. The resulting final four LED setup illumination pattern is shown in the bottom screenshot of Figure 67 and shows the intensity across the FOV in color scale. Profiles drawn through user-defined cross-sections through the receiver are shown on the right and below the illumination pattern. Data on intensity and uniformity parameters of the resulting illumination pattern are shown at the lower right of this figure. The optimization tool called the parameter sensitivity utility (Figure 68) allows the user to set the limits of the position and tilt of the LEDs as well as the step size in which the software will perform the simulations to calculate the average deviation at each step.

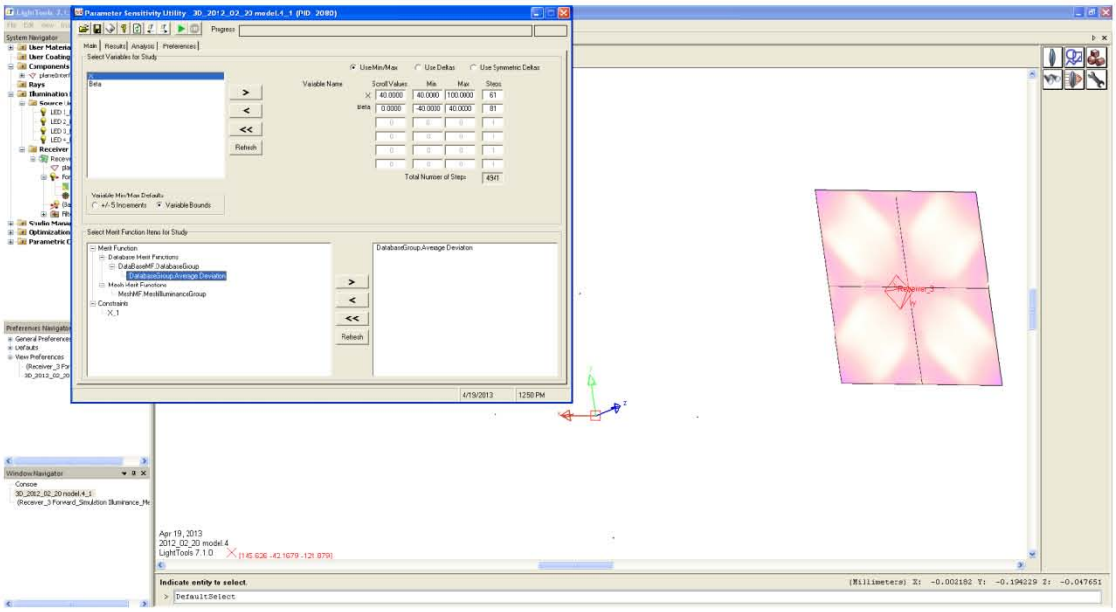

Figure 68: The LightTools Parameter Sensitivity Utility GUI

LED radial distances (center of LED to center of camera lens) from 40 to 100 cm and tilt angles from –40 to +40 degrees were considered for optimizing the IMIS LED positions. The ratio of the average deviation in the FOV to the average illumination power was chosen as the figure of merit, balancing the uniformity of the illumination in the FOV and the average fluence rate. At the end of the optimization process, global minima in the figure of merit were located in order to determine which LED position and angle would be most appropriate. Figure 69 and Figure 70 show the simulation results, plotting the average deviation value for a variety of LED radial position and tilt combinations, using a WD of 30 cm. For this working distance, the global minima were found along the light blue line in Figure 69. After thorough optimization post PSU modeling, the minima at 75.4 mm radial distance and 0 degrees tilt and 57 mm distance and 24.2 degree tilt were selected for further consideration.

Figure 71 shows the final optimized 4 NIR LED model for the 75.4 mm radial distance and 0 degrees tilt case. The model was simulated with 1 billion rays to produce a smooth profile across the receiver, which simulates the surgical field of view. The effects of the individual LEDs are obvious in the resulting profile due to the strict window level on the incident irradiance axis. One might argue that with presence of an incision in the surgical FOV would require the peaks caused by the LEDs in the irradiance profile to be in the center of the illuminated FOV to account for the greater depth of field at the incision. However, the incision might not necessarily be positioned in the center of the surgical FOV as viewed by the visible/NIRf system; in this case, it would be beneficial for the illumination profile to contain multiple peaks, as is the case with the final illumination profile presented here.

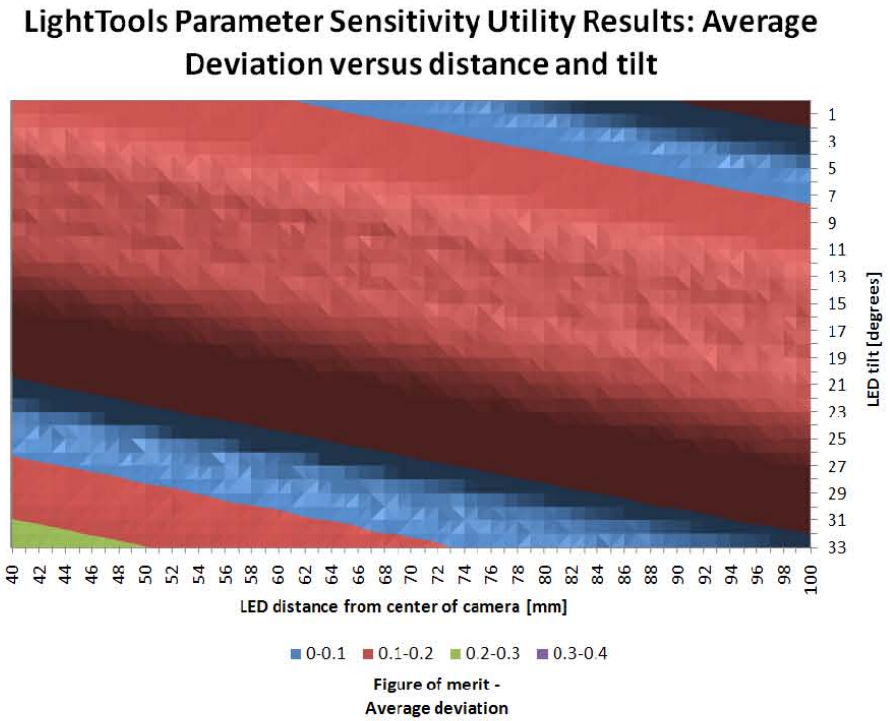

Figure 69: LightTools Parameter Sensitivity Utility: Average Deviation

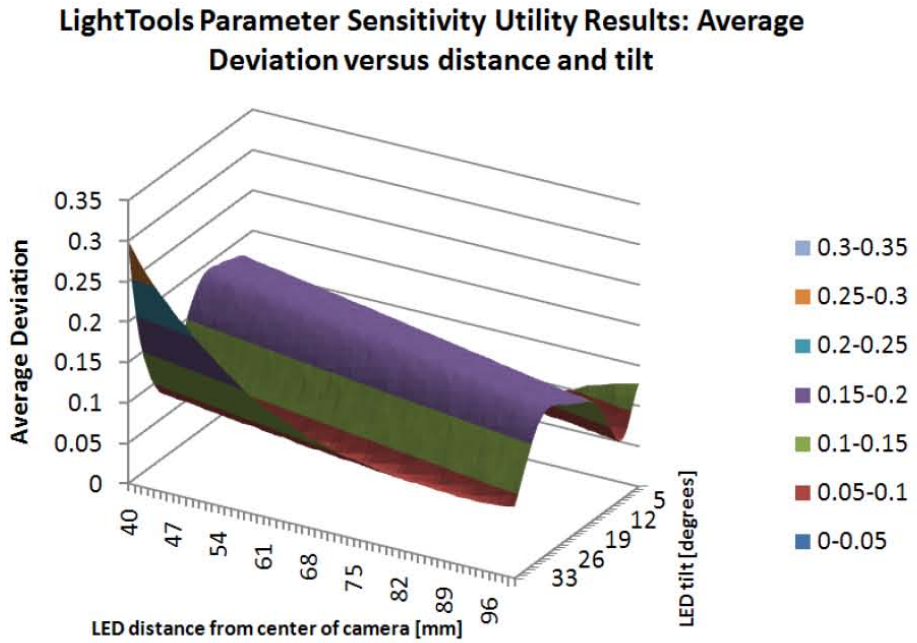

Figure 70: LightTools Parameter Sensitivity Utility: Average Deviation (3D view)

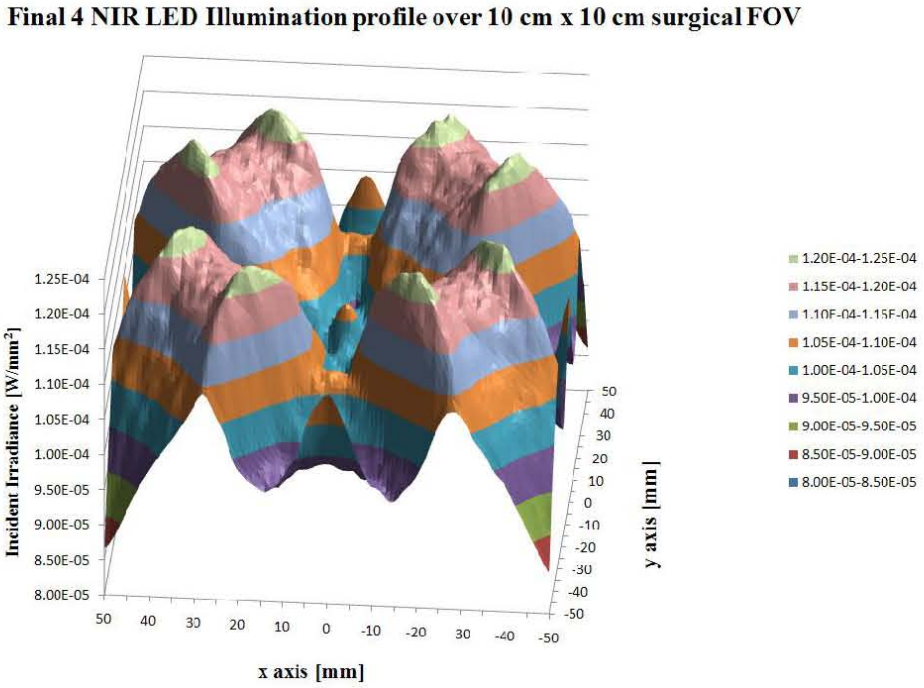

Figure 71: Final 4 NIR LED Illumination profile over the surgical field

Furthermore, it is important to consider how the average deviation value will change as the WD changes, as it is unreasonable to assume that the surgeons will be able to place the visible/NIRF camera at the same distance above the patient every time.

Figure 72 shows a graph of the average deviation versus the WD for the two setups chosen above, showing that compared to using 24.2 degree tilt, using zero LED tilt produces much less varying average deviation value over the whole range of WDs. The figure shows that the uniformity merit function is much less affected when the WD is increased beyond 30 cm with zero tilt. The divergence of the centers of the illumination regions of the individual LEDs causes the higher non-uniformity of the 24.2 degree tilt geometry as shown in Figure 73.

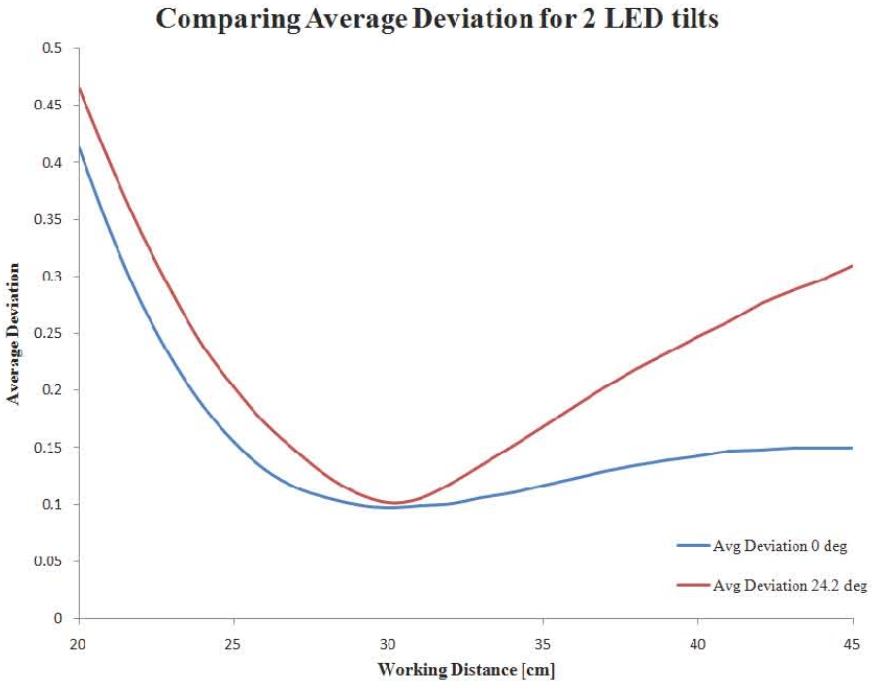

Figure 72: Graph of the average deviation versus working distance

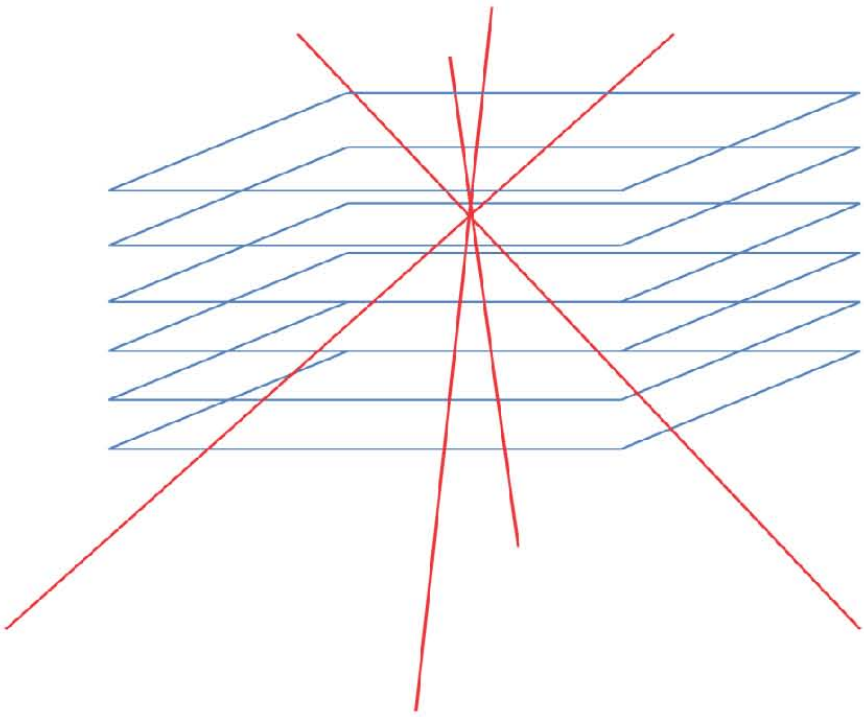

Figure 73: Illustration of the divergence of the centers of illumination of four individual LEDs for an LED tilt of 24.2 degrees as the WD is changed

Future improvements of the NIR excitation LED hardware might include motorizing the LED position depending on the WD. In this setup, the LEDs would be moved to the appropriate position to optimize the uniformity over the surgical FOV every time the back of the gamma camera was imaged for the co-registration purposes as described in chapter 4. LightTools was utilized to minimize the average deviation over the surgical FOV as the radial position of the excitation LEDs was changed, keeping the LED tilt angle fixed at zero degrees. This was performed for a range of WDs. A graph of the NIR LED radial position producing the minimum average deviation is plotted versus WD is shown in Figure 74 and could be used as a starting point for future uniformity optimization work.

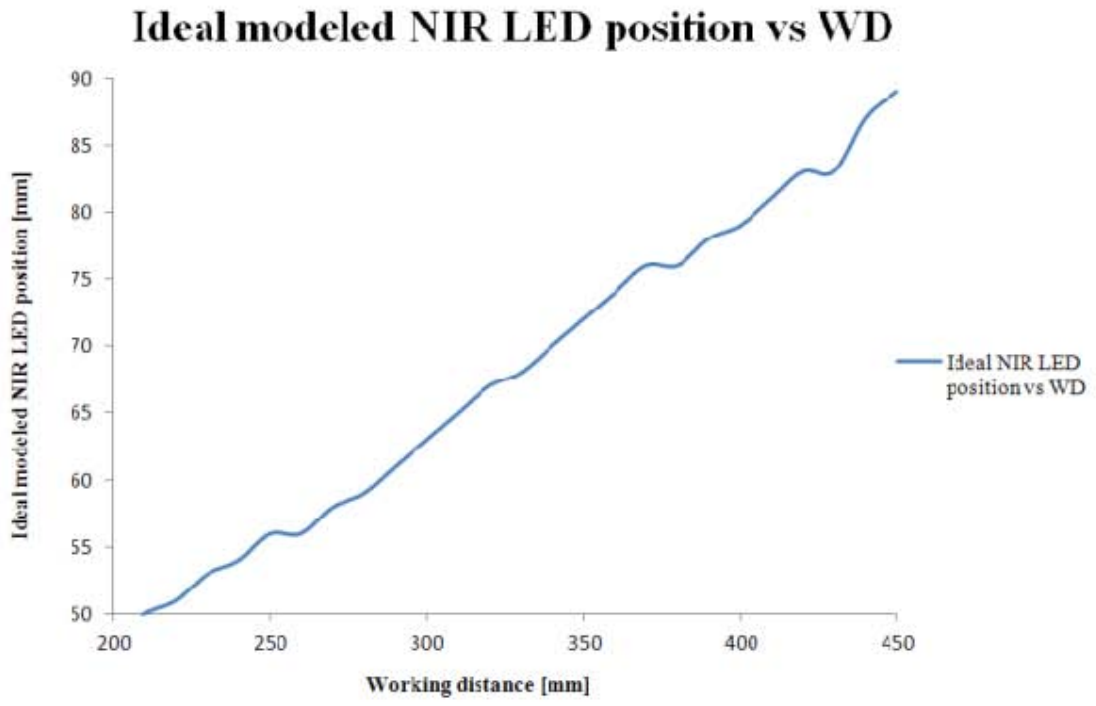

Figure 74: The ideal modeled NIR LED position for the zero degree LED tilt case versus WD

Finally, a comparison of the actual measured illuminance of the four LED model and the LightTools simulated data for the 75.4 cm radial LED distance and 0 degrees tilt case can be seen in Figure 75 with observed good agreement between the two cases.

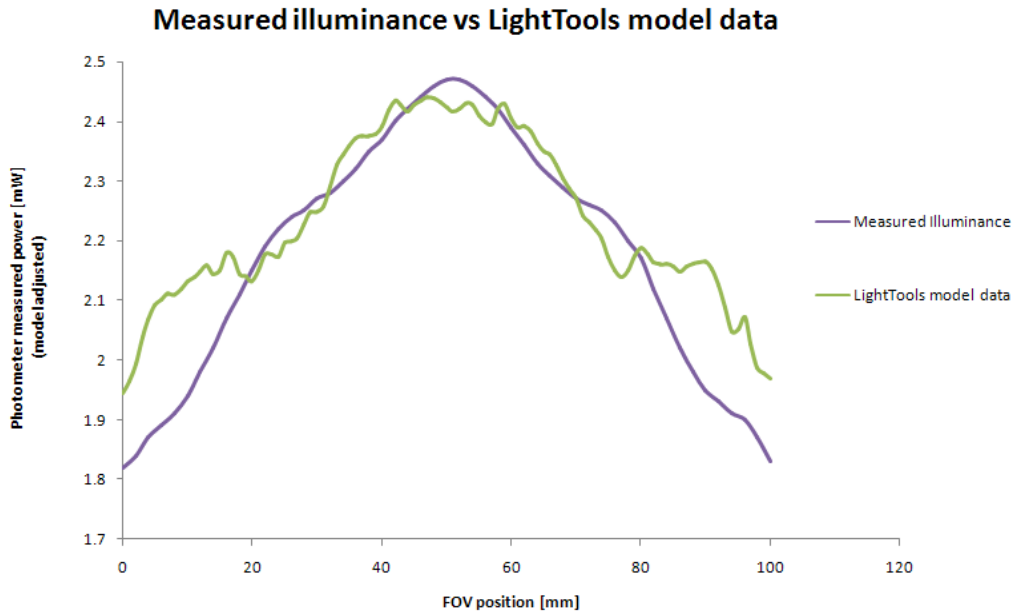

Figure 75: Four LED measured illuminance versus the LightTools model for the LED radial position of 75.4 mm, tilt angle of 0 degrees and a WD of 30 cm

6.1.3.2 RGB LED tests

The main purpose of the RGB LEDs is to provide the NIR-free light to the surgical FOV instead of the conventional OR lighting, which contains substantial NIR radiation. However, certain performance requirements need to be satisfied by the LEDs if they are to fully replace surgical lights. An international standard exists that defines the particular requirements for safety and the required performance of surgical luminaries and luminaries for diagnosis (IEC 60601-2-41). Two major requirements that this

standard poses are that the RGB lights used in the OR need to be able to provide between 40 and 160 kilolux (klux) of central illuminance to the FOV and that the color rendering index (CRI) and the correlated color temperature (CCT) of these lights have to be known and fall within certain limits. A good quality luminary according to this standard will have a CCT of 3000 K to 6700 K and CRI between 85 and 100 (105).

The RGB LED manufacturer's data only provides illuminance data at 1 m WD or above. Therefore, the illuminance at the WD of 30 cm for one RGB LED was experimentally measured with a lux meter and found to be 23.1 klux. The illuminance at a WD of 1 m was measured to be 2.4 klux, which agrees very well with the manufacturer's provided value of 2.34 klx. Hence, even two RGB LED units would in theory provide enough illuminance to satisfy the CIE illuminance requirements. However, due to non-zero visible light attenuation of the bandpass filters in front of the RGB LEDs as discussed in chapter 3, there is a slight reduction in the total white light illuminance of the RGB LEDs, and three RGB LEDs need to be used in this setup. The illuminance was measured with the bandpass filters in front of the three RGB LEDs at a WD of 30 cm. The central white light illuminance was found to be 46.2 klux after the LEDs reached their steady state temperature.

The CCT of a light source is by definition a measure of the apparent color of the light source and how closely the light spectrum of the illuminator resembles that of a black body irradiator. The CRI of a light source is a measure of the color shift that objects undergo when illuminated by the light source as compared with the color of those same objects when illuminated by an 'ideal' source (sunlight or a tungsten light source) at the same color temperature. Both of these parameters are directly related to the spectral

composition of the illumination light and require specialized equipment and methods to be correctly measured. In order to gain an approximate value for these values, the RGB LED light was projected on a white piece of paper, and the resulting apparent color of the paper was matched visually to the chromaticity diagram (Figure 76). The subjective assessment of the chromaticity coordinates averaged over three observers was calculated.

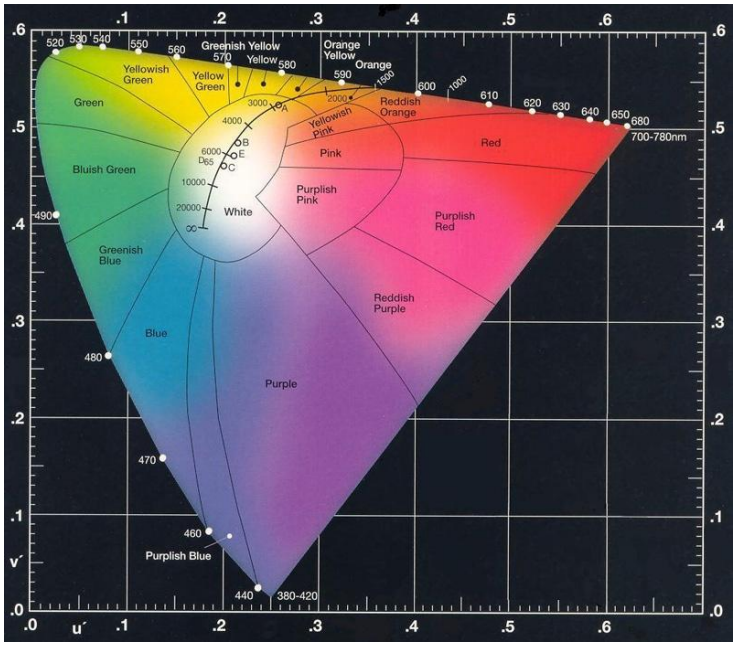

Figure 76: The 1976 CIE chromaticity diagram and the white color region defined by IEC 60601-2-41(106)

The relative intensities of the red, green and blue channels were adjusted until the averaged subjective CRI of the RGB LEDs fell within the CIE 1976 chromaticity diagram white color region (the central region in the center of Figure 76) confirming that the CRI value was in the satisfactory range. The CRI average value was recorded to be located at chromaticity coordinates of u = 0.21 and v = 0.46. These coordinates can be translated to the CIE 1931 chromaticity diagram chromaticity coordinates of x = 0.32 and

y = 0.31 (107). These x and y values on the chromaticity diagram were used to determine (108; 109) the CCT of the RGB LEDs to be 6180 K, which satisfies the IEC 60601-2-41 requirements. Finally, the light distribution of the RGB LEDs satisfies the minimum pattern requirements of the IEC standard (105), which requires that the pattern diameter (34.6 cm measured) at 50 % of the peak intensity must be greater than or equal to half of the pattern diameter (18.3 cm measured) at 10 % of the peak intensity (110).

6.1.4 Gelatin phantom tests

Simulated surgeries using tissue-simulating phantoms were performed to get an idea of how useful the IMIS will be in the OR and what logistical or performance parameters can be improved upon before the system is used in the OR. Multiple phantoms were constructed following the Intralipid recipe described above, with the addition of gelatin powder to solidify the phantom. A visible channel image of one of the first phantoms constructed and can be seen in Figure 77. This phantom contains two spherical acrylic lesions (10 mm ID, 12 mm OD) filled with a mixture of ^{99m}Tc-pertechnetate and the NIR fluorophore IRDye800 CW (111). This experiment was performed before the AHRS units were available, so the alignment of the positions of the gamma and the visible/NIRF modalities was achieved through a separate calibration procedure with two acrylic lesions prior to placing them in the gelatin phantom. In this calibration procedure, the gamma camera was placed below the lesions before placing them in the phantom and the visible/NIRF modality was observing the lesions from the top, with fixed relative positions of the two modalities. The acquired images of the

lesions provided us with fixed co-registration parameters that were used for the images acquired during the gelatin phantom experiment, during which the location of the lesions within the phantom was not known. The image showing the acquired gamma information overlaid on top of the visible channel image in the gelatin phantom experiment can be seen in Figure 78.

Figure 77: The visible channel image of a gelatin phantom mimicking the optical properties of human tissue, containing two spherical lesions filled with a radioisotope and a fluorophore

Figure 78: Signal from the gamma camera image (blue hue) overlaid on top of the visible channel image of the gelatin phantom from figure on the left

The gamma information would be useful to the surgeons prior to making the initial incision, with the visible optical and gamma information shown at the same time. Improved concept of using the outline from the gamma information only, instead of segmenting and ‘coloring’ the whole area within the ‘hot spot’ can be seen in Figure 79, which is an excerpt from the video of a simulated surgery performed on a gelatin phantom similar to the one described above.

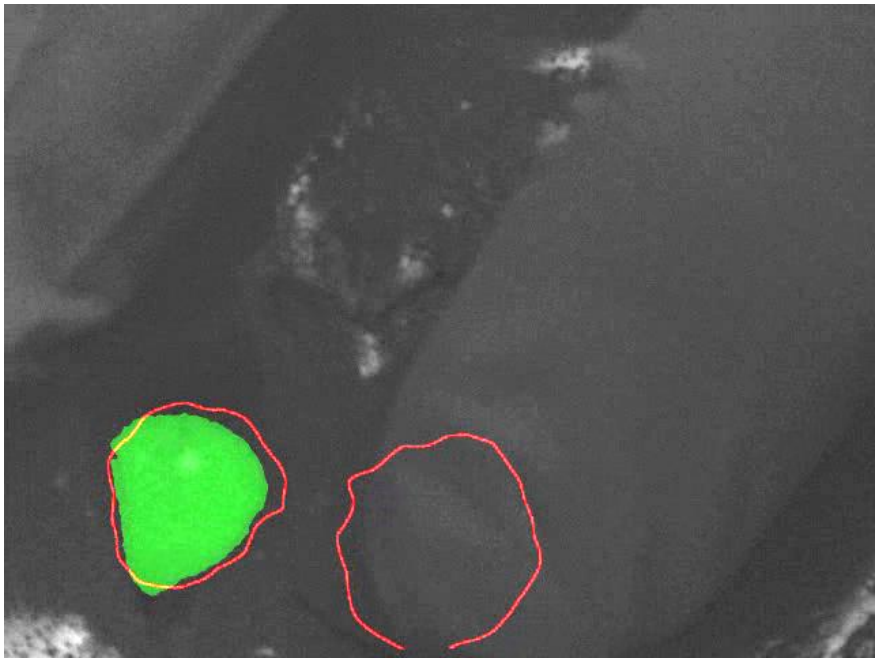

Figure 79: A still image capture from the video of the simulated surgery performed on a gelatin phantom

For the phantom surgery in Figure 79, two spherical acrylic lesions (10 mm ID, 12 mm OD) were filled with a mixture of ^{99m}Tc-pertechnetate and ICG before being placed in the phantom. The phantom was positioned at a WD of 30 cm below the camera. The red circular curves correspond to the borders of the lesion images in the gamma camera image, and the green regions correspond to the fluorescence image of the lesions captured by the NIRF channel of the visible/NIRF camera. Note that the gamma camera signal from both lesions can be seen clearly while the fluorescence signal can only be seen from the lesion on the left, since the lesion on the right is being covered by surgeon's finger. The lesion on the left was seen even before the incision was made in the phantom as the acrylic lesion was close the surface. The imperfect congruence of the positions of the lesions as imaged by the gamma and NIRF cameras is partially related to the nature of imaging of each modality and the dynamic nature of the surgery itself. The

gamma camera typically integrates its images over a period of 30-60 seconds, after which the target boundaries are determined. On the other hand, the visible and NIRF images are updated at a rate of 30 frames per second. Consequently, observing the gamma camera image stay in one place as the patient skin is moved by the surgeon in real-time can be confounding to the untrained eye. The surgeons are aware of the static nature of the gamma information and understand that the gamma images are used as guidance when thick tissue prevents NIRF imaging. The real-time information from the NIRF channel is the true information when the target is near the surface and the surgeon is manipulating the patient skin and tissue. The gamma camera image at that point bears less weight to the actual true position of the target. The surgeons are aware of the static nature of the gamma information and understand that the gamma images are used as guidance when thick tissue prevents NIRF imaging. The concept of displaying the gamma and visible/NIRF information shown in the still image, as well as in the full video of the phantom surgery, was accepted by the surgeons in terms of how it presents information to the surgery. This novel information is anticipated to improve the intraoperative decision making during future clinical SLNB and tumor surgeries.

6.2 Visible/NIRF system in animal studies

The most significant test of the system prior to using it in the OR within the upcoming human studies is in animal studies, where the surgical issues and procedures would most closely resemble the real imaging task anticipated in the human studies. In this section, the mouse studies in which one or both modalities of IMIS were used to image the radioactive and fluorescent tracers that were injected in the mice will be presented.

6.2.1 NIRF mouse imaging studies

The initial animal imaging used the NIRF video camera only, and was qualitative in nature. A nude mouse was inoculated with MCF-7 breast cancer cells into four different mammary pads. Tumors were allowed to develop over a period of several (4-5) weeks. On the day of imaging, the mouse received tail vein injection of PC-1007, a novel breast tumor-targeting tracer developed by Dongfeng Pan, PhD (112). The tracer is fluorescent in nature and its optical excitation and emission spectra are similar to those of ICG, which allowed the IMIS to be used without changing the optical filters. Figure 80 is a screenshot obtained with the visible/NIRF camera at a WD of 30 cm with the NIRF excitation and RGB LEDs on and shows that the fluorescence from four breast tumors can be clearly visualized.

Figure 81 shows the four tumors after excision and dissection. The tumors were imaged ex-vivo and show a non-uniform distribution of the tracer within the tumors.

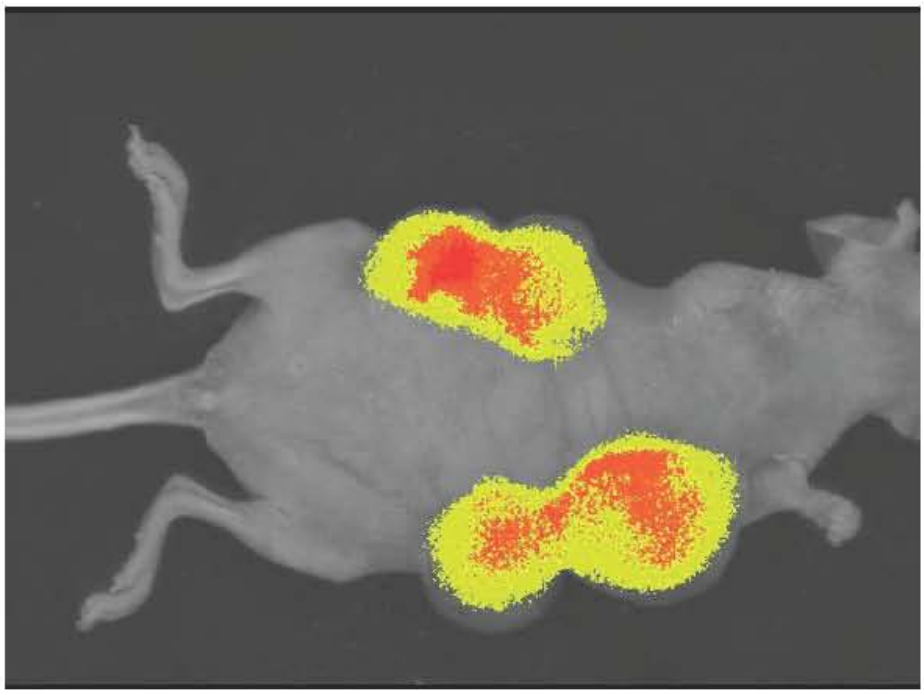

Figure 80: Visible/NIRF image of anesthetized mouse

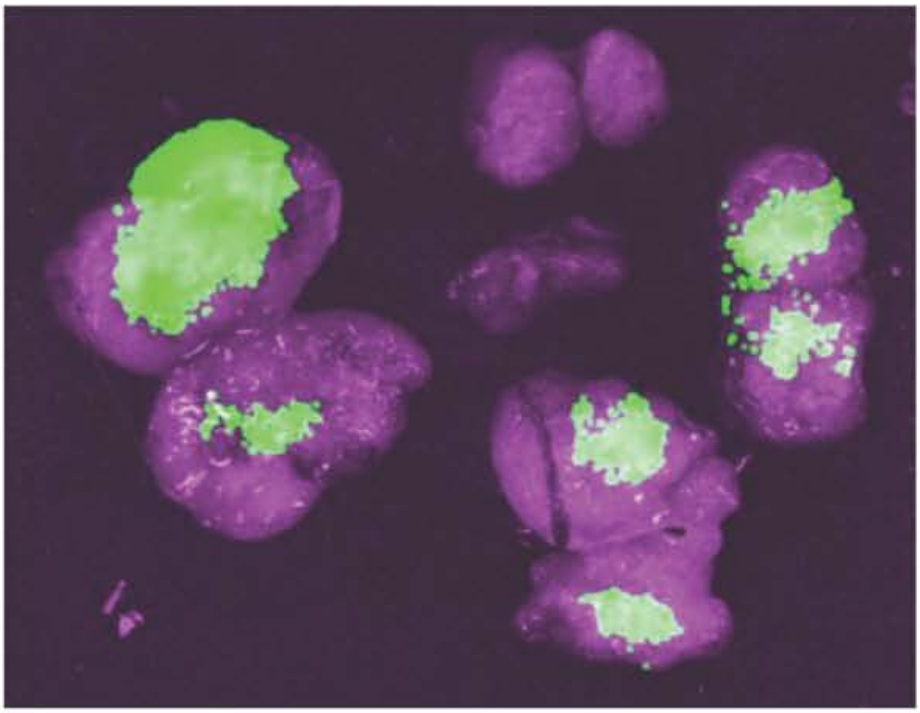

Figure 81: Visible/NIRF image of excised and dissected tumors

6.2.2 Full system mouse imaging studies

After developing the automated co-registration process, imaging a mouse by using the full IMIS system with co-registration of gamma, visible and NIRF images was performed. In this experiment, a female athymic mouse was inoculated with MCF-7 breast cancer cells into four different mammary pads. Tumors were allowed to develop over a period of several (4-5) weeks resulting in two tumors on each side of the mouse on the anterior side. The mouse was on a TD.94096 non-fluorescent diet (113) for several days prior to imaging to minimize the observed strong autofluorescence signal seen in prior NIRF mouse imaging experiments that was caused by their regular diet (not shown here). On the day of surgery and imaging, the mouse was injected with ^{99m}Tc-PC-1007 via the tail vein injection. The mouse was then anesthetized, subjected to a tumor excision surgery and imaged with IMIS in various stages of the surgery. Two tumors on the left side of the mouse were excised first and placed next to the mouse. Lack of the NIRF signal coming from the left side of the mouse was observed (Figure 82) which assured the surgeon that the tumors were fully excised and no cancer cells were left behind in the mouse.

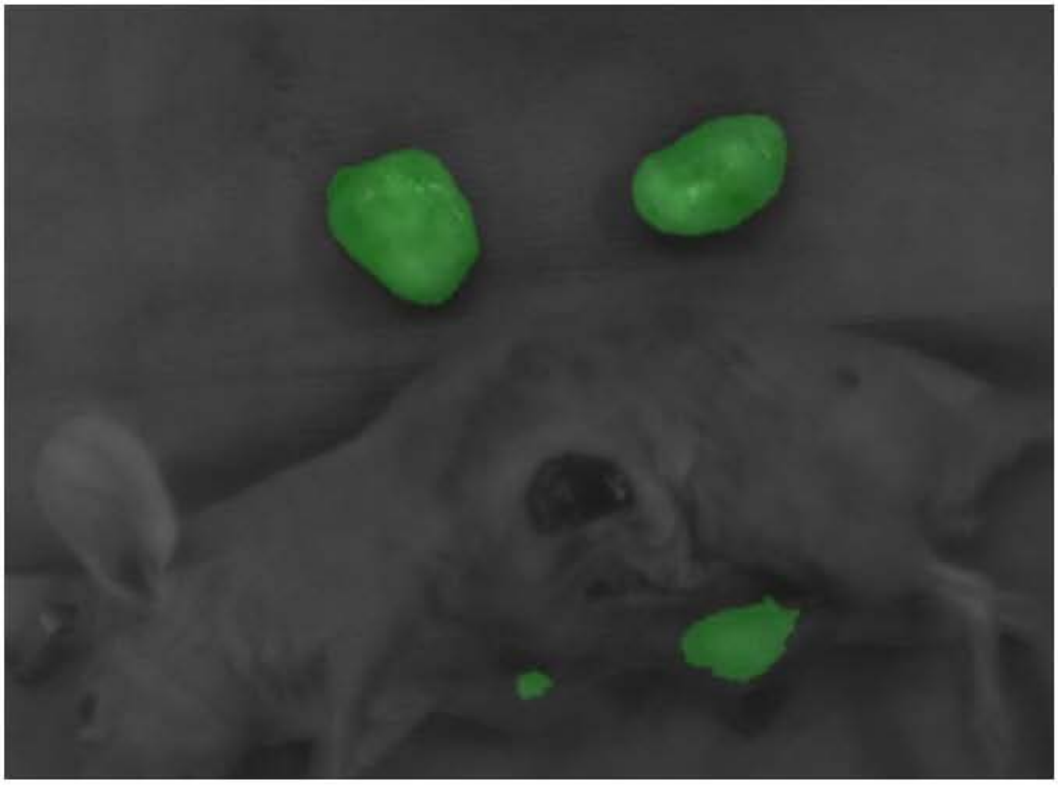

Figure 82: Visible/NIRF image of the anesthetized mouse with two excised tumors by its side

The tumors were then imaged with visible, NIRF and gamma modalities of IMIS. The gamma image was processed as described in chapter 4 to segment the tumor images and produce overlaid boundaries on the visible images. Figure 83 shows co-registered visible, NIRF (green) and gamma (white outline) images of one of the tumors that the surgeon chose during the co-registration process. Very good agreement between the spatial position and relative sizes of the signals coming from gamma and visible/NIRF modalities was observed, showing the proof of concept and successful IMIS operation.

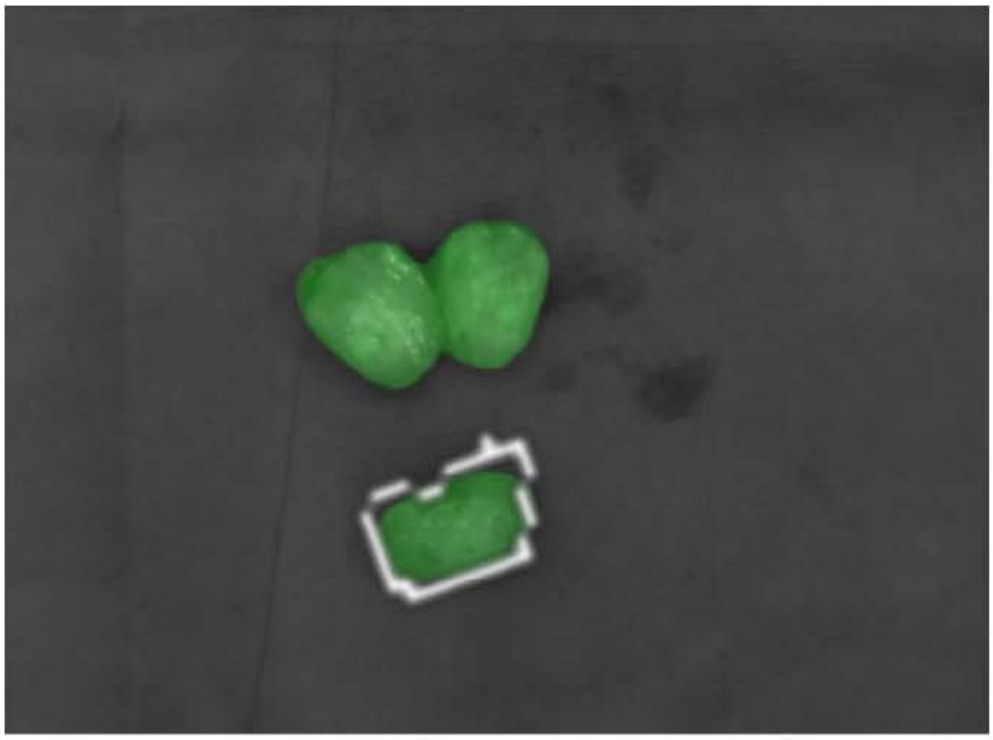

Figure 83: Visible/NIRF and gamma co-registered image of the excised and dissected tumors

6.3 Visible/NIRF system in human studies

As discussed in chapter 1, the NIRF imaging has been extensively used for intraoperative surgical guidance in variety of procedures including the SLNB and tumor excision for different types of cancer, burn assessment in plastic surgery, organ transplantation, lymphatic system drainage, intraoperative graft assessment and more. Keeping in mind the specialty of our surgical collaborators at the University of Virginia, we have an opportunity to test the IMIS in intraoperative SLNB guidance and tumor excision procedures. The IMIS is planned to be used in two upcoming clinical trials for melanoma and colorectal cancer SLNB with a novel gamma and NIRF tracer designed for SLN targeting (24). In this section of the dissertation, clinical trials with similar

scopes are reviewed as an aid in preparing for the upcoming studies and to have a frame of reference to compare the injected doses and concentrations of ICG. With non-imaging radionuclide-based SLNB presently a standard of care with fairly well-established tracer protocols, this review concentrated on NIRF trials and tracers used in them. More specifically, variations in dosage, concentration and injection techniques when using ICG as a tracer were documented, and the imaging instrumentation used and surgical results are described below in more detail.

Being the only currently FDA approved NIR tracer, ICG has been used extensively for testing novel NIRF imaging systems in SLNB procedures. In the past decade, the dose and concentration of ICG or its conjugates injected in humans for this purpose has varied widely. Additionally, the lymphatic pharmacokinetics of ICG can vary depending on physiology, age and body mass index (BMI) of the patient. Injection techniques for SLNB and position of the primary carcinoma and LNs are also crucial parameters in mapping the ICG flow, and often it is not known a priori if the patient has a compromised lymphatic system due to tumor metastases. Hence, diverse metrics were followed in reviewing the ICG use during SLNB procedures and they are discussed below.

Varying washout times of ICG from the SLNs exist, reported as low as 30 (114) or 25 (115) minutes from the ICG injection point, to 1 - 2 hours (116), 4 hours (117) or even several hours after injection (118). Similarly, the travel time from the injection point to the SLN was reported as low as 90 seconds (119) and 160 - 280 seconds (118) and upwards of 1 - 10 minutes (120), 5 minutes (121), within 5 minutes after injection for

most patients (122), 5 - 15 minutes (114) and 16 plus 17 minutes (from injection to incision plus from incision to reaching the first node) (123).

Two separate research groups have performed escalating dose studies to find the optimal ICG injection dose that would result in highest possible signal to background ratio ex-vivo in excised LNs. Sevick-Muraca (124) varied the injected doses of ICG from 0.31 µg to 100 µg in 24 consecutive women with breast cancer for SLNB (injected volume varied depending on the administered route). Their findings implied that the minimum injected dose of ICG for successful SLN mapping was 10 µg. Mieog (123) similarly escalated the concentration of ICG:HSA (human serum albumin) injected in SLN mapping procedures in 24 consecutive patients divided in 8 groups ranging from 50 µM to 1000 µM in a 1.6 mL volume. Their findings implied that the optimal injected concentration lies in the range of 400 µM to 800 µM. One of the key conclusions in their work was that the "...NIR fluorescent signal in the SLN is a complex function of the concentration of the injected NIR lymphatic tracer, the distance between the injection site and the SLN, the volume of ultrafiltrate within the lymphatic channels encountered by the NIR fluorophore, and retention of the NIR fluorophore by the SLN. Of these, only the injection concentration can be controlled".

Finally, ICG and ICG:HSA were compared for SLNB in breast and cervical cancer in two recent studies (125; 126), driven by the assumption that the ICG:HSA would be more appropriate for retention in the LNs due to its higher hydrodynamic diameter (26). However, these studies found no significant difference in fluorescence intensity and SBR, the number of excised lymph nodes or the time for the tracer to reach the LNs between using ICG or ICG:HSA. These studies noted the ICG is much easier to

use without the investigational new drug (IND) approvals in the institutional review board (IRB) protocol reviews compared to ICG:HSA.

Table 4 outlines the important tracer parameters for the SLNB clinical studies discussed above. These values were helpful in setting up the IRB clinical protocol for the upcoming melanoma and colorectal SLNB studies in which IMIS will be used.

Cancer type/ investigator	Number of patients	Imaging system	Injected ICG dose and volume [mg]/[mL]	Injected ICG concentration [M]
Breast cancer/ Kitai (120)	18	PDE	25 mg / 5 mL	6.4 mM
Breast cancer/ Ogasawara (119)	37	PDE	25 mg / 5 mL	6.4 mM
Breast cancer/ Hutteman (126)	18	Mini-FLARE	0.62 mg in 1.6 mL ICG:HAS or ICG	0.5 mM
Breast cancer/ Sevick-Muraca (124)	24	FDPM	0.31 µg to 100 µg / 0.1- 0.3 mL intradermally OR 1 - 3 ml subcutaneously	N/A
Breast cancer/ Tagaya (115)	25	PDE	5 mg in 4 mL mixed with blue dye	1.6 mM
Breast cancer/ Hirche (114)	43	IC-View	11 mg average	N/A
Breast cancer/ Troyan (127)	6	FLARE	0.4 mg in 1.6 mL ICG:HSA	10 µM
Breast cancer/ Mieog (123)	24	Mini-FLARE	62 µg to 1.25 mg in 1.6 mL	0.05 – 1 mM
Breast cancer/ Murawa (116)	30	IC-View	5-15 mg in 1-3 mL	6.4 mM
Melanoma/ Fujiwara (128)	10	PDE	0.5 mg in 0.1 mL	6.4 mM
Melanoma/ Namikawa (118)	49	PDE	5 mg in 1 mL	6.4 mM
Melanoma/ Mizukami (129)	24	PDE	0.5 mg in 0.1 mL	6.4 mM
Cervical cancer/ Crane (130)	10	Munich	0.5 mg in 2 mL mixed with blue dye	0.3 mM
Cervical cancer/ Schaafsma (125)	18	Mini-FLARE	0.62 mg in 1.6 mL ICG:HSA or ICG	0.5 mM

Cancer type/ investigator	Number of patients	Imaging system	Injected ICG dose and volume [mg]/[mL]	Injected ICG concentration [M]
Lung cancer/ Yamashita (131)	31	N/A	10 mg in 2 mL	6.4 mM
Gastric cancer/ Tajima (132)	56	PDE	10 mg in 2 mL	6.4 mM
Oropharyngeal cancer/ Bredell (121)	8	PDE	10 mg in 1 mL	12.9 mM
Oral cavity or oropharyngeal cancer/ van der Vorst (122)	10	Mini-FLARE	0.62 mg in 1.6 mL ICG:HSA	0.5 mM

Table 4: Overview of injected ICG doses and concentrations in a range of cancer SLNB procedures

CHAPTER 7: DISCUSSION

Development of IMIS for intraoperative guided surgery was presented in this dissertation. The IMIS consists of an unique small FOV gamma camera based on the SiPM technology and a visible/NIRF system whose main components are a video camera capable of simultaneous visible and NIRF imaging and NIR LEDs for fluorophore excitation, with all hardware components integrated on a common mobile cart.

The gamma camera was developed in collaboration with groups from West Virginia University, Thomas Jefferson National Accelerator Facility and University of Virginia. The performance of this gamma camera in both bench-top experiments and a clinical study was evaluated. The camera has a small field of view of 6 cm diameter round, which makes it convenient for hand-held operation. It has an intrinsic spatial resolution of 4.2 mm, normalized energy spectra resolution of 21.1 % and sensitivity of 481 and 73 cps/MBq for one and two collimator options respectively.

Compared to similar developmental and commercial small FOV gamma cameras, the gamma camera described in this dissertation shows comparable or superior resolution and detection efficiency performance, and in a hand-held package. Aarsvold (133) reported development of a camera with larger FOV (127 x 127 cm^2) that was arm-mounted and had lower sensitivity (61 cps/Mbq) compared to the gamma camera developed in this dissertation, and which required longer acquisition times of 3 - 5 minutes. Vermeeren (85) has evaluated performance of a commercial gamma camera Sentinella that was also not hand-held. The 4 mm pinhole collimator dictated a varying

FOV that changed from 4 x 4 cm^2 to 20 x 20 cm^2 at WD of 3 and 15 cm respectively. Vermeeren reported very good intrinsic spatial resolution (ISR) of 1.8 mm and extrinsic spatial resolution (ESR) of 7 and 21 mm, detection efficiency of 319 and 18.5 cps/MBq at WD of 3 and 15 cm respectively and an energy resolution of 15.9 % in the range of 50 - 200 keV. Pitre (134) reported on development of a small FOV hand-held gamma camera POCI (per-operative compact imager) in breast cancer SLNB (93). POCI has a 4 cm diameter round FOV, ISR of 3.2 mm, an energy resolution of 32 % at 140 keV, and sensitivity of 290 cps/MBq.

Dengel (42) reported use of a 13 x 13 cm^2 FOV arm-mounted camera based on 3 x 3 x 6 mm^3 NaI:Tl scintillator with detection efficiency of 405 cps/MBq. Scopinaro (90) reported performance of a small hand-held camera that only weighs about 1 kg and has a 1 in^2 square FOV and ESR of 3 mm at 1 cm WD. Mathelin (135) reported performance of a small 5 x 5 cm^2 square FOV gamma camera based on 2 mm thick single crystal GSO:Ce scintillator and with a mass of 2.5 kg compared to 1.4 kg for the SiPM camera described in this dissertation. The ISR was measured to be 3 mm and the ESR was 10 mm at the WD of 5 cm, similar to that of the SiPM camera with a single collimator layer. The detection efficiency was 1.6 cps/MBq and the energy resolution was 45 % of the FWHM at 122 keV, both of which were inferior to those of the SiPM camera. Olcott (94) reported on performance characterization of a miniature high sensitivity gamma camera NodeView that weighs about 1.1 kg and was designed for use in SLNB for melanoma and breast cancer. This camera has a FOV of 5 x 5 cm^2, an intrinsic resolution of 1.8 mm, average energy resolution of 12 % FWHM at 140 keV and a sensitivity of 270 cps/MBq using a 15 mm thick collimator. Garbay (92) reported use of a small hand-held camera

Minicam II in breast cancer SLNB. This camera has a 4 x 4 cm^2 FOV, spatial resolution of 2.5 cm, mass of only 0.7 kg and a sensitivity of 200 cps/MBq at the WD of 1 cm. A commercial arm-mounted 2020tc imager from Digirad (136) was successfully used in breast cancer SLNB (137; 138). This imager is arm-mounted, has a 21 x 21 cm FOV, ESR of 18 mm at 15 cm WD, good energy resolution of < 14 % in the energy range 60 – 300 keV and sensitivity of 133 cps/MBq. Tsuchimochi (139) reported on the performance of a prototype CdTe-based gamma camera (SSGC) for radio-guided surgery. The SSGC has a 4.48 x 4.48 cm^2 FOV, ESR of 1.56 mm FWHM, an energy resolution of 7.8 % FWHM at 140 keV and sensitivity of 300 cps/MBq.

Table 5 shows a review of important technical properties of these devices.

Device/ investigator	Spatial resolution (FWHM) [mm]		Sensitivity [cps/MBq]	Energy resolution (FWHM) [%]	Field of view [cm x cm]	Optimal working distance [cm]	Logistics, handling and imaging time
	ISR	ESR					
GammaCAM/ Aarsvold 2006	NS	NS	61	NS	12.5 x 12.5	NS	Arm-mounted, 3-5 minutes
Sentinella/ Vermeeren 2009	1.8	7	319	15.9% (50 - 200 keV)	4 x 4	3	Arm-mounted
		21	18.5		20 x 20	15	
13 x 13 MGC/ Dengel 2011	NS	NS	405	NS	13 x 13	NS	Arm-mounted
2020tc/ Digirad 2007	NS	18	133	<14% (60-300 keV)	21 x 21	15	Arm-mounted
SSGC/ Tsuchimochi 2003	NS	1.56	300	7.8% at 140 keV	4.48 x 4.48	0	Arm-mounted
		6.3				5	
IP-821 Li-Tech/ Scopinaro 2008	NS	3	NS	NS	2.54 x 2.54	1	Hand-held, 1kg mass
CarollReS/ Mathelin 2008	3	10	1.6	45% at 122 keV	5 x 5	5	Hand-held, 2.5kg mass
NodeView/ Olcott 2007	1.8	4	270	12% at 140 keV	5 x 5	3	Hand-held, 1.1kg mass (wireless)
Minicam II/ Garbay 2009	2.5	NS	200	<10% at 140 keV	4 x 4	1	Hand-held, 0.7kg mass
POCI/Pitre 2003	3.2	3.9	290	32% at 140 keV	4cm diameter round	1	Hand-held, 1.2kg mass
		7.6				5	
FWHM, full width at half maximum; ISR, intrinsic spatial resolution; ESR, extrinsic spatial resolution; NS, not specified.							

Table 5: Gamma scintigraphy devices used for clinical trials of SLNB

The NIRF/visible optical system described in this dissertation was developed in-house and showed good performance in bench-top experiments, surgery simulating experiments and animal imaging. The spatial resolution was measured to be 1.7 lp/mm, and good delineation of NIRF signal was observed up to almost a centimeter in realistic tissue-like phantom experiments. Excellent co-registration of NIRF/visible and gamma images was observed both in surgery simulating gelatin phantom experiments and during animal imaging.

Compared to similar developmental and commercial NIRF imaging systems, the visible/NIRF system described in this dissertation shows comparable or superior performance overall. DeGrand (61) reported initial development of a fluorescence-assisted resection and exploration (FLARE) system, whose hardware and logistics was refined over time as reported by Troyan (127) and Mieog (123). These two systems have been used extensively in animal model trials (61; 140; 141; 142; 143) and human clinical trials including breast cancer SLNB (127; 123), ex-vivo colorectal SLN mapping (143) head and neck cancer SLNB (122) and cervical cancer SLN mapping (125). In terms of the reported imaging system characterization performance, the FLARE system (127) provides fluence rates of 40 klux and 14 mW/cm^2 of white and NIR excitation light respectively at the optimal working distance of 45 cm and a maximum FOV of 15 x 11.3 cm^2. Mini-FLARE (123) has a smaller footprint imaging head compared to FLARE, with improved logistics and handling characteristics that allows for imaging at more oblique angles to the patient. Its excitation light output is somewhat lower compared to FLARE, providing 26.6 klux and 7.7 mW/cm^2 of white and NIR excitation light respectively, and compares well to 46.2 klux and 5.2 mW/cm^2 provided by IMIS. The working distance of

mini-FLARE can be varied from 10 - 32 cm with an FOV of 12 x 9 cm^2 at 32 cm WD. This working distance and FOV compare well with the 30 cm WD and 8.5 x 6.5 cm^2 FOV of the NIRF system described in this dissertation. The camera acquisition time can be adjusted for both FLARE and mini-FLARE to range from 100 μs to 8 seconds, while the IMIS can accommodate 30 ms or shorter acquisition times. The size of the IMIS imaging head compares favorably even to the mini-FLARE system whose imaging arm weighs close to 45 kg.

Handa (144) reported development of a custom CCD system HyperEye (HEMS) for NIRF medical imaging applications that was used in intraoperative graft assessment as well as fluorescence guided SLNB in animal models (117). With its working distance of 50 cm and circular FOV with radius of 5 cm, the authors claim observing the NIRF signal from 1.5 - 2 cm depth in tissue, which is better than ~ 8 mm seen with IMIS. It is possible that the 760 nm excitation ring-light module in HEMS provides superior fluence rates compared to IMIS that increase the amount of fluorescent light emitted by the fluorophore. Coupled with a higher sensitivity CCD camera and a more rigorous rejection of background light (840 nm cut-on filter used), this could result in the superior SNR and depth penetration values reported. Ntziachristos reported development of an intraoperative fluorescence imaging system using light-absorption correction (145), which was subsequently used successfully in a cervical cancer SLNB (146) as well as for assessing intraoperative techniques in tissue simulating breast phantoms (147). This system uses a 750 nm laser diode and a beam expander and diffuser setup for fluorophore excitation and a 250 W tungsten halogen lamp for white light illumination and color imaging. The penetration depth of ICG for this system was qualitatively estimated to be

about 1 cm from the clinical study, which compares well to the penetration depth measured with IMIS. The maximum surgical field of view of 11.5 x 9.3 cm^2 at the WD of 21 cm of this system is slightly larger than the FOV for IMIS at WD of 30 cm. The measured resolution is superior to IMIS (7.4 lp/mm averaged between the horizontal/vertical CTF compared to 1.7 lp/mm in IMIS), but the sensor temporal resolution in this imaging mode is much worse than IMIS (12 fps vs 30 fps). The size of the imaging module of this system (45 x 6 x 41 cm^3) is comparable to IMIS at the moment (42 x 36 x 20 cm^3), but the IMIS imaging head handling allows for more degrees of freedom.

Sevick-Muraca reported development of an intensified CCD multiplexed NIRF imaging system (148) and its use in lymphatic flow imaging in breast cancer (124). Even with a 765 nm laser diode with 80 mW power for NIR excitation light, this system only provided illuminance of 1.9 mW/cm^2 over the FOV of 200 cm^2. The results of their clinical feasibility study were not notable due to the micro-doses of ICG administered, with only 27/49 SLNs being fluorescent; nevertheless, these results confirmed the proof of concept. In terms of commercial NIRF imagers, Kitai (120), Tagaya (115) and Ogasawara (119) all reported successful clinical results of breast cancer SLNB in 18, 8 and 37 patients respectively using Hamamatsu's Photodynamic Eye (PDE) system. Furukawa also reported use of PDE in SLNB in cervical cancer (149). Kitai observed signal from ICG solution embedded 1 cm in material mimicking optical properties of human tissue in preliminary phantom tests. PDE itself comes in a portable hand-held package with dimensions of 8 x 8 x 18 cm^3 and a mass of only 0.5 kg. The optimal working distance of PDE is 20 cm with the FOV of about 9 x 12 cm^2 at the WD of 15 -

25 cm with 760 nm LEDs for NIR light excitation and a CCD detector. Unfortunately, the data on fluence rates and other performance characterization of PDE is scarce (spatial resolution reported to be 3.17 lp/mm (150)), with this system being used predominately in clinical studies in Japan. IC-View from Pulsion Medical Systems (Munich, Germany) was used in breast cancer SLNB in 43 and 30 patients respectively (114; 116), plastic surgery applications in burn depth assessment (151) and small animal small intestine blood flow assessment (152). The IC-View system utilizes a 780 nm laser diode for NIR fluorophore excitation and an 835 nm filter at the CCD entrance aperture. However, the data on other performance characteristics of IC-View is limited, besides a quoted 2 cm fluorescence light penetration in tissue depending on the excitation light intensity. Another commercial NIRF imaging system, Novadaq Spy was used in various clinical medical imaging applications, including coronary and graft imaging (153; 154) organ transplantation (155) and other cardiac function assessment procedures (156). This imaging device consists of a laser diode and a driver that produces light at a wavelength of 806 nm with a maximum output of up to 2.7 W over a square FOV of 7.5 x 7.5 cm^2 at a WD of 30 cm. Fluence of 40 mW/cm^2 was reported in this work, which is below the exposure limit of 200 mW/cm^2 set by the American National Standards for Safe Use of Lasers (ANSI Z136.1); this fluence rate is superior to IMIS and below the photobleaching limit of ICG. The Spy system has been cleared by the Food and Drug Administration (FDA) exclusively for intraoperative imaging following the intravenous administration of ICG. The system can be used in a variety of applications including coronary artery bypass, cardiovascular, plastic, reconstructive, organ transplant and gastrointestinal surgery, but the SLNB and oncology applications have not been pursued to this point.

Hirche (150) reported use of a commercial hand-held NIRF imaging system Fluobeam 800 in assessing SLN mapping in pigs. He reported a mean depth detection of the ICG:HSA signal from lymph nodes at 2.5 cm depth, with the system having FOV of 7.5 x 10 cm^2 at the WD of 20 cm and spatial resolution of 4 lp/mm. The excitation source was a class 1 expanded laser with a very high NIR excitation light fluence rate of 100 mW/cm^2, which might have caused ICG fluorescence quenching during the animal imaging. Heuveling (157) used Fluobem 800 for head and neck SLNB in rabbits and reported similar performance metrics as Hirche with a 6 cm diameter illuminated FOV at 17 cm WD, but using a much weaker fluence rate of 9.6 mW/cm^2. A review of most important technical properties of the NIRF devices described above is shown in Table 6.

Device/ Investigator/ Company	Spatial Resolution	Working distance [cm]	Field of view [cm]	Excitation light fluence [klux] or [mW/cm^2]	Logistics/ Handling
FLARE/ Frangioni	125x125 µm to 625x625 µm	45	2.2 x 1.7 to 15 x 11.3	40 klux and 14 mW/cm^2	Arm-mounted
Mini-FLARE/ Frangioni	320 x 320 µm	10 - 32	12 x 9 at 32 cm WD	26.6 klux and 7.7 mW/cm^2	Arm-mounted
FDPM/ Sevick-Muraca	NS	< 76.2	round, 900 cm^2	<1.9 mW/cm^2	Arm-mounted
HyperEye/ Kochi	NS	30 - 50	round, 5 cm diameter	760 nm LED array	Arm-mounted
PDE/ Hamamatsu	3.17 lp/mm	15 - 25	9 x 12	760 nm LED array	Hand-held, 0.5 kg mass
SPY/Novadaq	NS	30	7.5 x 7.5	40 mW/cm^2	Arm-mounted
Fluobeam800/ Fluoptics	4	20	7.5 x 10	100 mW/cm^2	Hand-held
		17	6 cm round	9.6 mW/cm^2	
IC-View/ Pulsion Medical	NS	NS	NS	780 nm laser diode	Hand-held
Munich/ Ntziachristos	7.4 lp/mm	21	11.5 x 9.3	750 nm laser diode, 250 W tungsten lamp	Arm-mounted

Table 6: NIRF devices used for clinical trials of SLNB; NS, not specified

Regarding the future plans for use of IMIS, the gamma camera will be used by itself for recording data from different camera positions and reconstructing this data to a 3D model of a larger field of view (FOV), similarly to the freehandSPECT concept available from SurgicEye (158; 96). The IMIS is expected to be used in two clinical studies involving SLNB in melanoma and colorectal cancer patients. A novel ICG-^{99m}Tc-Nanocoll compound that showed great results in SLNB in Europe (24; 159) is anticipated to be used for injection as an ideal tracer for imaging with both modalities of IMIS.

BIBLIOGRAPHY

1. *Positive margins following surgical resection of breast carcinoma: Analysis of pathologic correlates.* **Miller, Alexander R.** 3, 2004, Journal of Surgical Oncology, Vol. 86, pp. 134-140.

2. *The significance of the site of recurrence to subsequent breast cancer survival.* **Imkampe, A., Bendall, S., Bates, T.** 4, 2007, European Journal of Surgical Oncology, Vol. 33, pp. 420-423.

3. *Breast Cancer subtypes and and the risk of local and regional relapse.* **Voduc, K.D., Cheang, M.C., Tyldesley, S., Gelmon, K., Nielsen, T.O., Kennecke, H.** 10, 2010, Journal of Clinical Oncology, Vol. 28, pp. 1684-1691.

4. *Time trends in treatmant and survival of recurrences from colorectal cancer.* **Guyot, F., Faivre, J., Manfredi, S., Meny, B., Bonithon-Kopp, C., Bouvier, A.M.** 5, 2005, Annals of Oncology, Vol. 16, pp. 756-761.

5. *Postoperative surveillance recommendations for early stage colon cancer based on results from clinical outcomes of surgical therapy trial.* **Tsikitis, V.L., Malireddy, K., Green, E.A., Christensen, B., Whelan, R., Hyder, J., Marcello, P., Larach, S., Lauter, D., Sargent, D.J., Nelson, H.** 22, 2009, Journal of Clinical Oncology, Vol. 27, pp. 3671-3676.

6. *The detection and significance of melanoma micrometastases in sentinel nodes.* **Scolyer, Richard A.** 3, September 2008, Surgical Oncology, Vol. 17, pp. 164-175.

7. *Patterns of recurrence following a negative sentinel lymph node biopsy in 243 patients with stage I or II melanoma.* **Gershenwald, Jeffrey E.** 6, 1998, Journal of Clinical Oncology, Vol. 16, pp. 2253-2260.

8. **National Cancer Institute.** Breast Cancer Treatment. [Online] [Cited: 09 02, 2012.] http://www.cancer.gov/cancertopics/pdq/treatment/breast/Patient/page1/AllPages#5.

9. *Sentinel node mapping for breast cancer: current situation.* **Vidal-Sicart, S., Valdés Olmos, R.** 2012, Journal of Oncology. Published online 2012 August 15. doi: 10.1155/2012/361341.

10. *Technical details of intraoperative lymphatic mapping for early stage melanoma.* **Morton DL, Wen DR, Wong JH, Economou JS, Cagle LA, Storm FK, Foshag LJ, Cochran AJ.** 4, April 1992, Archives of Surgery, Vol. 127, pp. 392-399.

11. *A trend analysis of the relative value of blue dye and isotope localization in 2,000 consecutive cases of sentinel node biopsy for breast cancer.* **Derossis, A.M., Fey, J., Yeung, H., Yeh, S.D., Heerdt, A.S., Petrek, J., VanZee, K.J., Montgomery, L.L., Borgen, P.I., Cody, H.S. 3rd.** 5, November 2001, Journal of the American College of Surgeons, Vol. 193, pp. 473-478.

12. *The use of radioisotope combined with isosulfan Blue dye is not superior to radioisotope alone for the identification of sentinel lymph nodes in patients with breast cancer.* **Bines, S., Kopkash, K., Ali, A., Fogg, L., Wool, N.** 4, October 2008, Surgery, Vol. 144, pp. 606-610.

13. *The value of sentinel node mapping for staging melanoma.* **Dijkstra, B., Hill, A., Kelly, L., Prendegast, M., McDermott, E., O'Donnell, M., Collins, C., O'Higgins, N.** 7, July-August 2001, Irish Medical Journal, Vol. 94, pp. 210-2.

14. *SPECT-CT and real-time intraoperative imaging: new tools for sentinel node localization and radio-guided surgery?* **Olmos, R. A.** 1, January 2009, European Journal of Nuclear Medicine and Molecular Imaging, Vol. 36, pp. 1-5.

15. *Single-Photon Emission Computed Tomography/Computed Tomographyfor Sentinel Node Mapping in Breast Cancer.* **Husarik, Daniela B.** 1, January 2007, Seminars in Nuclear Medicine, Vol. 37, pp. 29-33.

16. *The hidden sentinel node and SPECT/CT in breast cancer patients.* **van der Ploeg, M. C.** 1, January 2009, European Journal of Nuclear Medicine and Molecular Imaging, Vol. 36, pp. 6-11.

17. *What is a Sentinel Lymph Node? Re-evaluating the 10% Rule for Sentlinel Lymph Node Biopsy in Melanoma.* **Kroon, H.M., Lowe, L., Wong, S., Fullen, D., Su, L., Cimmino, V.,Chang, A.E., Johnson, T., Sabel, M.S.** 2007, Journal of Surgical Oncology, Vol. 95, pp. 623-628.

18. *Sentinel lymph node biopsy for melanoma: how many radioactive nodes should be removed?* **McMasters, K.M., Reintgen, D.S., Ross, M.I., Wong, S.L., Gershenwald, J.E., Krag, D.N., Noyes, R.D., Viar, V., Cerrito, P.B., Edwards, M.J.** 3, April 2001, Annals of Surgical Oncology, Vol. 8, pp. 192-197.

19. **Wengenmair, H., Kopp, J.** Gamma Probes for Sentinel Lymph Node Localization: Quality Criteria, Minimal Requirements and Quality of Commercially Available Systems. [Online] 2005. [Cited: 03 20, 2013.] http://www.klinikum-augsburg.de/index.php/fuseaction/download/lrn_file/gammaprobes.pdf.

20. *Advances in the diagnosis and excision of breast cancer.* **Klimberg, V.S.** 1, January 2003, The American Surgeon, Vol. 69, pp. 11-14.

21. *Development of a high-resolution Si-PM-based gamma camera system.* **Yamamoto, S., Watabe, H., Kanai, Y., Imaizumi, M., Watabe, T., Shimosegawa, E., Hatazawa, J.** 23, December 2011, Physics in Medicine and Biology, Vol. 56, pp. 7555-7567.

22. *Development of a Silicon Photomultiplier Based Gamma Camera.* **Tao, A.T.** 2012, Open Access Dissertations and Theses, Vol. Paper 6415. http://digitalcommons.mcmaster.ca/opendissertations/6415.

23. *Development of a mini gamma camera for prostate imaging.* **Majewski, S., Proffitt, J., Stolin, A.** Valencia : s.n., 2011. Nuclear Science Symposium and Medical Imaging Conference . pp. 4024-4029 .

24. *A self-assembled multimodal complex for combined pre- and intraoperative imaging of the sentinel lymph node.* **Buckle, T., van Leeuwen, A.C., Chin, P.T.K., Janssen, H., Muller, S.H., Jonkers, J., van Leeuwen F.W.B.** 3, September 2010, Nanotechnology, Vol. 21.

25. *Nanocolloidal albumin-IRDye 800CW: a near-infrared fluorescent tracer with optimal retention in the sentinel lymph node.* **Heuveling, D.A., Visser, G.W., de Groot, M., de Boer, J.F., Baclayon, M., Roos, W.H., Wuite, G.J., Leemans, C.R., de Bree, R., van Dongen, G.A.** 2012, European Journal of Nuclear Medicine and Molecular Imaging, Vol. 39, pp. 1161-1168.

26. *Organic Alternatives to Quantum Dots for Intraoperative Near-Infrared Fluorescent Sentinel Lymph Node Mapping.* **Ohnishi, S., Lomnes, S.J., Laurence, R.G., Gogbashian, A., Mariani, G., Frangioni, J.V.** 3, Jul-Sep 2005, Molecular Imaging, Vol. 4, pp. 172-181.

27. *Optimization of coded aperture radioscintigraphy for sentinel lymph node mapping.* **Fujii, H., Idoine, J.D., Gioux, S., Accorsi, R., Slochower, D.R., Lanza, R.C., Frangioni, J.V.** 2, 2012, Molecular Imaging and Biology, Vol. 14, pp. 173-182.

28. *Tumor localizing radionuclides in retrospect and prospect.* **Edwards, C.L.** 3, 1979, Seminars in Nuclear Medicine, Vol. 9, pp. 186-189.

29. *Ben Cassen and the development of the rectilinear scanner.* **Blahd, W.H.** 3, Jul 1996, Seminars in Nuclear Medicine, Vol. 26, pp. 165-170.

30. **Anger, H.O.** Radioisotope Cameras. [ed.] G.J. Hine. *Instrumentation in Nuclear Medicine.* New York : Academic Press, Inc., 1967, Vol. 1, 19.

31. *Use of a gamma-ray pinhole camera for in-vivo studies.* **Anger, H.O.** 1952, Nature, Vol. 170, p. 200.

32. **Anger, H.O.** *The scintillation camera: a new instrument for mapping the distribution of radioactive isotopes.* Berkeley : University of California Radiation Laboratory, 1957.

33. **Horvath, A.** File:Photomultipliertube.svg. [Online] 04 24, 2006. [Cited: 16 2013, 04.] http://en.wikipedia.org/wiki/File:Photomultipliertube.svg.

34. **Derenzo, S., Boswell, M., Weber, M., Brennan, K.** Scintillation Properties. *Scintillation Properties.* [Online] [Cited: 08 21, 2012.] Lawrence Berkeley National Laboratory. http://scintillator.lbl.gov/.

35. **Saint Gobain Crystals.** BrilLance 380 Scintillation Material. [Online] [Cited: 01 20, 2013.] http://www.detectors.saint-gobain.com/uploadedFiles/SGdetectors/Documents/Product_Data_Sheets/BrilLanCe380-data-sheet.pdf.

36. *High-energy-resolution scintillator: Ce3+ activated LaBr3.* **van Loef, E.V.D., Dorenbos, P., van Eijk, C.W.E., Krämer, K.W., Güdel, H.U.** 10, 2001, Applied Physics Letters, Vol. 79, pp. 1573-1575.

37. *Newly developed semiconductor detectors by.* **Yamamoto, K., Yamamura, K., Sato, K., Kamakura, S., Ota, T., Suzuki, H., Ohsuka, S.** Kobe, Japan : International School for Advanced Studies, Trieste, Italy, 2007. International workshop on new photon-detector.

38. *Silicon photomultiplier and its possible applications.* **Buzhan, P., Dolgoshein, B., Filatov, L., Ilyin, A., Kantzerov, V., Kaplin, V., Karakash, A., Kayumov, F., Klemin, S., Popova, E., Smirnov, S.** 2003, Nuclear Instruments and Methods in Physics Research A, Vol. 504, pp. 48-52.

39. **Majewski, S., Proffitt, J., McKisson, J., Raylman, R., Stolin, A., Weisenberger, A.G.** *Initial Tests of a Compact Imaging Photomultiplier Made From Array of 3x3 mm2 Hamamatsu MPPC-SMD Modules.* Rome, Italy : Istituto Nazionale di Fisica Nucleare, Istitotu Nazionale di Fisica Nucleare, 2010.

40. **Hamamatsu Photonics, K.K.** *Cat. No. KAPD1023E05.* Hamamatsu City : s.n., 2009.

41. **Cherry, S.R., Sorenson, J.A., Phelps, M.E.** *Physics in Nuclear Medicine.* 3. Philadelphia : Saunders, 2003.

42. *Intraoperative imaging guidance for sentinel node biopsy in melanoma using a mobile gamma camera.* **Dengel, L.T., More, M.J., Judy, P.G., Petroni, G.R., Smolkin, M.E., Rehm, P.K., Majewski, S., Williams, M.B., Slingluff, C.L.Jr.** 4, April 2011, Annals of Surgery, Vol. 253, pp. 774-778.

43. *Development of SiPM array based compact small field of view gamma and PET imagers for intraoperative uses.* **Majewski, S., Proffitt, J., Stolin, A., McKisson, J., Raylman, R., Williams, M.B., Popovic, K., Weisenberger, A.** Orsay : s.n., 2009. Oral presentation.

44. **Sze, S.M., Ng, K.K.** *Physics of semiconductor devices.* 3. s.l. : John Wiley & Sons, Inc, 2007.

45. *A temperature-dependent gain control system for improving the stability of Si-PM-based PET systems.* **Yamamoto, S., Satomi, J., Watabe, T., Watabe, H., Kanai, Y., Imaizumi, M., Shimosegawa, E., Hatazawa, J.** s.l. : IOP Publishing, 2011, Physics in Medicine and Biology, Vol. 56, pp. 2873-2882.

46. **Hamamatsu Photonics, K.K.** Power supply module for MPPC, C11204(X), Operation manual. Hamamatsu City : s.n., 2011. Doc. No. K29-B61072e.

47. *Implementation of a High-Rate USB Data Acquisition System for PET and SPECT Imaging.* **Proffitt, J., Hammond, W., Majewski, S., Popov, V., Raylman, R.R., Weisenberger, A.G.** 2006. IEEE Nuclear Science Symposium Conference Record. Vol. 5, pp. 3063-3067.

48. *A Java Distributed Acquisition System for PET and SPECT Imaging.* **McKisson, J.E,, Hammond, W., Proffitt, J., Weisenberger, A.W.** Honolulu, Hawaii : s.n., 2007. IEEE Nuclear Science Symposium Conference. Vol. 5, pp. 3591-3593. M18-342.

49. **Kross, B.J., McKisson, J., Stolin, A., Weisenberger, A.G., Zorn, C.** *Collimator with attachment mechanism and system. 8217359* USA, 07 10, 2012.

50. *Noninvasive, infrared monitoring of cerebral and myocardial oxygen sufficiency and circulatory parameters.* **Jobsis, F.F.** 4323, 1977, Science, Vol. 198, pp. 1264-1267.

51. *The Optics of Human Skin.* **Anderson, R.R., Parrish, J.A.** 1981, Journal of Investigative Dermatology, Vol. 77, pp. 13-19.

52. *In vivo near-infrared fluorescence imaging.* **Frangioni, J.V.** 2003, Current Opinion in Chemical Biology, Vol. 7, pp. 626-634.

53. *Translation of Near-Infrared Fluorescence Imaging Technologies: Emerging Clinical Applications.* **Sevick-Muraca, E.M.** 2012, Annual Review of Medicine, Vol. 63, pp. 217-231.

54. *Near-Infrared Fluorescence Imaging in Humans with Indocyanine Green: A Review and Update.* **Marshall, M.V., Rasmussen, J.C., Tan, I., Aldrich, M.B., Adams, K.E., Wang, X., Fife, C.E., Maus, E.A., Smith, L.A., Sevick-Muraca, E.M.,.** 2, August 2012, Open Surgical Oncology Journal, Vol. 2, pp. 12-25.

55. File:Jablonski Diagram of Fluorescence Only.png. [Online] [Cited: 04 08, 2013.] http://upload.wikimedia.org/wikipedia/commons/8/89/Jablonski_Diagram_of_Fluorescence_Only.png.

56. **Terpetschnig, E., Povrozin, Y., Eichorst, J., ISS Inc.** Long-Wavelength Polarization Standards. [Technical Note]. http://www.iss.com/resources/research/technical_notes/PC1_LWPolarizationStandards.html.

57. *Light-absorbing properties, stability, and spectral stabilization of indocyanine green.* **Landsman, M.L.J., Kwant, G., Mook, G.A., Zijlstra, W.G.** 1976, Journal of Applied Physiology, Vol. 40, pp. 575-583.

58. *Near-infrared optical imaging of protease activity for tumor detection.* **Mahmood, U., Tang, C.H., Bogdanov, A., Weissleder, R.** 1999, Radiology, Vol. 213, pp. 866-870.

59. *Fluorescence-enhanced, near infrared diagnostic imaging with contrast agents.* **Sevick-Muraca, E.M., Houston, J.P., Gurfinkel, M.** 5, October 2002, Current opinion in chemical biology, Vol. 6, pp. 642-650.

60. *Fluorescence imaging with near-infrared light: new technological advances that enable in vivo molecular imaging.* **Ntziachristos, V., Bremer, C., Weissleder R.** 1, January 2003, European radiology, Vol. 13, pp. 195-208.

61. *An Operational Near-Infrared Fluorescence Imaging System Prototype for Large Animal Surgery.* **De Grand, A.M., Frangioni, J.V.** 6, s.l. : Adenine Press, December 2003, Technology in Cancer Research & Treatment, Vol. 2.

62. *Image-Guided Sentinel Lymph Node Mapping and Nanotechnology-Based Nodal Treatment in Lung Cancer Using Invisible Near-Infrared Fluorescent Light.* **Khullar, O., Frangioni, J.V., Grinstaff, M., Colson, Y.L.** [ed.] M.L. Liptay. 4, 2009, Seminars in Thoracic and Cardiovascular Surgery, Vol. 21, pp. 309-315.

63. *Total attenuation coefficients and scattering phase functions of tissues and phantom materials at 633 nm.* **Flock, S.T., Wilson, B.C., Patterson, M.S.** 5, June 1987, Medical Physics, Vol. 14, pp. 835-841.

64. *Charge coupled semiconductor devices.* **Boyle, W.S., Smith, G.E.** 4, April 1970, The Bell System Technical Journal, Vol. 49, pp. 587-593.

65. *Quantitation of brown adipose tissue perfusion in transgenic mice using near-infrared fluorescence imaging.* **Nakayama, A., Bianco, A.C., Zhang, C.Y., Lowell, B.B., Frangioni, J.V.** 1, January 2003, Molecular Imaging, Vol. 2, pp. 37-49.

66. *Angiographic effects of indocyanine green photobleaching by the diode laser.* **Mattos, R.M. Jr, Nehemy, M.B., Magalhães, E.P., Pedrosa, M.** 5, Sep-Oct 2006, Ophthalmic Surgery, Lasers and Imaging, Vol. 37, pp. 415-419.

67. *Improved Excitation Light Rejection Enhances Small-Animal Fluorescent Optical Imaging.* **Hwang, K., Houston, J.P., Rasmussen, J.C., Joshi, A., Ke, S., Li, C., Sevick-Muraca, E.M.** 3, July 2005, Molecular Imaging, Vol. 4, pp. 194-204.

68. *Image-Guided Surgery using Invisible Near-Infrared Light: Fundamentals of Clinical Translation.* **Gioux, S., Choi, H.S., Frangioni, J.V.** 5, October 2010, Molecular Imaging, Vol. 9, pp. 237-255.

69. **Brian Manning, Ph.D.** Brian's Technical FAQ. *Chroma Technology.* [Online] [Cited: August 15, 2012.] http://chroma.com/resources-support/frequently-asked-questions/brians-technical-faq.

70. **Automated Imaging Association.** Specifications of the Camera Link Interface Standard for Digital Cameras and Frame Grabbers. January 2004. Vol. 1.1.

71. **Jos. Schneider Optische Werke GmbH.** Xenoplan 1.4/17. [Online] 2012. [Cited: 03 23, 2013.] http://www.schneiderkreuznach.com/fileadmin/user_upload/bu_industrial_solutions/industrieoptik/11mm_Lenses/3MP_Compact_Lenses/Xenoplan_1.4-17.pdf.

72. **Marubeni America Corporation.** [Online] [Cited: August 20, 2012.] http://www.tech-led.com/data/Illuminator_Radiation.pdf.

73. —. L760-66-60 epoxy lens type Infrared illuminator. [Online] [Cited: August 20, 2012.] http://www.tech-led.com/data/L760-66-60.pdf.

74. **Seitter, Kevin.** RGB LED dimming circuit. 2012. Circuit drawing.

75. **Owen, H.** Volume phase holographic optical elements. [book auth.] Griffiths P.R. Chalmers J.M. *Handbook of vibrational spectroscopy.* s.l. : Wiley, pp. 482-489.

76. **Jason Cross, Chroma Technology.** Primary bandpass portion of the optical filter coating OD dependance on the angle of incident light. 2011.

77. *A Computational Approach To Edge Detection.* **Canny, J.** 6, 1986, IEEE Transactions on Pattern Analysis and Machine Intelligence, Vol. 8, pp. 679–698.

78. *Active Contour External Force Using Vector Field Convolution for Image Segmentation.* **Li, B., Acton, S.T.** 2007, IEEE Transactions on Image Processing, Vol. 16, pp. 2096-2106.

79. **American Association of Physicists in Medicine.** *Computer-Aided Scintillation Camera Acceptance Testing.* New York : American Institute of Physics, Inc., 1982.

80. **Goode, A.R.** Evaluation of Dedicated Gamma-Ray Imaging Detectors for Scintimammography. [Thesis]. May 1998.

81. *Lanthanum scintillation crystals for gamma ray imaging.* **Pani, R., Bennati, P. Betti, M., Cinti, M.N., Pellegrini, R., Mattioli, M., Orsolini Cencelli, V., Navarria, F., Bollini, D., Moschini, G., Garibaldi, F., de Notaristefani, F.** 2006, Nuclear Instruments and Methods in Physics Research A, Vol. 567, pp. 294-297.

82. *Large-Area Crystalline Microcolumnar LaBr3:Ce For High-Resolution Gamma Ray Imaging.* **Bhandari, H.B., Gelfandbein, V., Miller, S.R., Agarwal, A., Miller, B., Barber, H.B., Nagarkar, V.V.** 2011. IEEE Nuclear Science Symposium Conference Record. Vols. N1-5, pp. 12-17.

83. **NEMA.** *Performance Measurements of Gamma Cameras.* Rosslyn, VA : National Electrical Manufacturers Association, 2007. NU 1-2007.

84. **Welch, Benjamin.** *Response Report for the Lanthanum Bromide scintillator.* 2013.

85. *Intraoperative radioguidance with a portable gamma camera: a novel technique for laparoscopic sentinel node localisation in urological malignancies.* **Vermeeren, L., Valdés Olmos, R.A., Meinhardt, W., Bex, A., van der Poel, H.G., Vogel, W.G., Sivro, F., Hoefnagel, C.A. Horenblas, S.** 7, 2009, European Journal of Nuclear Medicine and Molecular Imaging, Vol. 36, pp. 1029-1036.

86. *Radio-guided surgery: advantages of a new portable γ-camera (Sentinella®) for intraoperative real time imaging and detection of sentinel lymph nodes in cutaneous malignancies.* **Stoffels, I., Poeppel, T., Boy, C., Mueller, S., Wichmann, F., Dissemond, J., Schadendorf, D., Rosenbaum-Krumme, S., Klode, J.** 3, March 2012, Journal of the European Academy of Dermatology and Venereology, Vol. 26, pp. 308-313.

87. *Precise localization of sentinel lymph nodes and estimation of their depth using a prototype intraoperative mini gamma-camera in patients with breast cancer.* **Mathelin, C., Salvador, S., Huss, D., Guyonnet, J.L.** 4, April 2007, Journal of Nuclear Medicine, Vol. 48, pp. 623-629.

88. *Intraoperative gamma imaging of axillary sentinel lymph nodes in breast cancer patients.* **Aarsvold, J.N., Greene, C.M., Mintzer, R.A., Grant, S.F.** Supplement 1, 2006, European Journal of Medical Physics, Vol. 21, pp. 76-79.

89. *Novel hand-held intraoperative radionuclide imaging.* **Johnson, D.L., Olcott, P.D., Pratx, G., Levin, C.S.** Supp.1, 2010, Annals of Surgical Oncology, Vol. 12, pp. S106-S107.

90. *High-Resolution, Hand-Held Camera for Sentinel-Node Detection.* **Scopinaro, F., Tofani, A., Di Santo, G., Di Petro, B., Lombardi, A., Lo Russo, M., Soluri, A., Massari, R., Trotta, C., Amanti, C.** 1, 2008, Cancer Biotherapy and Radiopharmaceuticals, Vol. 23, pp. 43-52.

91. *Evaluation of the efficacy of a small CdTe gamma-camera for sentinel lymph node biopsy.* **Tsuchimochi, M., Hayama, K., Oda, T., Togashi, M., Sakahara, H.** 6, 2008, Journal of Nuclear Medicine, Vol. 49, pp. 956-962.

92. *A new hand-held gamma camera for sentinel node detection in breast cancer. The Minicam experience in 50 cases.* **Garbay, J., Ricard, M., Lumbroso, J., Rimareix, F., Uzan, C., Gouy, S., Leroy, P.** 2 (Supplement), 2009, Cancer Research, Vol. 69. Abstract nr 1021.

93. *The Usefulness of a Preoperative Compact Imager, a Hand-held g-Camera for Breast Cancer Sentinel Node Biopsy: Final Results of a Prospective Double-Blind, Clinical Study.* **Kerrou, K., Pitre, S., Coutant, C., Rouzier, R., Ancel, P., Lebaux, C., Huchet, V., Montravers, F., Pascal, O., Duval, M., Lefebvre, F., Menard, L., Uzan, S., Barranger, E.** 9, 2011, The Journal of Nuclear Medicine, Vol. 52, pp. 1346-1353.

94. *Performance Characterization of a Miniature, High Sensitivity Gamma Ray Camera.* **Olcott, P.D., Habte, F., Foudray, A.M., Levin, C.S.** 5, 2007, IEEE Transactions on Nuclear Science, Vol. 54, pp. 1492-1497.

95. *Radio-guided occult lesion localisation in breast cancer using an intraoperative portable gamma camera: first results.* **Paredes, P., Vidal-Sicart, S., Zanón, G., Roé, N., Rubí, S., Lafuente, S., Pavía, J., Pons, F.** 2, February 2008, European Journal of Nuclear Medicine and Molecular Imaging, Vol. 35, pp. 230-235.

96. *First experiences with navigated radio-guided surgery using freehand SPECT.* **Rieger, A., Saeckl, J., Belloni, B., Hein, R., Okur, A., Scheidhauer, K., Wendler, T., Traub, J., Friess, H., Martignoni, M.E.** 2, 2011, Case Reports Oncology, Vol. 4, pp. 420-425.

97. **Schauer, A., Becker W., Reiser M.F., Possinger K., Reiser M.F.** *The Sentinel Lymph Node Concept.* s.l. : Springer, 2004. p. 121.

98. *Real-time intraoperative fluorescence imaging system using light-absorption correction.* **Themelis, G., Yoo, J.S., Soh, K.S., Schulz, R., Ntziachristos, V.** 6, Nov-Dec 2009, Journal of Biomedical Optics, Vol. 14.

99. *Validating the sensitivity and performance of near-infrared fluorescence imaging and tomography devices using a novel solid phantom and measurement approach.* **Zhu, B., Tan, I.C., Rasmussen, J.C., Sevick-Muraca, E.M.** 1, February 2012, Technology in cancer research and treatmant, Vol. 11, pp. 95-104.

100. *Tissue-Like Phantoms for Near-Infrared Fluorescence Imaging System Assessment and the Training of Surgeons.* **De Grand, A.M., Lomnes, S.J., Lee, D.S., Pietrzykowski, M., Ohnishi, S., Morgan, T.G., Gogbashian, A., Laurence, R.G., Frangioni, J.V.** 1, 2006, Journal of Biomedical Optics, Vol. 11, p. 014007. doi: 10.1117/1.2170579.

101. *Review of tissue simulating phantoms for optical spectroscopy, imaging and dosimetry.* **Pogue, B.W., Patterson, M.S.** 4, July/August 2006, Journal of Biomedical Optics, Vol. 11, p. 041102.

102. *Near-infrared fluorescence (NIRF) imaging in breast-conserving surgery: Assesing intraoperative techniques in tissue-simulating breast phantoms.* **Pleijhuis, R.G., Langhout, G.C., Helfrich, W., Themelis, G., Sarantopoulos, A, Crane, L.M.A., Harlaar, N.J., de Jong, J.S., Ntziachristos, V., van Dam, G.M.** 2011, European Journal of Surgical Oncology, Vol. 37, pp. 32-39.

103. *Optical Properties of Intralipid: A Phantom Medium for Light Propagation Studies* . **Flock, S.T, Jacques, S.L., Wilson, B.C., Star, W.M., van Gemert, M.J.C.** s.l. : Wiley-Liss, Inc, 1992, Lasers in Surgery and Medicine, Vol. 12, pp. 510-519.

104. **Marubeni America Corporation.** Radiation Pattern. [Online] [Cited: 09 10, 2012.] http://www.tech-led.com/data/Illuminator_Radiation.pdf.

105. **Nuvo, Inc.** Surgical lighting technology. [Online] 12 12, 2002. [Cited: 09 10, 2012.] http://www.nuvosurgical.com/pdfs/Surg_Light_Tech.pdf.

106. **Photo Research, Inc.** [Online] [Cited: 04 18, 2013.] http://hyperphysics.phy-astr.gsu.edu/hbase/vision/cie1976.html.

107. **CIE, International Commission on Illumination.** *Colorimetry*. 2004. https://law.resource.org/pub/us/cfr/ibr/003/cie.15.2004.pdf. CIE 15:2004.

108. *Correlated color temperature as an explicit function of chromaticity coordinates.* **McCamy, C.S.** 2, s.l. : Wiley Periodicals, Inc., April 1992, Color Research & Application, Vol. 17, pp. 142-144. DOI: 10.1002/col.5080170211.

109. **Billmeyer, F.W., Saltzman, M.** *Principles of Color Technology.* 2. s.l. : John Wiley & Sons, 1981. p. 58.

110. **Lamina Lighting Incorporated.** Titan LED Light Engines Data Sheet. 05 21, 2008. FM-0168.

111. **Li-Cor.** IRDye® 800CW Infrared Dye. [Online] [Cited: 02 17, 2012.] http://www.licor.com/bio/products/reagents/irdye/irdye800cw.jsp.

112. *Cancer-Targeting SPECT/NIR Fluorescence Dual-imaging Agent 99mTc-PC-1007: Synthesis and In Vivo Evaluation.* **Zhang, Y., Xiao, L., Popovic, K., Xie, X., Chordia, M.D., Chung, L.W.K., Williams, M.B., Yue, W., Pan, D.** 2013, The American Journal of Nuclear Medicine and Molecular Imaging. submitted.

113. **Harlan Laboratories.** Harlan AIN Diet Formulas. *Teklad Custom Research Diet Data Sheet.* [Online] 2008. [Cited: 01 22, 2013.] http://www.harlan.com/products_and_services/research_models_and_services/laboratory_animal_diets/teklad_custom_research_diets/ain_formulas.hl.

114. *ICG fluorescence-guided sentinel node biopsy for axillary nodal staging in breast cancer*. **Hirche, C., Murawa, D., Mohr, Z., Kneif, S., Hunerbein, M.** 2010, Breast Cancer Research and Treatmant, Vol. 121, pp. 373-378.

115. *Intraoperative identification of sentinel lymph nodes by near-infrared fluorescence imaging in patients with breast cancer.* **Tagaya, N., Yamazaki, R., Nakagawa, A., Abe, A., Hamada, K., Kubota, K., Oyama, T.** 2008, The American Journal of Surgery, Vol. 195, pp. 850-853.

116. *Sentinel lymph node biopsy in breast cancer guided by indocyanine green fluorescence.* **Murawa, D., Hirche, C., Dresel, S., Hunerbein, M.** 2009, British Journal of Surgery, Vol. 96, pp. 1289-1294.

117. *Feasibility of ICG Fluorescence-Guided Sentinel Node Biopsy in animal Models using the HyperEye Medical System.* **Yamauchi, K., Nagafuji, H., Nakamura, T., Sato, T., Kohno, N.** 2011, Annals of Surgical Oncology, Vol. 18, pp. 2042-2047.

118. *Sentinel lymph node biopsy guided by indocyanine green fluorescence for cutaneous melanoma.* **Namikawa, K., Yamazaki, N.** 2, 2011, European Journal of Dermatology, Vol. 21, pp. 184-190.

119. *Evaluation of Breast Lymphatic Pathways with Indocyanine Green Fluorescence Imaging in Patients with Breast Cancer.* **Ogasawara, Y., Ikeda, H., Takahashi, M., Kawasaki, K., Doihara, H.** 2008, World Journal of Surgery, Vol. 32, pp. 1924-1929.

120. *Fluorescence Navigation with Indocyanine Green for Detecting Sentinel Lymph Nodes in Breast Cancer.* **Kitai, T., Inomoto, T., Miwa, M., Shikuyama, T.** 3, 2005, Breast Cancer, Vol. 12, pp. 211-215.

121. *Sentinel lymph node mapping by indocyanine green fluorescence imaging in oropharyngael cancer - preliminary experience.* **Bredell, M.G.** 2010, Head & Neck Oncology, Vol. 2, pp. 31-37.

122. *Near-infrared fluorescence sentinel lymph node mapping of the oral cavity in head and neck cancer patients.* **van der Vorst, J.R., Schaafsma, B.E., Verbeek, F.P., Keereweer, S., Jansen, J.C., van der Velden, L.A., Langeveld, A.P., Hutteman, M., Löwik, C.W., van de Velde, C.J., Frangioni, J.V., Vahrmeijer, A.L.** 1, January 2013, Oral Oncology, Vol. 49, pp. 15-19.

123. *Toward Optimization of Imaging System and Lymphatic Tracer for Near-Infrared Fluorescent Sentinel Lymph Node Mapping in Breast Cancer.* **Mieog, J.S.D., Troyan, S.L., Hutteman, M., Donohoe, K.J., van der Vorst, J.R., Stockdale, A., Liefers, G., Choi, H.S., Putter, H., Gioux, S., Kuppen, P.J.K., Ashitate, Y., Löwik, C.W.G.M., Oketokoun, R., Ngo, L.H., Frangioni, J.V., Vahrmeijer, A.L.** 9, 2011, Annals of Surgical Oncology, Vol. 18, pp. 2483-2491.

124. *Imaging of lymph flow in breast cancer patients after microdose administration of a near-infrared fluorophore: feasibility study.* **Sevick-Muraca, E.M., Sharma, R., Rasmussen, J.C., Marshall, M.V., Wendt, J.A., Pham, H.Q., Bonefas, E., Houston, J.P., Sampath, L., Adams, K.E., Blanchard, D.K., Fisher, R.E., Chiang, S.B., Elledge, R., Mawad, M.E.** 3, March 2008, Radiology, Vol. 246, pp. 734-741.

125. *Randomized comparison of near-infrared fluorescence lymphatic tracers for sentinel lymph node mapping of cervical cancer.* **Schaafsma, B.E., van der Vorst, J.R., Gaarenstroom, K.N.,**

Peters, A.A., Verbeek, F.P., de Kroon, C.D., Trimbos, J.B., van Poelgeest, M.I., Frangioni, J.V., van de Velde, C.J., Vahrmeijer, A.L. 1, October 2012, Gynecologic Oncology, Vol. 127, pp. 126-130.

126. *Randomized, double-blind comparison of indocyanine green with or without albumin premixing for near-infrared fluorescence imaging of sentinel lymph nodes in breast cancer patients.* **Hutteman, M., Mieog, J.S., van der Vorst, J.R., Liefers, G.J., Putter, H., Löwik, C.W., Frangioni, J.V., van de Velde, C.J., Vahrmeijer, A.L.** 2011, Breast Cancer Research and Treatmant, Vol. 127, pp. 163-170.

127. *The FLARE Intraoperative Near-Infrared Fluorescence Imaging System: A First-in-Human Clinical Trial in Breast Cancer Sentinel Lymph Node Mapping.* **Troyan, S.L., Kianzad, V.,Gibbs-Strauss, S.L., Gioux, S., Matsui, A., Oketokoun, R., Ngo, L., Khamene, A., Azar, F., Frangioni, J.V.** 2009, Annals of Surgical Oncology, Vol. 16, pp. 2943-2952.

128. *Sentinel lymph node detection in skin cancer patients using real-time fluorescence navigation with indocyanine green: preliminary experience.* **Fujiwara, M., Mizukami, T., Suzuki, A., Fukamizu, H.** 10, October 373-378, 2009, Journal of plastic, reconstructive & aesthetic surgery, Vol. 62.

129. *Sentinel Lymph Node Detection by Indocyanine Green Fluorescence Imaging in Skin Cancer Patients: Technical Refinement.* **Mizukami, T., Fujiwara, M., Suzuki, A., Nagata, T.,Fukamizu, H.** 2010, The Open Surgical Oncology Journal, Vol. 2, pp. 57-61.

130. *Intraoperative Multispectral Fluorescence Imaging for the Detection of the Sentinel Lymph Node in Cervical Cancer: A Novel Concept.* **Crane, L.M.A., Themelis, G.,Pleijhuis, R.G., Harlaar, N.J., Sarantopoulos, A., Arts, H.J.G., van der Zee, A.G.J., Ntziachristos, V., van Dam, G.M.** 2011, Molecular Imaging and Biology, Vol. 13, pp. 1043-1049.

131. *Video-assisted thoracoscopic indocyanine green fluorescence imaging system shows sentinel lymph nodes in non-small-cell lung cancer.* **Yamashita, S., Tokuishi, K., Anami, K., Miyawaki, M., Moroga, T., Kamei, M., Suehiro, S., Ono, K., Takeno, S., Chujo, M., Yamamoto, S., Kawahara, K.** 2011, The journal of thoracic and cardiovascular surgery, Vol. 141, pp. 141-144.

132. *Sentinel node mapping guided by indocyanine green fluorescence imaging in gastric cancer.* **Tajima, Y., Yamazaki, K., Masuda, Y., Kato, M., Yasuda, D., Aoki, T., Kato, T., Murakami, M., Miwa, M., Kusano, M.** 1, January 2009, Annals of Surgery, Vol. 249, pp. 58-62.

133. *Intraoperative gamma imaging of axillary sentinel lymph nodes in breast cancer patients.* **Aarsvod, J.N., Greene, C.M., Mintzer, R.A., Grant, S.F.** Supplement 1, 2006, European Journal of Medical Physics, Vol. 21, pp. 76-79.

134. *A hand-held imaging probe for radio-guided surgery: physical performance and preliminary clinical experience.* **Pitre, S., Ménard, L., Ricard, M., Solal, M., Garbay, J.R., Charon, Y.** 3, 2003, European Journal of Nuclear Medicine and Molecular Imaging, Vol. 30, pp. 339-343.

135. *A New Intraoperative Gamma Camera for the Sentinel Lymph Node Procedure in Breast Cancer.* **Mathelin, C., Salvador, S., Bekaert, V., Croce, S., Andriamisandratsoa, N., Liegeois, P., Prados, E., Guyon, J.** 2008, Anticancer Research , Vol. 28, pp. 2859-2864.

136. **Digirad Corporartion.** 2020tc imager flexible single-head gamma camera. [Online] 2007. [Cited: 03 13, 2013.] http://www.digirad.com/downloads_2007/2020tc_s.pdf.

137. *Assessment of the solid-state gamma camera to depict axillary sentinel lymph nodes in breast cancer patients.* **Goto, M., Okuyama, C., Kubota, T., Ushuima, Y., Nishimura, T.** 7, 2005, Annals of Nuclear Medicine, Vol. 19, pp. 627-631.

138. *Usefulness of a solid-state gamma camera for sentinel node identification in patients with breast cancer.* **Motomura, K., Noguchi, A., Hashizume, T., Hasegawa, Y., Komoike, Y., Inaji, H., Saida, T., Koyama, H.** 1, 2005, Journal of Surgical Oncology, Vol. 89, pp. 12-17.

139. *A prototype small CdTe gamma camera for radio-guided surgery and other imaging applications.* **Tsuchimochi, M., Sakahara, H., Hayama, K., Funaki, M., Ohno, R., Shirahata, T., Orskaug, T., Maehlum, G., Yoshioka, K., Nygard, E.** 12, 2003, European Journal of Nuclear Medicine and Molecular Imaging, Vol. 30, pp. 1605-1614.

140. *Sentinel lymph node mapping of invasive urinary bladder cancer in animal models using invisible light.* **Knapp, D.W., Adams, L.G., Degrand, A.M., Niles, J.D., Ramos-Vara, J.A., Weil, A.B., O'Donnell, M.A., Lucroy, M.D., Frangioni, J.V.** 6, December 2007, European Urology, Vol. 52, pp. 1700-1708.

141. *Near-infrared fluorescence imaging of liver metastases in rats using indocyanine green.* **van der Vorst, J.R., Hutteman, M., Mieog, J.S., de Rooij, K.E., Kaijzel, E.L., Löwik, C.W., Putter, H., Kuppen, P.J., Frangioni, J.V., van de Velde, C.J., Vahrmeijer, A.L.** 2, May 2012, The Journal of Surgical Research, Vol. 174, pp. 266-271.

142. *Image-guided sentinel lymph node mapping and nanotechnology-based nodal treatment in lung cancer using invisible near-infrared fluorescent light.* **Khullar, O., Frangioni, J.V., Grinstaff, M., Colson, Y.L.** 4, 2009, Seminars in Thoracic and Cardiovascular Surgery, Vol. 21, pp. 309-315.

143. *Clinical translation of ex vivo sentinel lymph node mapping for colorectal cancer using invisible near-infrared fluorescence light.* **Hutteman, M., Choi, H.S., Mieog, J.S., van der Vorst, J.R., Ashitate, Y., Kuppen, P.J., van Groningen, M.C., Löwik, C.W., Smit, V.T., van de Velde, C.J., Frangioni, J.V., Vahrmeijer, A.L.** 4, April 2011, Annals of Surgical Oncology, Vol. 18, pp. 1006-1014.

144. *New device for intraoperative graft assessment: HyperEye charge-coupled device camera system.* **Handa, T., Katare, R.G., Nishimori, H., Wariishi, S.,Fukutomi, T., Yamamoto, M., Sasguri, S., Sato, T.** 2010, General Thoracic and Cardiovascular Surgery, Vol. 58, pp. 68-77.

145. *Real-time intraoperative fluorescence imaging system using light-absorption correction.* **Themelis, G., Yoo, J.S., Soh, K., Schulz, R., Ntziachristos, V.** 6, November/December 2009, Journal of Biomedical Optics, Vol. 14, p. 064012.

146. *ntraoperative Multispectral Fluorescence Imaging for the Detection of the Sentinel Lymph Node in Cervical Cancer: A Novel Concept.* **Crane, L.M.A., Themelis, G.,Pleijhuis, R.G., Harlaar, N.J., Sarantopoulos, A., Arts, H.J.G., van der Zee, A.G.J., Ntziachristos, V., van Dam, G.M.** 2011, Molecular Imaging and Biology, Vol. 13, pp. 1043-1049.

147. *Near-infrared fluorescence (NIRF) imaging in breast-conserving surgery: Assessing intraoperative techniques in tissue-simulating breast phantoms.* **Pleijhuis, R.G., Langhout, G.C., Helfrich, W., Themelis, G., Sarantopoulos, A., Crane, L.M., Harlaar, N.J., de Jong, J.S., Ntziachristos, V., van Dam, G.M.** 2011, European Journal of Surgical Oncology, Vol. 37, pp. 32-39.

148. *Multiplex techniques for frequency-domain photon migration imaging.* **Reynolds, J.S., Troy, T.L., Sevick-Muraca, E.M.** 1997, Biotechnology Progress, Vol. 13, pp. 669-680.

149. *The usefulness of photodynamic eye for sentinel ymph node identification in patients with cervical cancer.* **Furukawa, M., Oi, H., Yoshida, S., Shigetomi, H., Kanayama, S., Kobayashi, H.** 96, 2010, Tumori, pp. 936-940.

150. *An Experimental Study to Evaluate the Fluobeam 800 Imaging System for Fluorescence-Guided Lymphatic Imaging and Sentinel Node Biopsy.* **Hirche, C., Engel, H., Kolios, L., Cognie, J., Hünerbein, M., Lehnhardt, M., Kremer, T.** December 2012, Surgical Innovation, pp. 1-8. doi: 10.1177/1553350612468962.

151. *Laser-induced fluorescence of indocyanine green: plastic surgical applications.* **Holm, C., Mayr, M., Tegeler, J., Becker, A., Pfeiffer, A., Muhlbauer W.** 2003, European Journal of Plastic Surgery, Vol. 26, pp. 19-25.

152. *Validation of IC-VIEW fluorescence videography in a rabbit model of mesenteric ischaemia and reperfusion.* **Toens, C., Krones, C.J., Blum, U., Fernandez, V., Grommes, J., Hoelzl, F., Stumpf, M., Klinge, U., Schumpelick, V.** 4, May 2006, International Journal of Colorectal Disease, Vol. 21, pp. 332-338.

153. *A New and Simplified Method for Coronary and Graft Imaging During CABG.* **Rubens, F.D., Ruel, M., Fremens, S.E.** 2, 2002, The Heart Surgery Forum, Vol. 5, pp. 141-144.

154. *Novadaq SPY: intraoperative Quality Assessment in Off-Pump Coronary Artery Bypass Grafting.* **Reuthebuch, O., Häussler, A., Genoni, M., Tavakoli, R., Odavic, D., Kadner, A., Turina, M.** 2, February 2004, Chest, Vol. 125, pp. 418-424.

155. *An intraoperative fluorescent imaging system in organ transplantation.* **Sekijima, M., Tojimbara, T., Sato, S., Nakamura, M., Kawase, T., Kai, K., Urashima, Y., Nakajima, I., Fuchinoue, S., Teraoka, S.** 2004, Transplantation Proceedings, Vol. 36, pp. 2188-2190.

156. *Novadaq SpyTM Intraoperative Imaging System – Current Status.* **Vogt, P.R., Bauer, E.P., Graves, K.** 2003, The Journal of Thoracic and Cardiovascular Surgery, Vol. 51, pp. 49-51.

157. *Nanocolloidal albumin-IRDye 800CW: a near-infrared fluorescent tracer with optimal retention in the sentinel lymph node.* **Heuveling, D.A., Visser, G.W., de Groot, M., de Boer, J.F., Baclayon, M., Roos, W.H., Wuite, G.J., Leemans, C.R., de Bree, R., van Dongen, G.A.** 2012, European Journal of Nuclear Medicine and Molecular Imaging, Vol. 39, pp. 1161-1168.

158. *First demonstration of 3-D lymphatic mapping in breast cancer using freehand SPECT.* **Wendler, T., Herrmann, K., Schnelzer, A., Lasser, T., Traub, J., Kutter, O., Ehlerding, A., Scheidhauer, K., Schuster, T., Kiechle, M., Schwaiger, M., Navab, N., Ziegler, S.I., Buck, A.K.** 8, August 2010, European Journal of Nuclear Medicine and Molecular Imaging, Vol. 37, pp. 1452-1461.

159. *Comparing the hybrid fluorescent-radioactive tracer indocyanine green-99mTc-nanocolloid with 99mTc-nanocolloid for sentinel node identification: a validation study using lymphoscintigraphy and SPECT/CT.* **Brouwer, O.R., Buckle, T., Vermeeren, L., Klop, W.M., Balm, A.J., van der Poel, H.G., van Rhijn, B.W., Horenblas, S., Nieweg, O.E., van Leeuwen, F.W., Valdés Olmos, R.A.** 7, July 2012, Journal of Nuclear Medicine, Vol. 53, pp. 1034-1040.